Biomechanical characterization of fibrolamellar bone using nano-scale modulus mappin

Auteur : Muraro, Pauline
Promoteur(s) : Ruffoni, Davide
Faculté : Faculté des Sciences appliquées
Diplôme : Master en ingénieur civil biomédical, à finalité spécialisée
Année académique : 2020-2021
URI/URL : http://hdl.handle.net/2268.2/11555

UNIVERSITY OF LIEGE
FACULTY OF APPLIED SCIENCES

Biomechanical characterization of fibrolamellar bone using nano-scale modulus mapping

Master thesis conducted by

PAULINE MURARO

with the aim of obtaining the degree of Master in Biomedical Engineering

Under the supervision of

DAVIDE RUFFONI

PhD Student supervisor :

ASTRID CANTAMESSA

Liège

Academic year 2020-2021

Abstract

Bone has the amazing ability to adapt its mass, structure and material properties to fulfill specific loading requirements. The bone of large and fast growing animals, such as cows and horses, has to solve two challenges: it has to grow very quickly and, at the same time, it has to provide sufficiently high stiffness and toughness. In general, the hierarchical structure of bone shows several strategies, at different length scales, to combine high stiffness with high toughness. This is particularly true for secondary lamellar bone, which is a type of bone formed rather slowly during the biological process of bone remodeling. The mechanical competence of fast growing bone is usually inferior to secondary bone, however nature has found other strategies to reinforce fast growing bone, also called fibrolamellar bone, such that it can sustain the high loads as required in large animals while allowing a rapid growth.

Fibrolamellar bone has received only limited attention, nevertheless it is a very relevant type of bone to better understand the rapid bone formation, as required, for instance during bone healing. The basic unit of fibrolamellar bone is formed between two large blood vessels. Firstly, a layer of hypercalcified disordered bone is quickly deposited. This serves, most likely, as a scaffold for the formation of parallel fibers bone, with the mineralized collagen fibers well oriented along the longitudinal direction. Around the blood vessels, parallel fiber bone is replaced by more classical lamellar bone. Although the structure of fibrolamellar bone is quite well-known, its mechanical properties are largely unexplored. Specifically, there is no information on the local mechanical behavior of the different basic blocks (i.e., hypercalcified layer, parallel fibers and lamellar region) which constitute fibrolamellar bone.

This master thesis proposes to use a complex and fairly new nanoscopic mechanical characterization method based on nanoindentation and called modulus mapping, to analyze with high spatial resolution the mechanical properties of a fibrolamellar bone unit. The modulus mapping technique was first applied to a standard fused quartz sample to tune the parameters and to establish a proper protocol to obtain reproducible data. This material has a know Young's modulus, allowing to calibrate the modulus mapping approach before going to bone.

In the second part of the thesis, fibrolamellar bone was investigated. Firstly, scanning electron microscopy was used to characterize the microstructure of fibrolamellar bone, confirming the different building units, although the mineral content of the central layer was not higher in comparison to other regions. Second, the local mechanical properties were investigated by combining traditional static indentations and modulus mapping. Interestingly, the central layer had a lower modulus then the other regions, suggesting a more disorganized arrangement of the mineralized collagen fibers. Additionally, the ratio of the elastic properties between thin and thick lamellae present in the lamellar region could be well characterized by modulus mapping and was much higher than traditionally reported in the literature. Furthermore, the parallel fiber region and the thick lamellae showed the highest elastic properties. Finally, high load indentation was used to generate local fractures and the fracture paths were characterized by electron microscopy. The results showed that fractures were deflected in the lamellar region around the large blood vessels while cracks could propagate relatively straight inside the parallel fibers region.

In conclusion, the present work reports, for the first time, local nanoscale elastic and fracture properties of fibrolamellar bone which are relevant to understand how nature combines the conflicting requirement of rapid bone growth with good mechanical properties. Future work may focus on the central layer to determine its composition using quantitative techniques such as qBEI and maybe apply this process to the unexplored cement line.

Acknowledgements

This work is my first real experience in the world of research and also in the application of what we have been taught for more than four years. It allowed me to discover a very interesting and enriching sector that is the research on biocomposite materials. People have accompanied me throughout this work and, I wish to thank them.

First I would like to sincerely thank my promoter Professor Ruffoni, for this very exciting subject, his time, his patience and his experience. Throughout the work he was available and gave me precious advice.

Then I would like to thank all the people of the MBBM lab who welcomed me, who created a good working atmosphere (in a very nice office), who reassured me and who gave me precious advice from their fresh experience. In particular I would like to thank Astrid Cantamessa, PhD student who supervised me, for many things. She was very kind, continually there to help, understood and supported me, and was always available at any time and any day. Then I would also like to thank Yann Delaunois for his help with the microscope, his availability and his patience in certain moments.

Thanks also to the members of my jury who took time to read my master's thesis and attend my oral presentation.

Moreover, I would also like to thank my boyfriend, Lucas Delvaux, who has always been there to support me, to motivate me, to believe in me and to listen to me about this work.

Finally, I am grateful to my family who allowed me to do these studies, supported me throughout this work and who encouraged and advised me. My friends too, especially Lise, Laura and Pauline, for their proofreading, encouragement, unlimited support and their joy of life.

Contents

Introduction

Nature is a source of inspiration for humans who try to reproduce what it is capable of doing. For example, the first machines built to fly were inspired by birds; water-repellent surfaces like waterproof jackets were invented by studying and reproducing the ability of the lotus to repel water; velcro was inspired by a plant that uses small hooks to attach itself to the fur of animals and then go elsewhere... [1]. This discipline, which consists of drawing inspiration from the composition, structure, form and properties of living things present in nature, is called biomimicry. It requires close collaboration between several domains such as biologists, engineers, physicists... . This branch was therefore born regarding the incredible capacity of nature to adapt to its environment and to optimize each of its elements through natural selection and evolution. The best that man can do is what nature does.
In addition nature has the ability to combine properties that are contradictory which is still a challenge for humans. In general, what is stiff and strong is brittle and what is tough is deformable and therefore has a low stiffness. However, nature is able to combine a high toughness with a high stiffness and a high strength [2].

Bone is a perfect example of the combination of these two contradictory properties, that is why it is interesting to study. The cortical bone present in humans is mainly investigated because a good understanding of its composition and structure allows, among other things, to produce implants. However, there are different bone structures that are captivating. Among them, there is the fibrolamellar bone structure. This bone present in many large mammals has been little studied while it has two very interesting features that are difficult to combine. The structure allows to have at the same time a rapid growth of the bone and strong mechanical properties needed to take up the weight of those large animals [3]. Nature has succeeded in combining a weak, randomly organized material, which guarantees rapid growth with a material with high mechanical properties that can support the weight of the animal and thus assure the strength of the skeleton [4].

The structure of the bone extends over several length scales and each level has its importance in the final properties. However, to study microscopic or even nanoscopic elements, advanced techniques must be used. With the evolution of technology, man is able to reach microscale and nanoscale resolution. Modulus mapping is one of such techniques created with the aim of studying the mechanical properties of biocomposites like bone at the nanoscale thanks to its lateral resolution of 20 nm. However, this method being highly challenging, recently developed and not widespread, its calibration is necessary to obtain consistent results.

In this master thesis, the modulus mapping technique is studied in order to implement a protocol adapted to bone. This allows to investigate the mechanical properties of the special structure of a fibrolamellar bone unit. This report is divided into 4 chapters.

The first chapter is dedicated to a theoretical explanation of the different points that are addressed in this master thesis. At the beginning, a consequent reminder on bones is made in order to understand their structure and to describe their components. It ends with a part of what is known for the structure and the mechanical properties of the fibrolamellar bone. Then the techniques of static indentations and

modulus mapping are explained in order to instill the necessary basis for understanding the tests performed with them. To close this chapter, a brief explanation of the operating principle of a scanning electron microscope is given to be able to correctly extract the information provided by these images.

The second chapter focuses on the experimental part that has been conducted throughout this master thesis. First the preparation of the samples is explained. Next comes the whole calibration of the modulus mapping with an overview of the main tests which were carried out during one month and a half on fused quartz to finally establish a protocol which allows to have reproducible measurements on bones.

The third one presents the results. The images obtained with the scanning electron microscope of the composition and structure are analyzed. Then the results of the tests carried out to study the mechanical properties are stated. This chapter ends with a brief overview of the results obtained with the high load indents that allow to watch the propagation of cracks.

The last chapter includes a discussion of the results of each test by comparing them with the previous measurements and with other studies from the literature. Then the limitations encountered during this master thesis are exposed and some future works that are interesting to investigate are proposed.

Chapter 1

Background

The purpose of this chapter is to provide a context and a background of the elements that have been studied throughout this master thesis. In the first part, generalities on bone are presented, passing through all levels of the hierarchy. Fibrolamellar bone, the structure studied in this work, is explained in more detail at the end of this section. In the second section, the technique of nanoindentation and mainly the technique of the modulus mapping are reviewed and in the third one, the scanning electron microscope is briefly described. In the last part, the main contributions of this master thesis are outlined.

1.1 Bones

1.1.1 Generalities of bones

Bones representing stiff skeletal material are present in vertebrates [5]. With tendons, ligaments, cartilage and muscles, they are the major components of the musculoskeletal system whose role is to support the weight of the body and to allow a living being to move [6]. Bones are therefore important and accomplish vital functions. They play a role in the hematopoiesis. In fact, in some parts of the bones there is some red bone marrow. This marrow is the center of production of red and white blood cells and platelets. Bones also act as a 'mineral bank' since they contain mainly calcium and phosphorous. In the body, 99% of calcium (Ca^{2+}) is stored in the skeleton and the level of calcium in the blood can be regulated thanks to the remodeling process which allows to release it or not in the body. In addition they play the role of protectors of vital organs. As examples, there are the cranial box that protects the brain, the thoracic cage that guards the heart and lungs and the vertebrae that enclose the spinal cord. They can ensure this role of protection through their ability to absorb high energy while having a low weight. [7, 8, 9]

In the body, there are different types of bones which have their own specificities and their own roles. They are characterized by their size and shape. The first type is long bone (FIGURE 1.1) like the femur. This type of bone is elongated along a major axis and most of the time has a cylindrical shape [5]. Their role is to provide stability against bending and buckling [7]. The second type is short bones (FIGURE 1.1) like vertebrae. They have approximately the same size in all directions and, they provide stability against compression. A third type is plate-like bones (FIGURE 1.1) such as the skull. For these bones, one dimension is always smaller than the other two. They are thin with a small curvature. This type of bone is well suited to resist bending moments and their roles are to protect vital organs and allow muscle attachment. [7, 8, 9]

Figure 1.1: The three types of bone. From left to right: long bone, plate-like bone and short bone (adapted from [10]).

For this master thesis, a peculiar structure present in long bones was studied. Therefore, we are focusing on this type of bone in the rest of this section.

1.1.2 Long bone

Long bone can be cut in three main regions shown in FIGURE 1.2. The first one is the central part called the diaphysis. It contains the bone marrow cavity. The second one is the epiphysis. This part is located at each end of the bone and two growth plates separate it from the rest. They are responsible for the growth of the bone along its main axis. The last region is the metaphysis. This is the transitional part between the epiphysis and the diaphysis. It has a conical shape because it connects two relatively cylindrical regions of different diameters. [7, 11]

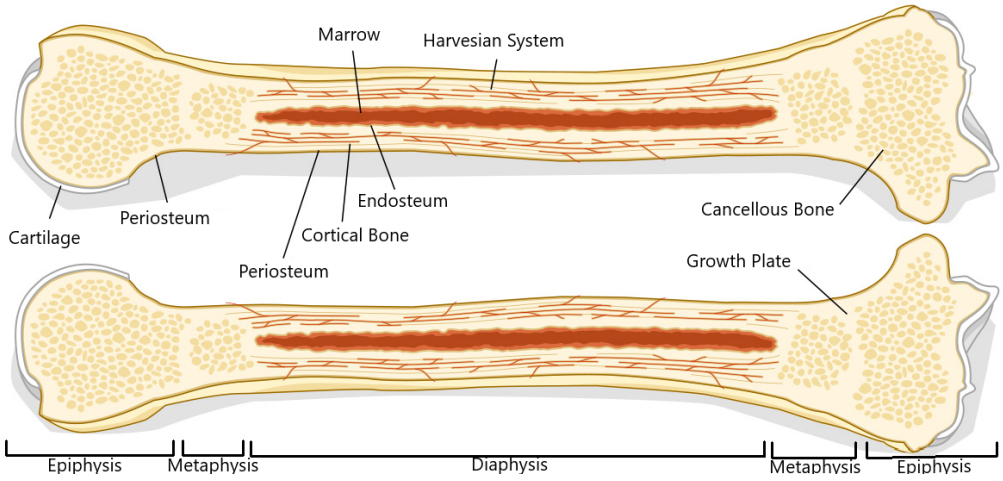

Figure 1.2: General form of long bones (adapted from [12]).

The external surface of the bone is covered with a layer of cells called the periosteum. It is made of dense connective tissue and contains a lot of blood vessels and nerves [13, 14]. It nourishes the surface of the bone and ensures thick ossification [8]. On the internal surfaces, such as the cavities, there is another kind of connective tissue layer: the endosteum. This layer contains quiescent cells that are involved in bone remodeling (process presented in SUBSECTION 1.1.3). These cells play a role in the bones' homeostasis [13]. They are shown in FIGURE 1.2. Inactive surfaces of bone are also covered by a cell layer called the bone-lining cells. These are old cells involved in the bone remodeling process that have flattened. They serve to protect the bone and to control and regulate the movement of ions such as calcium ions between the bone and the body [5, 15, 16].

In long bone, two opposite structures can be found. One is trabecular bone, also called cancellous bone. This type is located at the extremities (epiphyses) and is distinguished by a high porosity. The

second type is cortical bone forming the central part of the bone. This one is characterized by a very low porosity. Both of them are identical in terms of chemical composition [17].

1.1.2.1 Trabecular bone

► **Structure**

Trabecular bone corresponds to 20% of the skeletal mass. It is a spongy type of bone characterized by a very low weight. This feature is due to the presence of 3-dimensional (3D) interconnected pores filled up with red bone marrow. The porosity of this type of bone ranges from 75 to 95% [18]. The size of one pore is approximately equal to 10^3 µm [19]. Trabecula are arranged in a variable way which depends on the location in bone, the location in the body, the morphological characteristics of the person and its age [7]. This 3D trabecula network reflects the forces acting on the bone. Indeed, the bone is placed in such a way as to take up the forces applied to it as well as possible: some trabeculae take up the compression ones, the others support the tension forces [11]. This sort of bone can be found at the ends of long bone, within flat and irregular bones and within the vertebral body. This type of structure makes it possible to build bones that are quite large but do not weigh much. At the joints, the bones are wide, they take up a large load but the corresponding stress is lower due to the larger surface. When we move to the diaphysis part of the bone, it becomes less porous, more compact because as the section decreases, it must be able to support a higher stress [18]. They also allow to absorb choc without lost of rigidity. The thickness of a trabecula is approximately $100 - 150$ µm [18]. Pores and a trabecula network are visible in FIGURE 1.3.

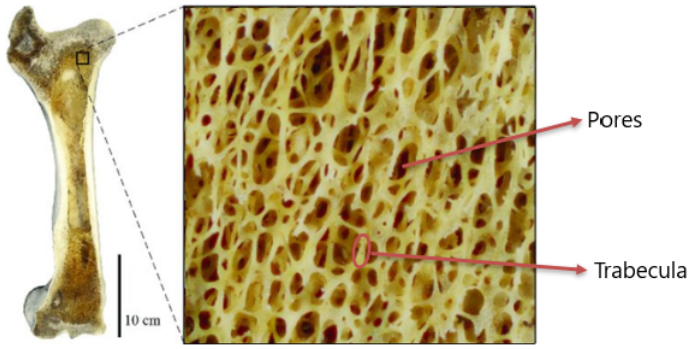

Figure 1.3: General form of trabecular bone (adapted from [20]).

Due to bone remodeling and mineralization, trabecular bone exhibits heterogeneous patchwork-like structures composed of various bone bundles that differ in mineral content, stiffness, and age (shown in FIGURE 1.4). In these bones, which are relatively thin, there are no osteons built during bone remodeling in general because nutrients can be supplied by diffusion. If the trabecula is thicker than 300 µm, blood vessels are required to furnish the bone with what it needs. Secondary osteons may then be present [5].

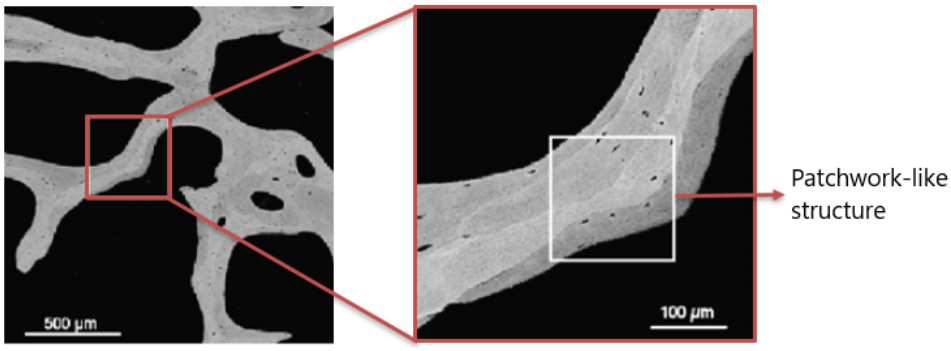

Figure 1.4: Illustration of the patchwork-like structure present in trabecular bone (adapted from [21]).

► Mechanical properties

The mechanical behavior of bone is an interaction between the structure of this one and the material which constitutes it. Trabecular bone is generally described as an orthotropic material which means that it has three planes of symmetry that are perpendicular to each other. This type of material is characterized by nine elastic constants: Young's modulus E, Poisson's ratio ν and shear modulus G in the three main axes of the planes of symmetry.
In FIGURE 1.5, typical stress/strain curves of trabecular bone for different relative density (the upper curve corresponds to a higher relative density) in compression are shown. The two curves have the same shape but the dissimilar regions are of different sizes. The first linear part represents the elastic region. This means that if we stay in this region, after release, the material recovers its initial shape and properties. After there is a peak: this is the yield point which characterizes the point from which the deformations become plastic, i.e. irreversible. This is when the failures appear. The third part is the plateau region. At this step, the system is collapsing and once the trabecula are broken, they cannot carry any load. It leads to deformations at constant load. The last part is the densification. The porosity decreases and in the end all trabeculae are broken [7].

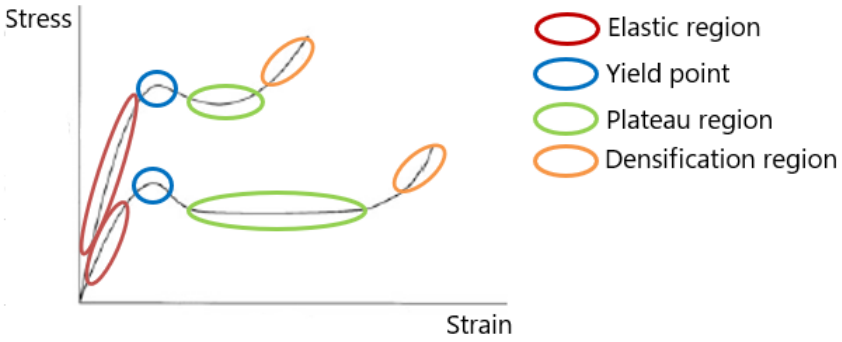

Figure 1.5: Typical stress/strain curves of the behavior of trabecular bone under compression for different relative densities (adapted from [18]).

At the apparent level, it is difficult to quantify mechanical properties of trabecular bone due to its high heterogeneity. Nevertheless, the Young's modulus (E) of trabecular bone can be linked to the apparent density (ρ_{app}) of the bone [19]. Indeed, the apparent density has a great influence on the elastic properties of the trabecular bone. It can be defined as the ratio between the mass of the bone and the bulk volume of this one (volume of bone plus volume of holes). If this apparent density increases, the Young's modulus increases. That seems logical since more material gives more stiffness. The relationship between both is an exponential one and is the following:

$$E \propto (\rho_{app})^2$$

The apparent density also has an influence on the failure properties of trabecular bone. The ultimate stress (σ_u stress at which the material breaks) can also be linked to this density. The formula is the following:

$$\sigma_u \propto (\rho_{app})^2$$

It is important to note that different architectures can correspond to the same density. This influence of the architecture must be taken into account and, a constant must be added. This one varies from one bone to another or from one region to another.

1.1.2.2 Cortical bone

► **Structure**

Cortical bone is found in different places: it forms the shafts of the long bones and also the shells that enclose the trabecular bone [18]. It represents 80% of the skeletal mass [17]. The structure of cortical bone is different in young and mature individuals. The structure of the latter is more ordered, uniform and developed than the one of the young due to the remodeling process. In young individuals, primary osteons are present. In all bovine adults, cortical bones are mostly composed of osteonal bone (secondary osteons), interstitial bone and the whole is surrounded on the endosteal and periosteal surface by lamellar bone. This last one consists of large concentric lamellae of fibrolamellar bone in large animals (explained in SECTION 1.1.5)[22]. Osteonal bone is made of 10-15 lamellae organized in concentric cylinders around a central Haversian canal (where blood vessels pass) which has a diameter of ∼50 µm oriented in the direction of the main axis of the bone. Osteons have a diameter of ∼100-200 µm with a length of 1-3 mm. Between the osteons, there is bone called interstitial bone which consists of bone remaining after the remodeling process [23]. Secondary osteons and interstitial bone can be seen in FIGURE 1.6.

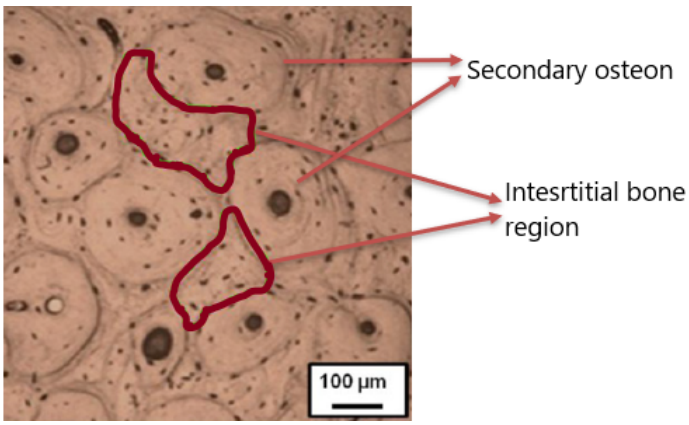

Figure 1.6: Cross-section image of cortical bovine bone of a mature individual (adapted from [23]).

Cortical bone is a dense solid but the porosity changes with age. It goes from 8 to 5 %. This can be explained by the fact that young bones need more nutrients to grow [23]. The pores present in this structure are osteocytes, canaliculi, blood vessels or Haversian canal and erosion zones [5]. Haversian channel represents the main channel of the osteons, where the blood vessels pass. After there is the lacuno-canalicular porosity which is due to the canaliculi and the osteocyte lacunae. These last ones are ellipsoidal in shape with measurements of about 5 × 10 µm. These regions are not mineralized and contain the osteocytes, hence their name. The canaliculi are canals that interconnect the Haversian canals together and with osteocytes and also with the periost which represents the external layer of long bones.

► **Mechanical properties**

Cortical bone behaves like a ductile material which means that its mechanical behavior in compression can be represented by the FIGURE 1.7. At the beginning of the curve there is an elastic zone. The slope of the straight line in this region is used to determine the Young's modulus. It corresponds to the stiffness of a material, i.e. the resistance that a material opposes its deformation. This stops at the yield point which is the elastic limit. From this point on, irreversible deformations occur in the material. This is called the plastic zone. The curve finally stops when the material breaks. This is the point of failure [24].

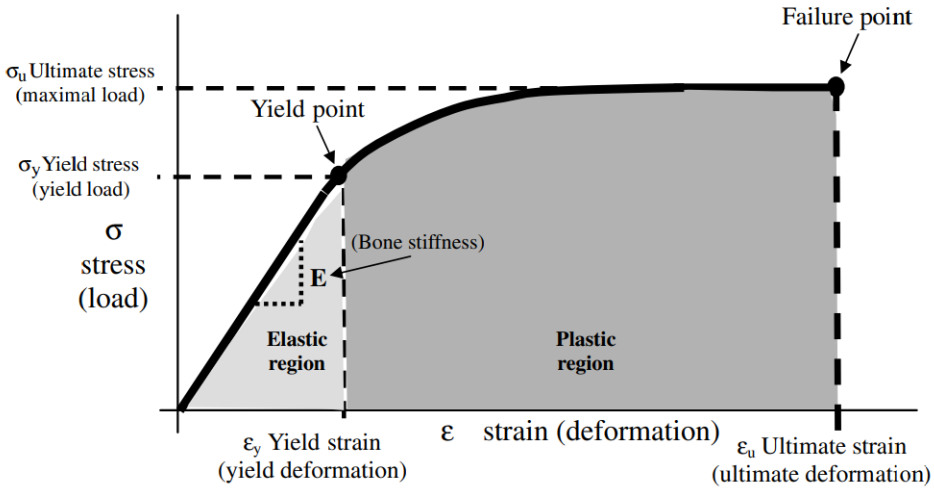

Figure 1.7: Stress/strain curve of a ductile material [25].

Due to the presence of osteons, orientation of collagen fibers and mineral crystals, cortical bone is anisotropic which means that its mechanical properties change depending on the direction [24]. Indeed, depending on this factor (longitudinal and transverse), the Young's modulus, the compressive strength and the ultimate stress/strain are different. However, this anisotropy does not affect the yield strain. Bones are stronger longitudinally than transversely (see FIGURE 1.8 and TABLE 1.1) because it is in this direction that the majority of forces are applied and bone has therefore adapted its internal architecture to its external loads. In addition, bones are stronger in compression than in tension because they are subjected to compression most of the time. This can be seen in FIGURE 1.8. Given its structure, cortical bone is stronger than the trabecular bone [18]. It provides mechanical strength due to its high resistance to bending and torsion [17].

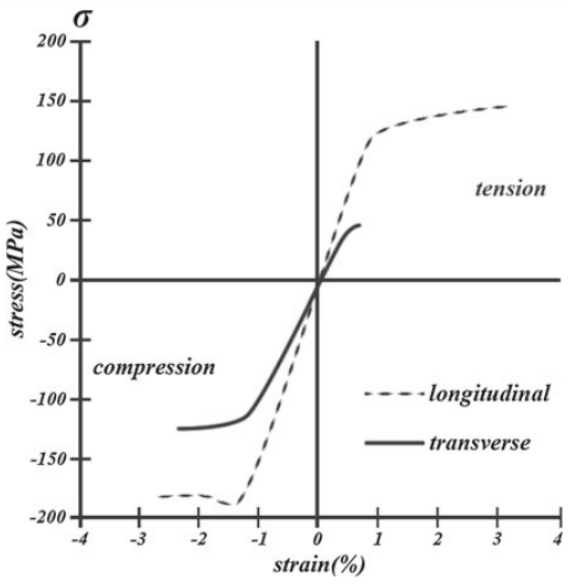

Figure 1.8: Stress/strain behavior of cortical bone in tension and compression for longitudinal and transverse directions [26].

Mechanical properties can be influenced by two factors: the porosity and the mineral content. The variations in cortical porosity can be due to changes in number, length and diameter of Haversian canals [7]. This is often correlated with age. Porosity effects mechanical properties because the more the volume fraction increases, the more the bone is able to support large loads and the ultimate stress increases. Moreover, mechanical properties are highly influenced by the mineral content as it is also shown in

TABLE 1.1. The compressive strength and the Young's modulus are higher for mature individuals which have a bigger volume percentage of minerals than young one [23]. Indeed, these features are stiffer.

Sample	Orientation	Vol. % minerals	Compressive strength [MPa]	Young's modulus [GPa]
Untreated mature	Longitudinal	43 ± 1	184.1 ± 14.7	20.5 ± 2.3
	Transverse		156.5 ± 5.3	13.0 ± 2.3
Untreated young	Longitudinal	39 ± 1	131.3 ± 39.4	6.6 ± 1.9
	Transverse		121.0 ± 3.2	5.3 ± 0.1

Table 1.1: Volume percent of minerals, compressive strength and Young's modulus for untreated mature and young individual in longitudinal and transverse section (adapted from [23]).

For the viscoelasticity, the effect can be neglected if a physiological strain rate is applied i.e. 0.01-1 [%/second]. That means that elastic properties and strength are poorly dependent on the rate and the duration of the load. For higher strain rate, this is not the case. Bone has increased stiffness, increased strength and decreased ultimate strain which makes it more brittle.

1.1.3 Biological process of bone remodeling

Bone remodeling is an important and complex process that occurs throughout life. This continuous process consists of the replacement of old bones with new ones. It allows to repair microcracks by replacing damaged bone with new bone, to adapt bone architecture in response to biomechanical forces to meet environmental loads (if the load increases, the bone mass also increases, which strengthens the bone architecture) and to regulate calcium homeostasis.

In this process, three different cells are involved in a coordinate way: osteoclasts, osteoblasts and octeocytes. Firstly, osteocytes derive from osteoblasts that have been wrapped in the mineralized bone matrix[11, 17]. These cells are then a little less active but, they still produce matrix proteins. Their shape, size and activity vary according to the age of the cell. They are connected together by canaliculi which form a dense network inside the bone. This network serves as a strain and a microdamage sensor [27]. In trabecular bone of cows (animal studied in this master thesis), the density (number of cells per bone volume) of this type of cell is approximately equal to 30 000 mm^{-3} [28]. Secondly, there is osteoblasts. They are responsible for the bone formation [11]. They are derived from multipotent mesenchymal stem cells and they never function alone, always in clusters. At the end of the deposition process of the bone matrix constituents, about 15% remain enclosed in the matrix and become osteocytes as explained before and another part remains on the surface and becomes flat lining cells. They first deposit a collagen matrix and then this matrix must be mineralized [5]. Thirdly, the last type is osteoclasts. They derive from precursor cells circulating in blood and allow the mineralized tissue resorption. They are present on the surface of calcified bone and in areas eroded by their activity [17]. They are multinucleus cells and are generally larger than other bone cells with a diameter ranging from 20 to 100 µm [11]. During the resorption, first, the osteoclasts digest the links between the crystals and the collagen, which allows the mineral to be mobilized. The collagen fibers are then digested mainly by activated collagenases [17].

Bone remodeling can occur both at the periphery and inside the bone. At the periphery the process of erosion starts at the surface and is conducted by osteoclasts. Inside the bone, it is the osteocytes that initiate bone remodeling [11]. The process (shown in FIGURE 1.9) begins with the migration of mononuclear preosteoclasts in the region of interest where they constitute multinucleated osteoclasts. They remove bone that is getting old or damaged. After this resorption, mononuclear cells prepare the surface and produce a signal to attract osteoblasts. The latter then move on to replace the old bone. To do that they put some collagen where bone is needed. The Ca^{2+} recognizes the collagen and binds to

it [7]. Then mineralization starts i.e. the mineral content and the stiffness increase over time. All this process is schematized in FIGURE 1.9. Most of the bone remodeling takes place in trabecular bone since the latter has a larger surface area than the cortical bone. The resorption stage lasts about two weeks while the formation stage remains about four months [17]. When this process is not effective, it leads to diseases such as osteoporosis.

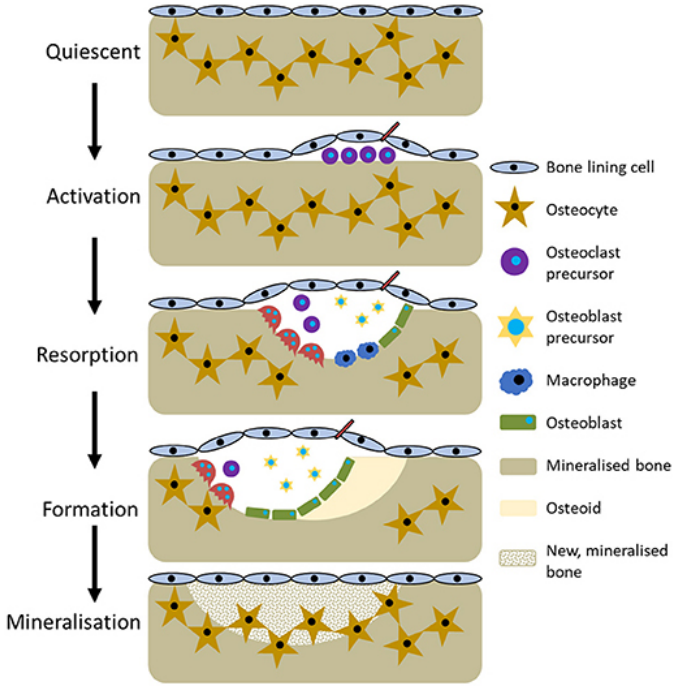

Figure 1.9: Scheme of biological process of bone remodeling [29].

The process differs slightly in trabecular and cortical bone but these differences are morphological and not biological. Bone remodeling allows the construction of basic units that constitute the bones. It is these units that are dissimilar between the different types of bones. In trabecular bone, the process is done by bone packets and in cortical bone, it is done by secondary osteons [30]. These two structures are in the order of 100 µm. Secondary osteons or Haversian systems consist of cylindrical concentric layers of mineral collagen. They are formed in this way [5] (shown in figure 1.10): the osteoclasts gather to come and remove bone. They are removing the bone by forming what is called a cutting cone and thus form a hole in the shape of a cylinder with a base that has a diameter of 200 µm and is 2000 µm long [17]. As soon as the cavity is formed, it is filled with cylindrical layers of bone that are deposited by osteoblasts. Ten osteoclasts are needed for the removal part of the process and thousands osteoblasts reform the bone [17]. The whole gives a cylinder composed of different layers with a central cavity where one or two blood vessels pass. Around these secondary osteons there is a special sheath: the cement line. It is formed at the point where the osteoclasts stop removing bone and just before the osteoclasts come to add bone to form lamellar bone. This is the boundary between old (bone matrix) and new bone (secondary osteon) [7].

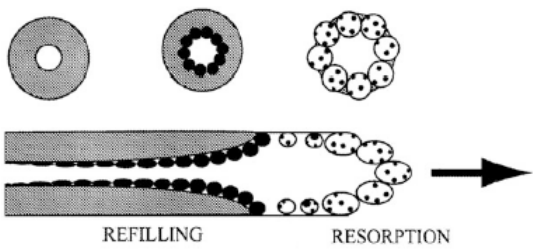

Figure 1.10: Scheme of biological process of bone remodeling in cortical bone (adapted from [18]).

1.1.4 Composition and structure of bone at different levels

Bone is made of a very complex hierarchical structure that extends to different length scales. To understand how they function and their mechanical properties, it is important to know their structure at different levels from the molecular scale to the millimeter scale.

▶ Molecular level

At the molecular level, three main components are present: proteins which constitute the organic phase, mineral crystals which represent the inorganic phase and water [5, 7].

In the organic phase, the main protein is the collagen. This is a structural protein which is the strongest and the most abundant found in the body. It has a well-defined structure shown in FIGURE 1.11. It consists of a repetitive amino acid sequence which is glycine-X-Y where X often represents the proline and Y sometimes the hydroxyproline. By repeating itself, this sequence allows to form polypeptides. Three polypeptides of the same length then associate together to form the protein molecule called tropocollagen. They are folded into a left-handed triple helical structure thanks to hydrogen bonds between the three chains. These basic building blocks have a length of about 300 nm and a diameter of 1.5 nm [30]. The tropocollagen then aggregates to form fibrils of collagen [5] with a diameter of 80–120 nm [31]. The fibrils become stable due to intermolecular cross-links. This allows the collagen molecules to be formed [5]. Collagen is present in three forms: collagen type I, type III and type IV. The difference between the three is the type of chains that are distinguished by different secondary structures [32]. This type I is composed of two $\alpha 1$ chains and one $\alpha 2$ chain while the type III is composed of three $\alpha 1$ chains [17, 32]. The main one is the type I. It represents about 90–95% of the organic matrix [11]. In addition to collagen, there are also non-collagenous proteins (osteocalcin, osteonectin and osteopontin for example). They act as a glue between mineral parts and collagen fibrils and also play a role in bone formation [22, 31]. The organic phase has the role to provide elasticity and toughness to the bone [33]. The rest of the organic components are proteoglycans, glycoproteins, sialoproteins, serum proteins and lipids [11].

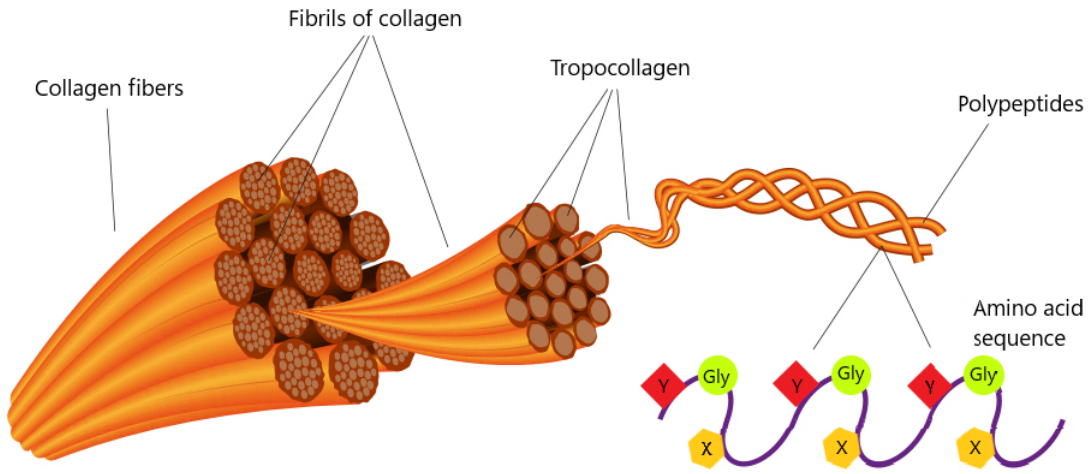

Figure 1.11: Structure of a collagen fibers (adapted from [34]).

The inorganic phase is made of mineral crystals as said before. This phase is a form of naturally occurring calcium phosphate called hydroxyapatite whose smallest unit that repeats uniformly to form the crystals is $Ca_{10}(PO_4)_6(OH)_2$. The crystals are present in version of tiny platelets with a thickness of 1.5-4 nm which form within the collagen molecules [31, 35]. The role of this phase is to provide stiffness to bones [36]. Sodium and magnesium ions associated with the mineral phase can also be found.

Their percentage in this phase is small, but of the total amount present in the body it is large, representing about 60% [11].

The last phase is water. This part is important for the mechanical behavior of the bone. Water is present at different places. There are some on the surface of the crystals, between the tropocolagens molecules, in the blood vessels, in the canaliculi and in the lacunae [31].

The proportion of these three mains components is given in the TABLE 1.2.

Weight [wet]	Volume
Inorganic : 60%	Inorganic : 40%
Organic : 30%	Organic : 35%
Water : 10%	Water : 25%

Table 1.2: Relative amounts of the three mains constituents in human bone in % of the wet weight and in % of the volume [7].

Collagen and minerals have opposite mechanical properties. Indeed, collagen has a good toughness but is soft, whereas minerals are stiff but brittle. The structure of the bones at several length scales has made it possible to combine the advantage of each component: the material is tough thanks to the proteins and rigid due to the minerals [37].

- **Basic building block level: mineralized collagen fibers**

These different constituents are arranged in a particular way as shown in FIGURE 1.12. To form the basic building block, the tropocollagen molecules line up in a row but they do not bind with the other molecules that precede or follow them. They bind with their neighbors which are next to each other. The packets of collagen molecules formed in this way are one on top of the other with a constant offset each time. This creates a gap between the head and the end of two molecules that are in the same file. As they are all stacked on top of each other and they all follow each other, this creates repeating features like this 67 nm hole that is visible in FIGURE 1.12. Mineral crystals nucleate in these holes and start to grow at the end form platelets parallel to collagen fibers [31]. The crystals are about 3 nm thick, 15 nm wide and 50 nm long while the tropocollagen molecules are 1.5 nm in diameter and 300 nm in length. These values are true for humans, they may differ slightly from other species such as bovine (the width and thickness are the same, only the length changes and is about 27.3 nm).

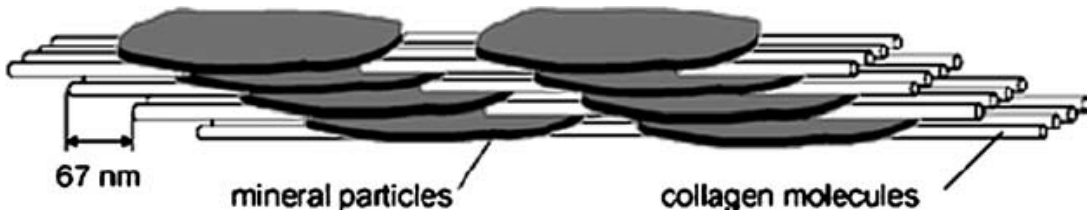

Figure 1.12: Arrangement of collagen fibrils and mineral crystals in bone [38].

- **Micrometers level**

At the micrometer level, molecules of collagen can be arranged in two different structures: woven bone which is immature bone and lamellar bone which is mature bone.

The woven bone (visible in the left part of FIGURE 1.13) is created very quickly and can grow about 4

µm and more per day. This type of bone is found especially in fast-growing fetuses and in areas that have been broken and need to be rebuilt [39]. The collagen fibers that make up this structure vary in diameter from 0.1 to 3 µm and are randomly organized. The arbitrary organization is due to the fact that bone grows quickly [11]. Given that the minerals are randomly arranged and leave space between them, the woven bone is relatively porous at the micron level. It contains a large number of cells called osteocytes which are included in extended and rather round spaces. Osteocytes are also arbitrary distributed and are connected to each other by canaliculi. Woven bone can reach a high degree of mineralization [11]. This structure is mechanically weaker than lamellar bone, which takes a longer time to build (see next paragraph) [4]. The bone is weaker due to the fact that the mineral crystals that give the bone its stiffness are oriented in the direction of the collagen fibers. Since these fibers are arranged in a random way, the crystals are also organized in a non-regular fashion so that the bone is not stiff in any direction [40].

The lamellar bone (visible in the middle part of FIGURE 1.13) is created slower than the woven bone at approximately 1 µm per day. In this type of bone, collagen fibrils and minerals are arranged in a precise way: lamellar bone corresponds to a high level of organization [11, 39]. They are organized in sheets that are called lamellae and the thickness of these lamellae alternates. There is a repeated variation between a thick lamella of about 5 µm and a thin lamella of about 1 µm. Collagen fibers and minerals are organized in a twisted plywood structure (visible on the right in FIGURE 1.13). In this arrangement, there are many layers and the collagen fibers are parallel in the same layer. Between the layers, the direction of the collagen fibers changes by a certain angle constant in size and direction. Due to this architecture, there is no preferential direction in these bones. The lamellar bones also contain osteocyte cells that are in flattened spheroid spaces and are connected with few canaliculi [11]. The smallest direction of the spheroid is parallel to the orientation of the lamella thickness. The lamellar bone is less mineralized than woven bone [5].

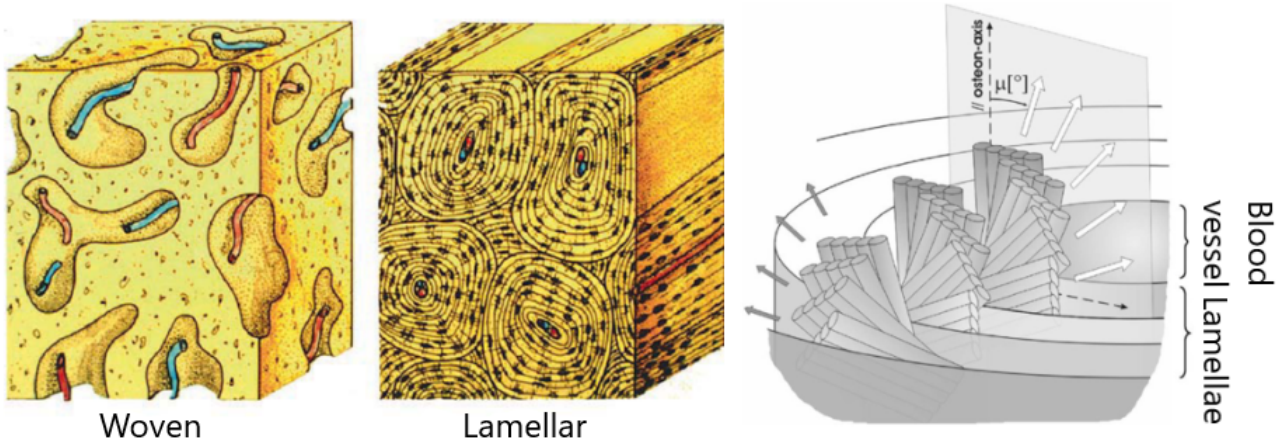

Figure 1.13: From left to right: diagram of woven and lamellar bone [39] and scheme of the twisted plywood structure (adapted from [41]).

- **Millimeters level**

At this level four different types of bone are present: woven bone, lamellar bone, Haversian system and fibrolamellar bone. The first three are explained briefly in this section. The fourth one, being the subject of this thesis, is investigated in more detail in the following section.

The first one is the woven bone that is described in the previous section. This type of bone is present at this level because it can extend uniformly over millimeters in all directions.

Secondly, there is lamellar bone also present in the previous section. They can occupy large spaces and are generally organized in a cylinder with a bony cavity in the center.

In third place, there is Haversian system or secondary osteon. It is a structure made of cylindrical and concentric layers around a cavity in which one or two blood vessels and nerves are found. The way this structure is built is explained in the previous SECTION 1.1.3. The secondary osteons are delimited by a special layer called the cement line which has a thickness of 1 or 2 µm.

1.1.5 Fibrolamellar bone

Fibrolamellar bone is a structure that is often found in rather large animals that need to grow rapidly in diameter. In addition to fast development, this transient primary organization must be strong enough to support the weight of the animal which creates compression and bending. The structure of the fibrolamellar bone is not a consensus. Two structures are highlighted. Old studies have put forward a certain structure but, new technologies have allowed to discover a new architecture different in some points.

► Structure

In fairly old studies (Martin et al. (1998), J.D. Currey et al. (2003), Mori et al. (2007)), researchers found that the fibrolamellar bone is composed of a scaffold made of woven bone and that the holes are filled with lamellar bone which consolidates them. As said in SECTION "Micrometers levels", the woven bone has the advantage of animals that need to grow rapidly to have a high rate of construction. This is due to the fact that the collagen fibers constituting it are deposited in a random manner which takes less time to build than well-ordered fibers [40]. The lamellar bone is there to reinforce the structure of woven bone because this one, as explained previously, due to its random organization, has poor mechanical properties [4]. In some studies, they found a hypercalcified line on which the woven bone was deposited [18, 42].

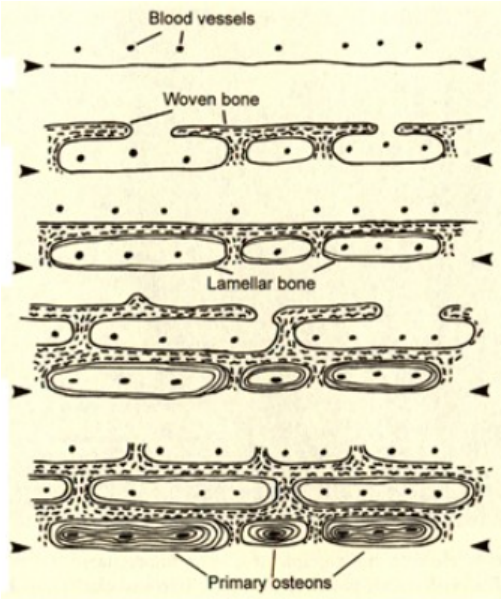

Figure 1.14: Scheme of the formation of fibrolamellar bone [5].

In FIGURE 1.14, the formation of the fibrolamellar bone is schematized. Blacks arrows show the position of the original surface. It is possible to see in this illustration that the blood vessels are the first to be put in place. Then, the woven bone comes to surround these vessels from quite far and grows leaving

large holes. These holes are used for the lamellar bone to attach to and surround the blood vessels more closely. These structures around the blood vessels are called primary osteons. They are different from the secondary osteons mentioned before and can be distinguished by the fact that they do not have a cement line.

In more recent studies (Kerschnitzki et al. (2011), Stein and Prondvai (2014), Rotem Almany Magal (2014), Barrera et al. (2016)), researchers highlight another structure. This one is arranged around a network of blood vessels and, the construction is done in several steps like the previous one. The first step is the creation of a thin, porous and hypercalcified layer (PHL). This layer will serve as a scaffold on which the various components of the fibrolamellar bone will be deposited. This first step is the fastest. The second one is the deposition of bone on this scaffold. This part of the bone is composed of parallel-fibered bone (PFL) which is composed of collagen parallel fibers. Once this bone is deposited on the hypercalcified layer, large holes remain around the blood vessels. The third step is to fill these holes with lamellar bone (LB). By folding around the blood vessels, they form primary osteons. Their role is to consolidate the structure [5, 43]. Due to the remodeling process they are replaced when the animal has matured by Haversian bone tissue also called secondary osteons which are embedded in the matrix [3, 44].

In summary, the structure of fibrolamellar bone is as follows: a hypercalcified central layer on which parallel fibers are deposited, followed by lamellar bone that surrounds a blood vessel. This structure is orthotropic [3]. A unit of fibrolamellar bone is shown in FIGURE 1.15.

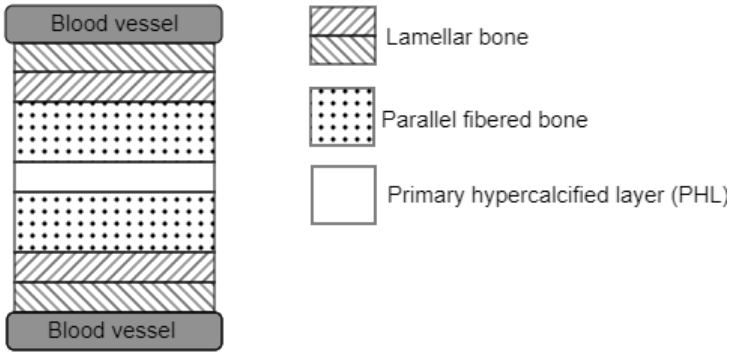

Figure 1.15: Schematic unit of fibrolamellar bone.

The different parts of this bone have been studied in more depth and are shown in FIGURES 1.15 and 1.16.

In the primary hypercalcified layer (appearing brighter in FIGURE 1.16), two different features are present. The first one is fibril arrays. Their size is approximately equal to 1-1.5 µm in minipig [43]. The fibers present in one array are parallel. The orientation of these arrays is random, there does not seem to be a trend. Also, there does not appear to have a 67 nm gap between two fibers that follow each other on the same line. Since this characteristic is not present, Rotem Almany Magal et al. think that it is type II collagen. The second distinct feature is pores. They have diameters of several tens of nanometers and, they are free of organic matter. They do not have a regular shape or specific orientation. Canaliculi are also present but in small numbers [44, 45]. The osteocytes in this layer are not well organized but they are aligned with respect to this layer which means that their main axis is parallel to the layer [45]. Since PHL does not show any preferential orientation, it can be considered as an isotropic material [43].

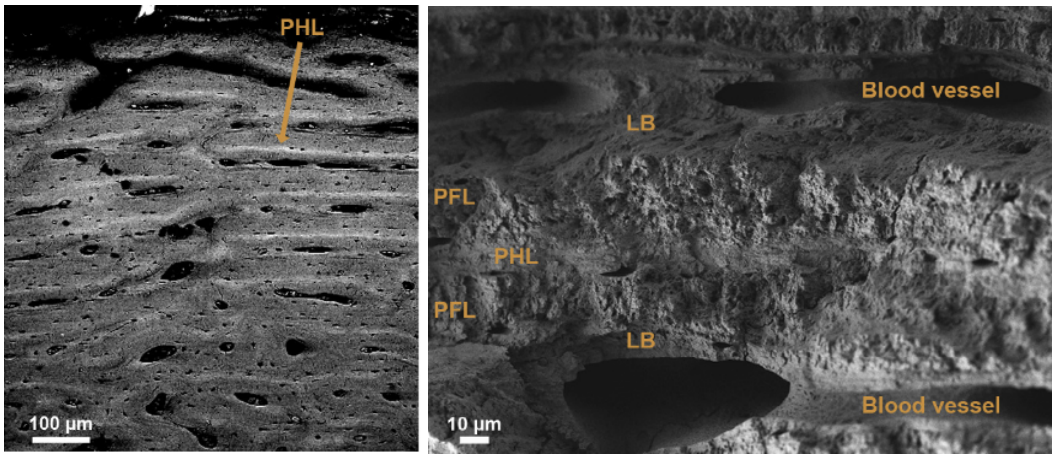

Figure 1.16: From left to right: backscattered electrons image of a periosteal region of fibrolamellar bone with bright lines which represent the PHL and a Scanning Electron Microscope (SEM) image of a fracture of a fibrolamellar unit where each structure is presented (adapted from [43]).

The parallel-fibered bone is the major component of the fibrolamellar unit. As the name suggests, these fibers are parallel to each other and their orientation is along the main axis of the long bone (in relation to a transverse section, they form an angle ranging from 85 to 120°). They also have the characteristic distance of 67 nm between two consecutive fibers. They are arranged into bundles whose diameter is in the range 1.5-3 µm and close to the PHL, a kind of sheath surrounds them. The composition and organization of this sheath are not known. The arrays in the outer part of this layer are surrounded by a thin disordered material [31]. The transitions between the different structures are not sudden, they are done gradually. Canaliculi are also present in this layer of parallel fibers bone. They are organized differently depending on whether they are in the inner or outer part. In the inner one they are relatively large in diameter (200 nm) and the collagen fibers surrounding them flatten them a little. Their orientation is not well defined because they follow tortuous paths. In the outer part, their orientation is better defined: they go in a straight line and are parallel to each other in the direction perpendicular to collagen fibrils. Their cross-sections are ellipsoidal in shape [43, 45]. The change in orientation of the canaliculi and the organization of osteocytes are a precise indicator to show the change in structure of the bone [40, 44].

Lamellar bone is found all around the blood vessels. As seen before, thin and thick lamellae are present. They are characterized by collagen fibers oriented in different directions. Two different patterns of change are observed inside a lamella: the first is a gradual change in fiber orientation and the second is a plateau where the fibers appear aligned in the same direction. Two plateaus are observable at 10 and 90°and between the two the changes seem to be gradual. The main motif is the gradual change. Canaliculi are also present in this layer. They are mainly oriented in the direction perpendicular to the lamellar boundaries and are elongated [43, 44]. The osteocytes are well organized and their main axis is parallel to the lamellae [45].

The canaliculi network explained for the three kinds of structures present in a fibrolamellar bone unit is shown in FIGURE 1.17.

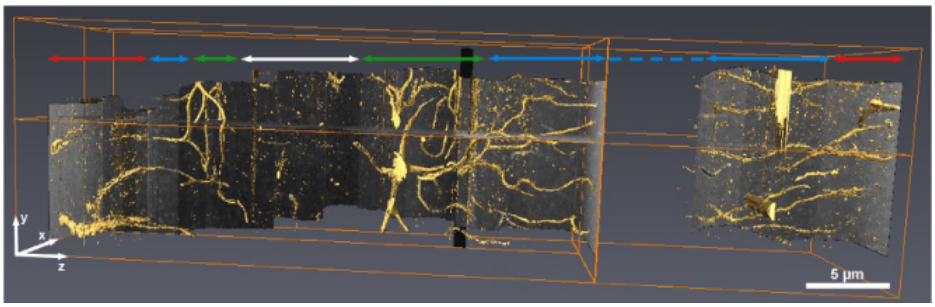

Figure 1.17: Network of canaliculi present in a fibrolamellar bone unit. The red arrows indicate the area of lamellar bone, the blue arrows indicate the area in the parallel fibers bone where they are in a straight line, the green arrows also represent the parallel fiber bone but this time when the canaliculi are parallel to the collagen fibers and finally the white arrow represents the hypercalcified layer where almost no canaliculi are present. The missing part is due to a technical problem (adapted from [43]).

► Mechanical properties

In a study conducted by Barrera et al. (2016), they tested some deer samples under compression in three directions: axial, transverse and radial. These samples were harvested from the proximal diaphysis. They found that fibrolamellar bones present the greatest Young's modulus in the axial direction. This is logical since this is the direction which has to support the highest loads. This direction is followed by the transverse orientation and after by the radial one. The material shows an orthotropic behavior. The values of Young's modulus in these different orientation are given in the TABLE 1.3.

Orientation	Young's modulus [GPa]
Axial	21.6 ± 3.3
Transverse	17.6 ± 3.0
Radial	14.9 ± 1.9

Table 1.3: Means values and standard deviation of the Young's modulus of different deer samples tested in different orientations (adapted from [3]).

They also tested a sample from the mid-diaphysis to be able to compare their results with the study of Reilly et al. (1974) [46]. The latter measured the Young's modulus of a cow femur by subjecting a cube taken from the mid-diaphysis to compression. Reilly et al. found a Young's modulus equals to 30.3 GPa and Barrera et al. found an average value for the Young's modulus equals 30.87 ±5.0 GPa. These results are almost identical. They notice that they are 30% higher than what they had found before for axial compression. This is due to the fact that the mid-diaphysis is a thinner diameter region than the proximal diaphysis, which means that a cross section in this area is smaller on the surface. Therefore, stresses are greater in this region and that the bone has had to increase its stiffness by raising mineralization in order to be able to withstand these stresses.

Benecke et al. studied the correlation between tensile stress and strain in the range of 10 µm to 1 mm in a fibrolamellar unit harvested from a bovine femur [47]. They found that up to the yield point, the strain rate is the same throughout the bone and beyond this limit, this rate varies strongly depending on the position in the sample. The strain rate increases sharply in the damaged regions and in the others it remains more or less constant. Bands of high strains are of the order of 10 mm.

Seto et al. performed micromechanical tensile loading and nanoindentation tests on fibrolamellar bone harvested from the periosteal region of the femur of a calf [48]. They tested different directions, ranging from 0° to the orientation of the collagen fibers to 90°. They found that there is a very large anisotropy

in this structure. Indeed, for tensile tests, they found a ratio of 1:20 for the Young's modulus and 1:15 for the ultimate tensile strength between 0°and 90°. As the angle to the collagen fibers increases, the Young's modulus decreases [22]. This is true for wet and dry samples as shown in FIGURE 1.18.

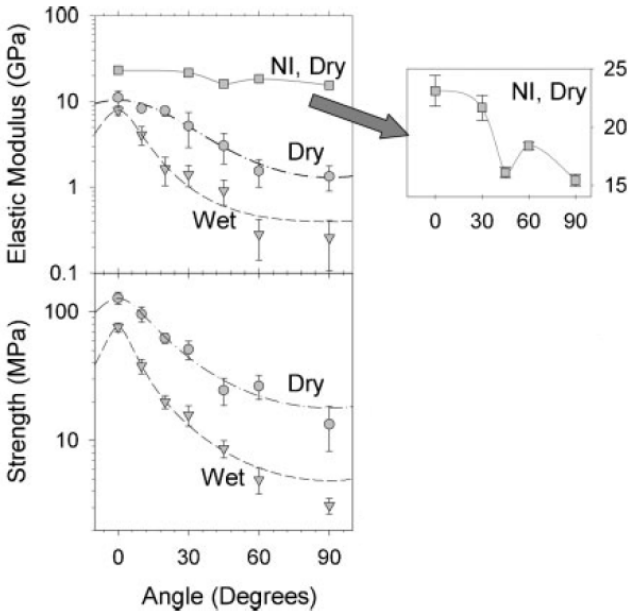

Figure 1.18: Young's modulus and tensile strength from microtensile measurements as a function of collagen fibers orientation (adapted from [48]).

They found the same trend for nanoindentation tests when the indentation surface is oriented at a certain angle of the direction of collagen fibers. They obtained 23.1±0.7 GPa for the Young's modulus along the collagen fibers axis and 15.4±0.5 GPa for the surface at 90°. This also proves the anisotropy of the fibrolamellar bone [48].

1.2 Nanoindentation and modulus mapping

1.2.1 Static indents

Nanoindentation is a technique used to locally characterize mechanical properties -Young's modulus and hardness- at the nanoscale of material. The basic operation of this method is to apply a certain load on a sample with a diamond tip and to register the corresponding displacement. A load-depth curve can be generated with this data (FIGURE 1.19) [49].

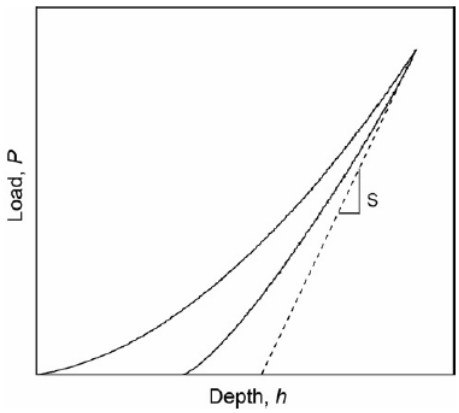

Figure 1.19: Load-depth curve obtained after performing a static indentation test on fused quartz [49].

By applying the formula of the method described by Oliver and Pharr [50], which comes from the theory of Hertz for the elastic contact, the Young's modulus of the sample tested can be calculated:

$$E_r = \frac{\sqrt{\pi}S}{2\sqrt{A}} \tag{1.1}$$

where S is the contact stiffness and A is the indenter contact area. S can be obtained easily by calculating the slope of the first part of the unloading curve.

The hardness (H) can also be calculated based on its definition:

$$H = \frac{P_{max}}{A} \tag{1.2}$$

where P_{max} is the maximum load applied by the indenter and A is the projected area of the hardness impression [50].
To obtain a map (image where the color of each pixel represents the Young's modulus value obtained for this indent), there are two limitations. The first one is the space between two indents which need to be sufficient and the second one is the fact that this technique is time consuming [51].

1.2.2 High load fracture

In bones, microcracks can appear due to the daily loading. That is why it is interesting to look at how cracks propagate in their structure. For this purpose, high load indents are performed. The goal is to make an indent that creates cracks and to observe their propagation. The indents are made with a sharp diamond tip, a Berkovich one, bigger than the one used for nanoindentation in order to create observable cracks [52]. The load function applied to the tip had a triangle shape. Its peak value is determined in function of the penetration of the tip. In a material the crack is supposed to propagate in a straight line. An example of an indent performed in a cortical human bone is shown in FIGURE 1.20.

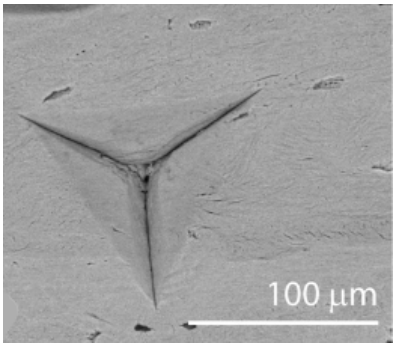

Figure 1.20: Example of a high load indent perform with a Berkovich tip in human cortical bone (adapted from [53]).

1.2.3 Modulus mapping

The mechanical behavior of a material is influenced by the structure and properties of all scale levels of this material. To investigate the nanoscale level different methods exist and among them the nanoindentation and the modulus mapping. The modulus mapping was created to improve the nanoindentation technique which allows to measure mechanical properties (hardness, contact stiffness and local Young's modulus) of a sample. This method of nanoindentation has limitations. Indeed, at the nanoscale, the areas of interest can be small. The problem is that the size of the indents can exceed 1 µm, which means that certain characteristics that could be interesting are not measurable (for example the thin

lamellae which have a thickness of 1 µm as seen previously). Moreover, depending on the penetration distance, plastic deformation can appear which can distort the calculation of the Young's modulus [54]. The modulus mapping was then created to overcome these weaknesses. This technique allows to obtain quantitative information about the distribution of several mechanical properties of a sample such as storage modulus with a high spatial resolution (in the order of 20 nm) on a window of a few micrometers [55]. For this purpose, the machine is equipped with the same tip which is used for nanoindentation. It combines nanoindenter with a force modulation system. For the modulus mapping, the tip is subjected to a weak static force (F_{DC}) and it scans the sample thanks to a piezoscanner which will be introduced in the SECTION 2.3.1. Since the static force is low, the tip only penetrates a few nanometers into the surface, which means that no plastic deformation is created and the surface remains intact after the measurement. Furthermore, this allows a high spatial resolution as the contact air between the surface and the tip remains small. Thanks to this force and the piezo scanner that scans the area, it is possible to obtain the profile of the height. An oscillating force (F_{AC} show in black in FIGURE 1.21) is added to this static force. The oscillating force must always have a smaller amplitude than the static force to ensure continuous contact with the surface. The frequency of this force is given by $f = \omega/2\pi$ with ω the period. The static force allows to stay in contact with the surface and the oscillating force rastes the surface and allows to obtain viscoelastic data of the sample. The displacement of the tip (show in green in FIGURE 1.21) is analyzed to obtain its amplitude U_o and its phase shift δ which will be used through calculations explained in SECTION 1.2.4 to obtain the storage and loss modulus. The storage modulus is the real part of the Young's modulus and represent the elastic contribution and the loss modulus is the imaginary part and represents the viscoelastic contribution.

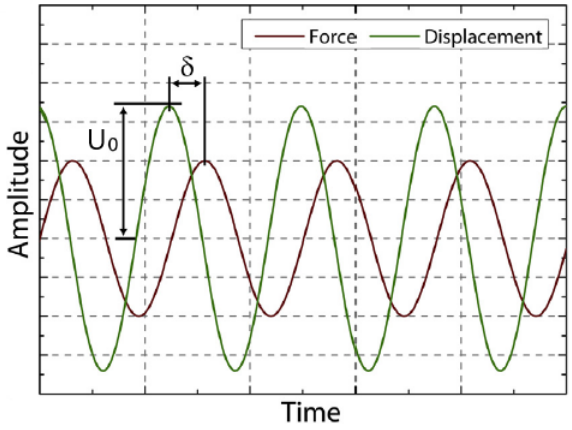

Figure 1.21: Representation of the force applied and the corresponding measured displacement of the tip (adapted from [54]).

This method is very interesting for biological materials because of its resolution. Indeed, these materials are very heterogeneous at different length scales, especially at the nanometer level, which means that they have a complex structure. The modulus allows to measure the mechanical properties of the different regions of this structure which can vary strongly from stiff to smooth, for example.

1.2.4 Equations of modulus mapping

Firstly, the displacement of the tip U can be described by the following standard differential equation of motion:

$$m\ddot{U} + C\dot{U} + KU = F_{AC}\exp(i\omega t) \tag{1.3}$$

where $F_{AC}\exp(i\omega t)$ is the periodic force applied on the tip, m represents the effective mass, C the effective damping coefficient and K the stiffness of the sample-tip configuration [56]. The solution of

this equation is given by the following periodic displacement:

$$U = U_o \exp[i(\omega t - \delta)] \tag{1.4}$$

By putting EQUATION 1.4 in EQUATION 1.3, the amplitude is obtained:

$$U_o = \frac{F_{AC}\exp(i\delta)}{K - m\omega^2 + i\omega C} = \frac{F_{AC}}{\sqrt{(K - m\omega^2)^2 + \omega^2 C^2}} \tag{1.5}$$

The contact stiffness K* is equaled to the ratio of the load and the displacement. By knowing the load applied on the tip and using the EQUATIONS 1.4 and 1.5, the variable can be calculated:

$$K^* = \frac{F_{AC}\exp(i\omega t)}{U} = \frac{F_{AC}\exp(i\delta)}{U_o} = K - m\omega^2 + i\omega C = K' + iK'' \tag{1.6}$$

where $K' = K - m\omega^2$ the real part of K* represents the storage stiffness and the imaginary part $K'' = \omega C$ represents the loss stiffness (elastic and viscoelastic components respectively).

The absolute value of this contact stiffness can be computed to measure its amplitude:

$$|K^*| = \sqrt{(K - m\omega^2)^2 + \omega^2 C^2} = \frac{F_{AC}}{|U_o|} \tag{1.7}$$

K' and K'' can also be expressed in another form using the formula z = a+ib with a = r cos(θ) and b = r sin(θ):

$$K' = |K^*|\cos(\delta) = K - m\omega^2 \quad \text{and} \quad K'' = |K^*|\sin(\delta) = \omega C \tag{1.8}$$

The phase shift visible in FIGURE 1.21 can be obtained using EQUATIONS 1.8 [51]. That gives:

$$\frac{K''}{K'} = \frac{\sin(\delta)}{\cos(\delta)} = \frac{\omega C}{K - m\omega^2} \Leftrightarrow \delta = \mathrm{tg}^{-1}\left(\frac{\omega C}{K - m\omega^2}\right) \tag{1.9}$$

By knowing $|K^*|$ and δ which are measured values and by using EQUATION 1.8, variables K and C can be calculated:

$$K = |K^*|\cos(\delta) + m\omega^2 \quad \text{and} \quad C = \frac{|K^*|\sin(\delta)}{\omega} \tag{1.10}$$

At this step, an hypothesis is used: the sample and the indenter can be represented by a Kelvin-Voigt mechanical equivalent model which is visible in FIGURE 1.22 [51, 54, 57].

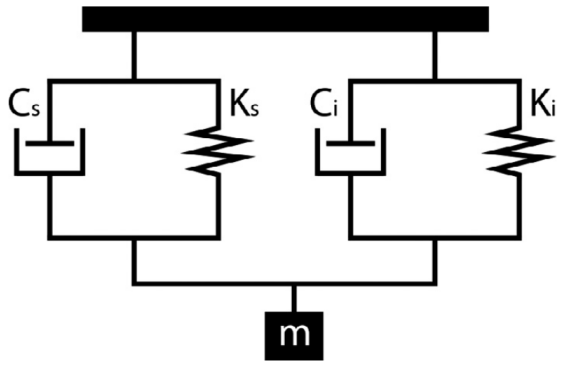

Figure 1.22: Representation of the sample and the indenter using the Kelvin-Voigt mechanical equivalent model with K_s and K_i the contact stiffness of the sample and of the indenter respectively and C_s and C_i the damping coefficients of the sample and of the indenter respectively (adapted from [54]).

The sample and the indenter are considered to be in parallel. Knowing this, the formula of the spring (K) and the damper (C) equivalent can be applied which gives:

$$K = K_s + K_i \quad \text{and} \quad C = C_s + C_i \tag{1.11}$$

with K_s and K_i the stiffness of the sample and the indenter respectively and C_s and C_i the damping coefficient of the sample and the indenter respectively. By using EQUATIONS 1.8 and 1.11, that leads to:

$$K_s = |K^*|\cos(\delta) + m\omega^2 - K_i \quad \text{and} \quad C_s = \frac{|K^*|\sin(\delta)}{\omega} - C_i \tag{1.12}$$

As for the contact stiffness, the Young's modulus can be expressed by two components: the storage modulus E' which represents the elastic part and E'' the loss modulus which represents the viscoelastic part:

$$E = E' + E''i \tag{1.13}$$

To go from storage and loss stiffness to storage and loss modulus, the Hertz contact mechanics which describes an elastic contact between a sphere (here the tip) and an elastic half-space (here the sample) are applied [54, 55, 56]. The relations between storage modulus and loss modulus with the contact stiffness and the damping coefficient are as follows:

$$E' = \frac{K_s}{2}\sqrt{\frac{\pi}{A_c}} \quad \text{and} \quad E'' = \frac{\omega C_s}{2}\sqrt{\frac{\pi}{A_c}} \tag{1.14}$$

where A_c is the area of the contact between the tip of the indenter and the sample when the tip applies a contact force F_{DC}. For a spherical tip, $A_c = \pi a^2$ with a the radius of the contact. By putting this information into the equations, they become:

$$E' = \frac{K_s}{2a} \quad \text{and} \quad E'' = \frac{\omega C_s}{2a} \tag{1.15}$$

with $a = \left(\frac{3RF_{AC}}{2K_s}\right)^{1/2}$ where R represents the radius of the tip. By putting this value in EQUATION 1.15, the reduced storage modulus of the sample can be know:

$$E_s = \frac{K_s^{3/2}}{\sqrt{6RF_{AC}}} \tag{1.16}$$

The storage modulus obtained correspond to the reduced modulus E_r. The calculation of E_r involves the tip of the indenter parameters and the parameters of the samples investigated. The formula is the following:

$$\frac{1}{E_r} = \frac{1-\nu^2}{E} + \frac{1-\nu_i^2}{E_i} \tag{1.17}$$

with E_i and ν_i the Young's modulus and the Poisson's coefficient of the tip and E and ν the Young's modulus and the Poisson's coefficient of the sample. Often, if the tip is in diamond, E_i » E and EQUATION 1.17 can be simplified:

$$E = E_r(1-\nu^2) \tag{1.18}$$

To apply this procedure, several parameters of the indenter tip (C_i, K_i, m and A_c) are needed. To find them, a calibration of the system is necessary before performing a modulus mapping. It consists of the application of a periodic force ($F_{AC}\exp(i\omega t)$) on the tip which is in the air, i.e. not in contact with a sample. The frequency ($f = \frac{\omega}{2\pi}$) of this force will then vary between 10 and 300 Hz. During this time, the amplitude of the movement of the tip is recorded and finally a graph of this displacement as a function of angular frequency (ω) is generated. This displacement is represented by the same equation (EQUATION 1.5) used for the modulus mapping. By fitting this equation with the experimental data curve, the coefficients C_i, K_i and m can be determined. An assumption is made in this calibration step: the mass m is considered to be constant during the measurement of mechanical properties [51, 55].

Another parameter that is also necessary to have to make the calculations is the radius of curvature whose value can change due to wear and tear and must therefore be recalculated every certain time. To obtain it, fused quartz, which is a material whose Young's modulus is known precisely, is used. An

indentation will be made in the unknown sample. On the load versus displacement curve, the displacement corresponding to the static force used to make the modulus mapping is retained. An indent is then made on fused quartz and thanks to the load vs displacement curve, the force corresponding to the displacement made in the unknown sample is obtained. A modulus mapping of the fused quartz is then done by applying the load found. The modulus mapping being done, the machine applies the EQUATION 1.16 but with the tip radius as unknown because the Young's modulus is known. And so the tip radius is identical for the unknown sample.

The contact theory of Hertz is used to pass from stiffness to storage modulus. This theory is based on several assumptions: the surface must be flat and smooth, its structure and composition must be homogeneous and only elastic contacts are present. Given these assumptions, the topography and inhomogeneity of a material can therefore lead to errors in the calculations. Indeed, since the tip only sinks a few nanometers, the topography has an important influence. To ensure a good topography, the grinding and polishing of the sample are crucial. Moreover, the sinking of this tip generates an elastic volume underneath it. It is this volume that must be elastic and homogeneous, which is not always the case. Finite element analysis can be used to simulate the process and to study the influence of inhomogeneity, topography and plastic or elastic deformations. If some values seem suspicious, these simulations can explain what is going on.

1.3 Scanning electron microscope

Scanning electron microscope (SEM) is a microscope using electron to scan the surface of materials at high resolution in the range of 1 µm to 1 nm [58]. This technique allows to investigate the topography and the morphology of the surface and the chemical composition of the studied sample. The method uses an accelerated electron beam as a source to produce the images.

Several signals can be emitted by the interaction between the electron beam and the studied sample depending on the atomic number of atoms, their concentration and the energy of the electron beam that is sent. Among them, there are secondary electrons (SE), backscattered electrons (BSE), visible light or X-rays (left on FIGURE 1.23). The signal will be picked up by a detector which will give different information depending on the type of signal received [59, 60].

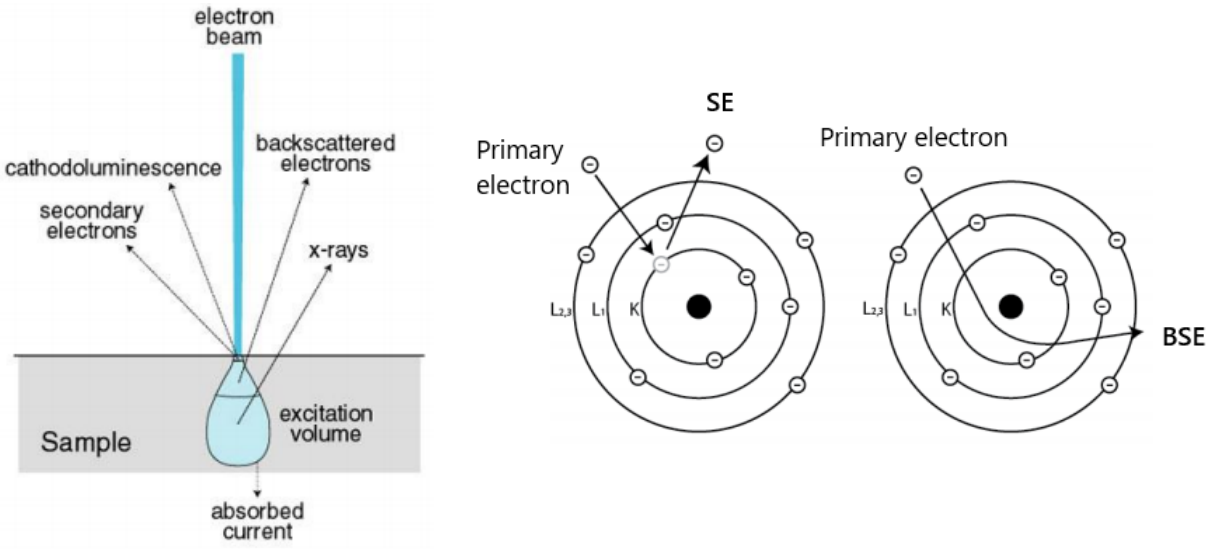

Figure 1.23: From left to right: different interactions between the incoming electron beam and the sample studied and generation of secondary and backscattered electrons (adapted from [61]).

In this master thesis, SE and BSE were used. The SE provides information about the morphology and the topography of the surface of the sample studied while the BSE gives compositional contrast information. For SE, the electron beam is used as energy to release electrons of the sample, called secondary electron, by transferring energy to them. These electrons are the ones that are on the K-shell. A specific detector is used to capture and collect them to reconstitute the image of the topography or the morphology of the surface. Indeed, since they have a rather low energy, only the electrons close to the surface are emitted. The intensity captured by the detector depends on the number of second electrons that arrive on it. The vacuum must be made in the microscope to avoid any interaction of second electrons with molecules present in the air [59].
BSE corresponds to the primary electrons that have been sent to the sample and that are deviated and returned by the nucleus of atoms of the sample (right on FIGURE 1.23). BSE are backscattered depending on the atomic number [61]. The angle of deflection is a function of the atomic number Z of the atom and depending on that the contrast differs because the heavier elements will re-emit more electrons than the lighter elements, which makes them appear brighter. They will then be captured by a detector placed in front of the sample since the BSE are only slightly deviated. The images thus produced give an indication of the contrast of the sample composition at the atomic scale [59].

The system, shown in FIGURE 1.24 is composed of several parts. The three main ones are the electron gun, the magnetic lenses and the scanning coils. The first one is the part that generates the electron beam which can have different energies. Electrons can be produced by two types of sources: thermionic emitters or field emitters. For the first one, a current flows in a filament of tungsten to heat up it. When the heat reaches a certain threshold, the electrons escape from the material. For the second type, a filament of tungsten is used, a huge electric field is applied to it and electrons are emitted [59, 61].

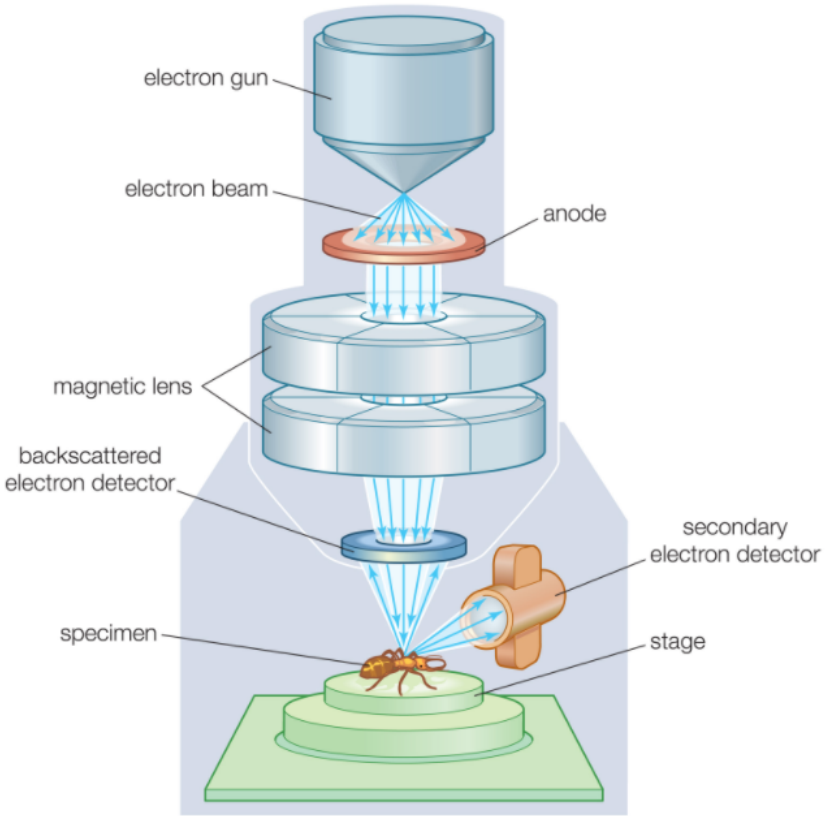

Figure 1.24: Schema of the SEM instrument [62].

For the second component, magnetic lenses consist of solenoids. A current is applied to these coils and it generates a magnetic field. Its role is to condense or deflect the electron beam. Just before the sample, an objective lens is placed. This one, thanks to magnetic fields allows to command the final focus of the

electron beam. An aperture is also added to refine the beam if necessary. The last one is the scanning coils. There are used to scan the samples by deflecting the electron beam in a zigzag fashion [59, 61].

1.4 Main aim of this master thesis

As seen in this background, fibrolamellar bone is a very interesting structure because of its ability to grow quickly while presenting high mechanical properties. Indeed, it must be able to support the weight of large animals. The structure of this bone is relatively unexplored but a consensus has been established through recent studies. However, the mechanical properties have hardly been studied. An investigation of these at the nanoscale would be useful to complete the information about the structure already available in literature. For this purpose, a recent technique, little used but with many advantages seems appropriate: the modulus mapping. The objective of this master thesis is therefore twofold:

1. The first goal is the investigation of modulus mapping method. This one being complex, the implementation of a protocol of use is necessary to guarantee the consistency of the results on bones.
2. The second aim is to investigate a fibrolamellar bone unit through different tests:
    - Scanning electron microscope to highlight the topography and the chemical composition.
    - Static indentations to get an idea of the distribution of the Young's modulus of the different parts constituting the fibrolamellar bone.
    - Modulus mapping to map with high lateral resolution the storage modulus of all features of a unit.
    - High load indentations to see the propagation of cracks in the different part of a unit.

After this work, the goal is to have a protocol for using modulus mapping that works on bone and to know more about the mechanical properties of fibrolamellar bone at the microscopic level.

Chapter 2

Material and method

2.1 Introduction

The purpose of this chapter is to describe the experimental parts that have been performed for this master thesis. The first part was the collection and the preparation of the samples for the modulus mapping and for the scanning electron microscope. The preparations for these different techniques differ at the final step. After that, the implementation of the modulus mapping protocol is explained and this one is written at the end.

2.2 Samples preparation

To realize these experimentations, bovine bones were used for several reasons. The first are the fact they are easily available and their use does not pose any ethical problem. Moreover, since bones of cows are relatively big, the features of the structure are readily visible.

The protocol followed in this work was put in place and is used at Ludwig Boltzmann Institute of Osteology in Vienna. The researcher Markus Hartmann helped us in the implementation of this protocol [63]. This very precise way of preparing the bones has to aim to reduce the risk of the formation of microcracks that could be seen under the microscope and that could change the mechanical properties of the sample. A second goal is to obtain very flat surfaces to perform modulus mapping on them. Indeed, a too high roughness could cause artifacts during the measurement.

2.2.1 Collection of samples

The samples came from a local butcher located near the Sart-Tilman (the Mosanne butcher). Two cows' femurs were collected. The age of these animals was not known. The fresh bones were directly cut the day of their collection to avoid their storage in the freezer which could cause the formation of microcracks inside.

2.2.2 Sample cutting

After obtaining the bones, they were cut at the Faculty of Veterinary Medicine with the help of Professor Marc Balligand. Fresh bones were divided into smaller samples with a band saw. Both heads of the femur were removed and then transverse sections were made in the diaphysis of the femur. Finally, these slices were cut into two centimeters side cubes. These different steps are shown in FIGURE 2.1. It

is important to use the band saw very carefully. Some materials are taken to push the bone in order to avoid any contact between the blade and the fingers.

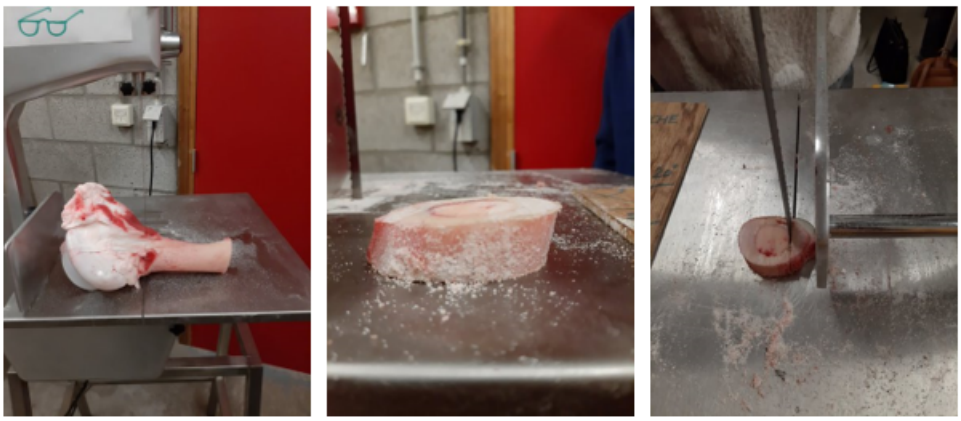

Figure 2.1: Illustration of the sample cutting. From the left to the right : removal of the heads, slice of the diaphysis of the femur and cut of the slice into small cubes.

After obtaining these pieces, samples were cut with a low-speed diamond band saw (BUEHLER ISOMET) into small cubes with an average length size of 1 cm. The speed of the diamond band was 300 rotations per minutes (rpm) and it was constantly irrigated with distilled water. In this step, glycol was not used because the microcracks that water could have caused are removed by polishing at the end of the process.
It is important to take notes on how the bone was cut (which transverse section) and from where in this section (anterior/posterior) because the load is not the same in the entire bone due to remodeling which can lead to differences in mechanical properties within the same bone. This step was not performed during the bone sample preparation due to an omission. This is a point to improve in future work.

2.2.3 Sample dehydration

Samples were dehydrated in ascending grades of ethanol, acetone and methylmethacrylate (MMA) solutions by following the protocol below:

- day 1: ethanol 80%
- day 2: ethanol 96%
- day 3: ethanol 100%
- day 4: ethanol 100%
- day 5: ethanol 100% + acetone (1:1)
- day 6: acetone
- day 7: ethanol 100% + acetone (1:1)
- day 8: ethanol 100%
- day 9: ethanol 100%
- day 10: MMA
- day 11: MMA

Each step was performed at room temperature. The last two steps with MMA were made under a fume hood given the strong odors.

The bones must be dehydrated to allow a better infiltration of the resin which is hydrophobic [64]. But dehydrating the bones has an impact on the mechanical properties of the bones. Indeed, it is well documented in the literature that dehydrated bones are more rigid than wet bones. It is therefore important to take this into account when comparing the values in the literature to be consistent.

2.2.4 Sample embedding

Once the samples were dehydrated, they were embedded in resin. The composition of this resin for 500 milliliters (ml) was the following:

- 400 ml MMA
- 7 grams (g) Benzoylperoxid (BPO)
- 100 ml Nonylphenylpolyethyleneglycol acetate

BPO was used as a starter for the polymerization. It was supplied with 25% water. To be exploited, it must be dried for 24 hours at 30-35ºC in an incubator before dissolving it in MMA. Special attention should be paid to BPO when it is dry because it becomes more explosive.
To realize the medium, MMA and BPO were first mixed and after, the nonylphenylpolyethyleneglycol acetate was added. This last one was used as a softener.
Once the medium was ready, the bones were first placed in the molds provided for this purpose (FIGURE 2.2) and resin was added. The resin should flow on top of the bone, at about 1.5 centimeters (cm) to avoid problems of evaporation and strengthening of the resin on top of the bone which would cause the bone not to be longer embedded entirely in the resin. The molds must be sealed using paraffin to ensure that the resin does not leak underneath. In addition, they must be covered with paraffin as well to prevent evaporation, especially in the incubator (FIGURE 2.2).

Once the molds were ready with the samples, they were placed first in the refrigerator and then in an incubator. Samples were stored for two days at a temperature of 4°C in the refrigerator. After that, they were moved to an incubator for five days. The first two days, the temperature was 34°C. Then it was increased to 42°C for the next two days and finally for the last day it was increased to 50°C.

In the incubator, the temperature was increased step by step to avoid the formation of bubbles which can happen when the temperature becomes initially too high. The temperature to start the polymerization is 34 °C. Moreover, also to avoid the formation of bubbles, not more than 8 samples can be put at once in the incubator. Indeed, the polymerization reaction being exothermic, if too many samples are placed at the same time in the incubator, the temperature will increase too quickly which can cause the formation of bubbles as said just before. [63]

Figure 2.2: Illustration of the embedding process of samples. From left to right : cylindrical mold with sample inside, paraffin and embedded samples obtained.

2.2.5 Sample grinding & polishing

The last steps of the protocol of the samples preparation were the grinding and the polishing.
The first thing to do was to remove the samples from the mold. For that, the use of a scalpel has been helpful. Once they were taken away, the top of the sample was cut with the same diamond saw used in the SECTION 2.2.2. This step can be seen in FIGURE 2.3. This cut is necessary for two reasons. First,

on top of each sample, a layer of about 4 mm had not cured as it should, this layer had remained a little slimy. Hence it had to be removed by cutting. Secondly, this cut also allows to free a part of the sample from the resin. It is this section which was polished and then analyzed.

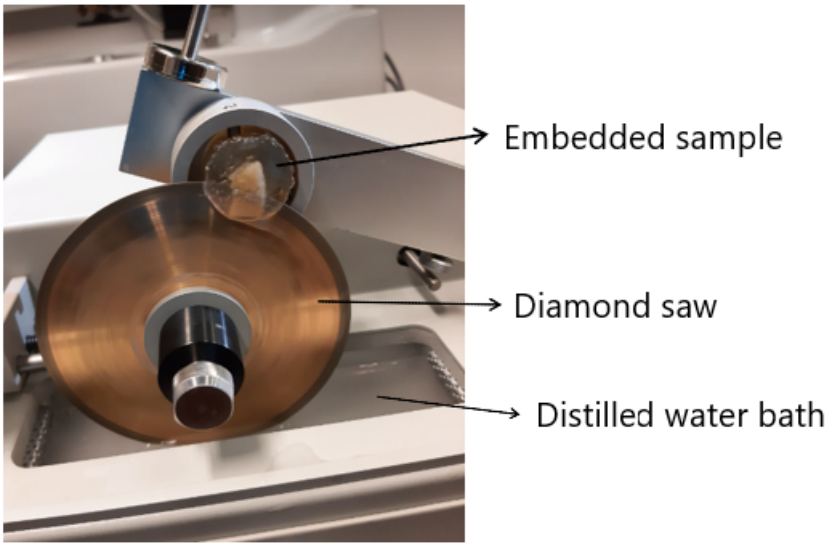

Figure 2.3: Illustration of the diamond saw cut.

After that, the grinding and the polishing were performed with the machine BUEHLER METASERV 250.

Firstly, samples were ground with a carbide paper P1500 at 20 rpm for three minutes and after with a paper P2500 (which corresponds to smaller grains than the P1500) also at 20 rpm for three minutes under ethylene glycol irrigation. Glycol was added approximately every fifteen seconds to ensure proper lubrication and, removal of particles produced by grinding.

Secondly, the polishing was performed. To do this, a first polishing was done with a 3 µm diamond spray (diamond suspension in alcohol) on a silk cloth at 45 rpm for six minutes. Finally, a second polishing was done with a 1 µm diamond spray on a silk cloth at 35 rpm for seven minutes. During the polishing, a force of 10 N was applied with the machine on the sample to ensure a good and uniform polishing.

The diamond suspension was sprayed about every 30 seconds to ensure proper lubrication. However, another method would be preferable: put spray once on the silk disc and wait for the alcohol to evaporate, then polish on this disc under glycol irrigation again. This other method allows to avoid a prolonged contact of the sample with the alcohol which decreases the risk of microcracks formation. However, having used the first method, we did not observe a high density of cracks which means that the polishing has been correctly performed anyway.
After several tests of modulus mapping, a second polishing was conducted to try to improve the results obtained with this test. For that, the second method was employed. No great difference was obtained, the results still seemed to be of high quality (the RMS roughness passed from 5.6461 nm to 5.8641 nm for a flat region).
Care must be taken to ensure that the samples are not too thin, otherwise they will pass between the disc and the machine. Therefore, they are not polished and can also be damaged.

Finally, samples were cleaned manually. For this purpose, benzine and a silk fabric were used.

After this last step, samples were glued on a magnetic disk with epoxy glue. They could thus be analyzed.

2.2.6 Scanning electron microscope (SEM)

The samples were viewed under a scanning electron microscope. For this purpose, a short preparation of the samples was necessary to facilitate the visualization. They were coated with silver using the BALZERS SCD 030 and two tapes of carbon were added. These last ones are conductive and they allow to evacuate the negative charges on the ground due to the electron beam to avoid an overcharging of the sample. Without that, nothing would be visible, it allows to increase the contrast [58]. To coat the samples, they were placed in a tube. The vacuum was then made and the little remaining O_2 was replaced by argon. The reason for putting argon in the tube allows to control the pressure in this one thanks to the pressure of the bottle where the argon comes from. It also allows for proper control of the air constituents in the tube. The samples were placed between a cathode and an anode and on the top part was the silver. A current was applied and passed by the two extremities. This changed the state of the silver into plasma. This one then moved around and deposited on the sample. The duration of the application of the current allows to determine the thickness of the silver layer which is deposited on the sample. Silver was chosen not to interfere with the quantification of bone constituents because it does not contain any.

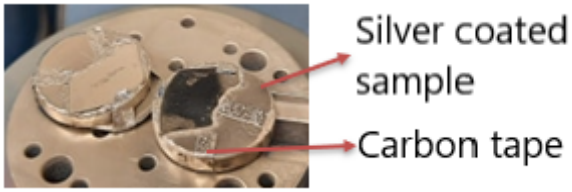

Figure 2.4: Illustration of silver coated sample.

A second treatment was done to highlight the orientation of collagen fibers. This is called etching and for this, HCl 1% acid was put for two seconds on the bone sample. This acid allows to dissolve a part of the minerals present in the bone and the collagen fibers are then highlighted.

Then a scanning electron microscope (XL 30 ESEM-FEG) was used. It was put in a low vacuum and an accelerating voltage of 15 kV was applied. Results obtained with this microscope are shown in the CHAPTER 3.

2.3 TriboIndenteur

The machine used to perform tests is the HYSITRON TI 980 TRIBOINDENTER. It allows to carry out several nanomechanical testing. For this thesis, static indentations, modulus mapping and high load fractures tests were applied.

2.3.1 System

The system is composed of different parts. Their functioning and role will be explained in this section.

Firstly, the machine is equipped with an automated X, Y and Z axis staging system. The motors that allow the movements in the three directions are controlled by micro-steps to have the most precise movement possible.
Moreover, the platform on which the samples are placed is magnetic which allows to make an attraction with the magnetic disk fixed on the back of the sample. Nine places where samples can be put are available. The defined locations help to avoid any risk of damaging the machine or the samples.

Secondly, a Z axis stage, a system composed by a piezo scanner and a transducer as well as an optical microscope system are mounted on a granite frame. This frame has several advantages: it contributes to thermal stability of the instrument and reduces environmental noise and resonant frequencies.

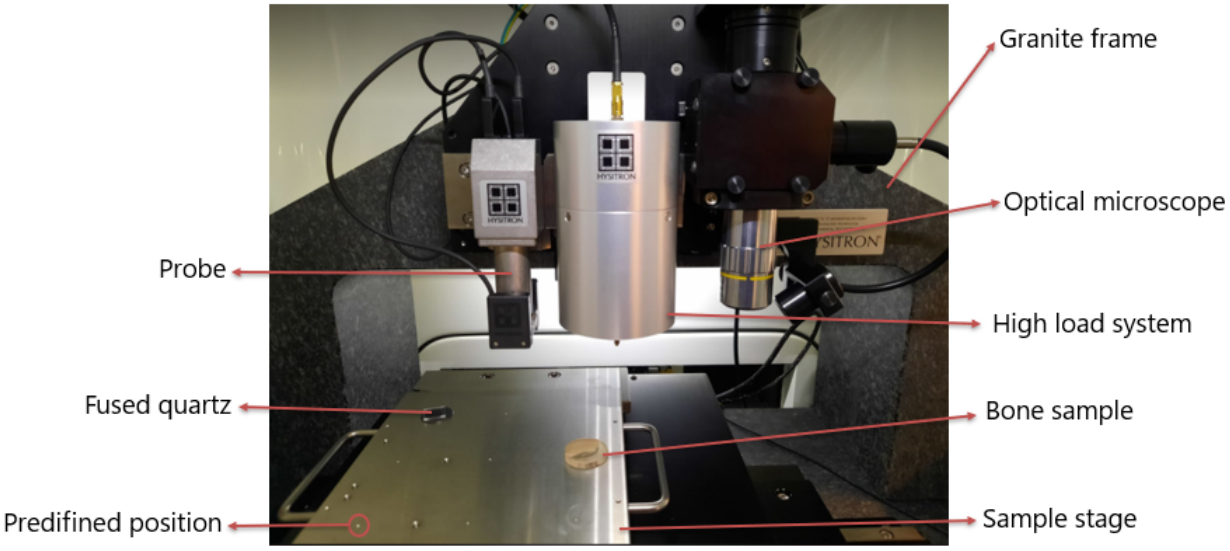

Figure 2.5: Illustration of the Hysitron TI 980 TriboIndenteur.

Thirdly, the instruments are housed in an acoustic enclosure that minimizes the amount of acoustic noise and blocks drafts.

Fourthly, there is an active vibration isolation system. This part is very important due to the fact that the measurements made are very precise and sensitive which means that little perturbation can disturb them. Active refers to a system that reacts dynamically to the vibrations. The system is located below the granite frame and is composed of 2 rails which are on each side of the granite base. Four piezo-electric accelerometers are put in each rail and are placed in different orientations to capture change in all degrees of freedom. They allow to detect variations through a feedback loop. Feedback systems are made to correct incoming vibrations in a continuous way. At low frequencies (between 0 and 200 Hz),

the vibrations felt by the accelerometers are rectified thanks to four electrodynamic transducers which send compensating vibrations. If it is at a higher frequency, there is no more active correction but a passive one which is done with a stiff metal springs and the granite frame mass [65, 66].

On the granite bridge, as said before, there are three instruments fixed as it can be seen in FIGURE 2.5. They are used to perform static indentations, high load fractures and modulus mapping.

The first one is the optical microscope. This system allows to see the sample with a zoom of time 20. An additional zoom from time 1 to time 10 is possible in the TriboScan system which permits a total zoom from 20 to 200. To obtain images, an optic illumination is needed [66].

The second one is the high load system. It is composed of a diamond tip, sharp, which is larger than the one used for modulus mapping and static indents. It allows to make indents that create cracks in the samples.

The last one is the assembly of a piezo scanner and a transducer. The piezo scanner allows to approach the tip close to the sample in a very precise way giving an accurate final positioning before starting measurements. The accuracy given by this piezo scanner is higher than the one allowed by the sample stage. This is why, when the probe is close to the sample, the piezo scanner controls the positioning. It is used to perform Scanning Probe Microscopy (SPM) imaging of the sample but during nanoindentation, it stays stationary. The piezo scanner is composed of a piezoelectric ceramic tube as it can be seen in FIGURE 2.6. The inverse piezo effect of ceramic is used: voltage is applied to the ceramic which induces deformation of it [67]. The tube is cut horizontally, resulting in an upper and a lower part. The upper one is again cut in four parts which gives quarter cylinders. Each quarter allows to precisely control the movement in one direction: X, -X, Y and -Y. The movements in these directions are possible because when a voltage is applied to one of the parts, it extends along the main axis of the cylinder which bends. The lower part is entirely dedicated to control the movement according to Z. If the voltage is applied to this part, it extends which allows a movement according to Z.

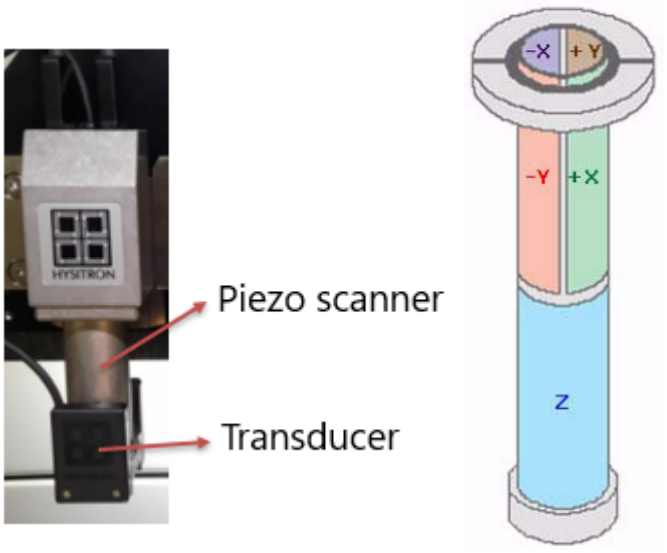

Figure 2.6: From left to right: Picture of the transducer mountained on the piezo scanner and illustration of the piezo ceramic tube construction [66].

The transducer is mounted on the piezo scanner. Its role is to measure the displacement of the tip. This is possible thanks to three-plate capacitive force/displacement transducer shown in FIGURE 2.7. It is composed of two outer plates in the middle of which is the central plate, connected to the structure by springs. These allow the motion of the central plate at which the probe is fixed [57]. This configuration

permits to give high sensitivity and a linear force or displacement output signal [66].

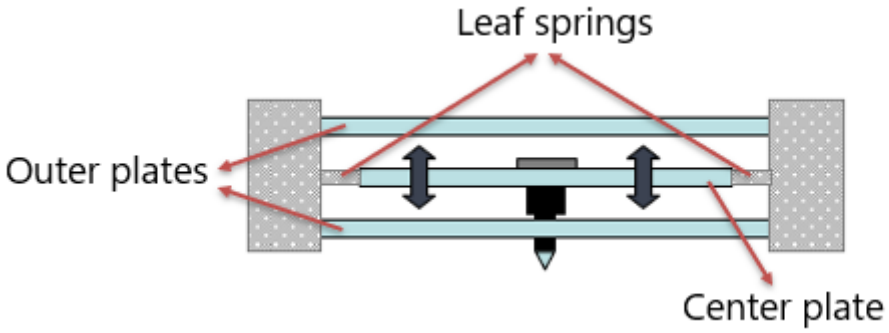

Figure 2.7: Cross-sectional scheme of the three-plate capacitive force/displacement transducer (Adapted from [68]).

The measurement of the displacement works in the following way. The central plate picks up a voltage that is applied to the two outer plates. These voltages have the same amplitude but they are in phase shift which is equal to 180°. This means that they are opposite. The displacement of this central plate between the two other ones can be obtained by measuring the voltage amplitude at the center plate. This captured voltage amplitude will be changed into a DC signal by the drive circuit board. This signal is equal to zero when the center plate is exactly in the middle of the outer plates. It will change and become positive or negative depending on whether the center plate is attracted to the lower or upper outer plate. The displacement of the probe is then obtained thanks to a relation that links the voltage amplitude and the position of the center plate between the two outer ones [66, 69].

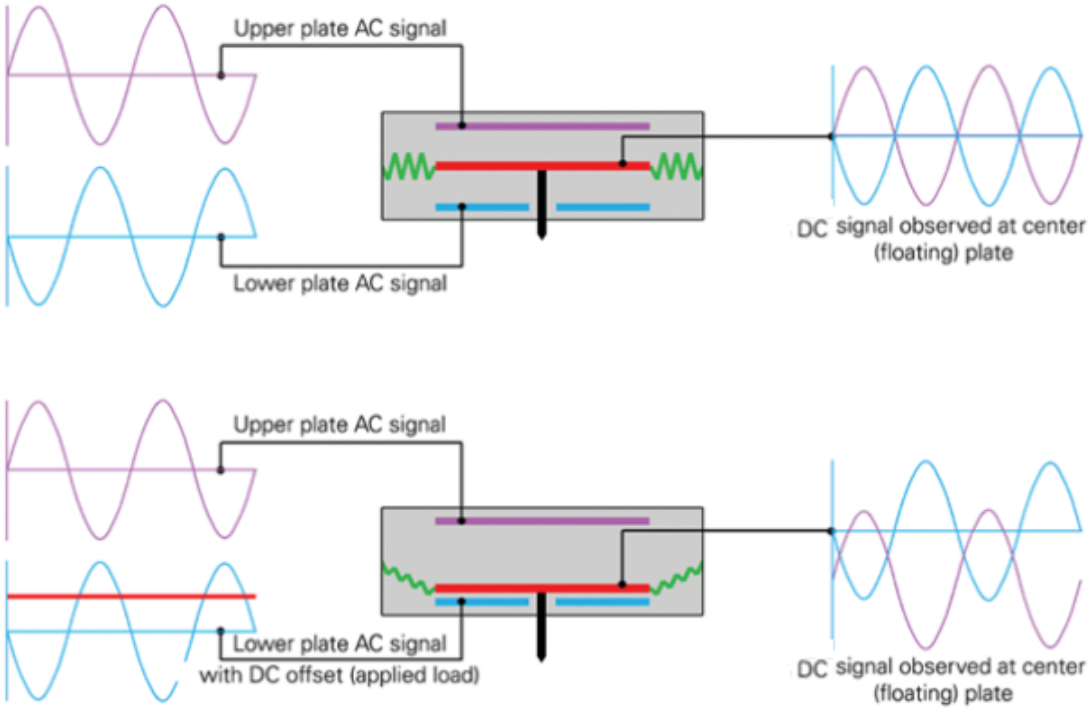

Figure 2.8: Schematic explanation of the operating three plate capacitive transducer [69].

2.4 Modulus mapping

Initially, several measurements were made on the bones but the results were not conclusive. Firstly, the values obtained for the storage modulus were much higher than those known for bone. Indeed, the mean value was around 80 GPa while the average real value is between 20 and 30 GPa [70]. Secondly, the results were not reproducible since two tests done at the same place with the identical parameters did not give the same values. It was decided to work first on fused quartz to be able to establish a protocol and study the influence of the parameters.

2.5 Modulus mapping on fused quartz

Firstly, tests were performed on fused quartz because it has several interesting properties such as its high chemical purity and its high resistance [71]. The purity makes it very flat after polishing which is really interesting to test several parameters because the results will not be influenced by the topography. Since the fused quartz comes from the company Hysitron and is given as reference for the nanoindenter, we know that the polishing which has been done by them is of high quality. Moreover, properties of the fused quartz are well known such as the young modulus which is equal to 69.6 GPa [66]. By knowing this information, results can be analyzed and if they match the theoretical values, it means that the method works.

To perform a modulus mapping, there are two kinds of parameters that must be taken into account. The first category consists of the imaging parameters and the second one is the parameters which are related to nanoscale Dynamic Mechanical Analysis (nanoDMA). The next section describes these parameters and explain how they were chosen.

2.5.1 Imaging parameters

There is a list of parameters that represent all physical properties of the SPM image. They are the following: scan rate (S_R), scan size, set point and integral gain.

- **Scan rate**: it represents the number of back and forth performed in one second so it defines the speed of the probe. The value of this scan rate can go from 0.01 Hz to 12 Hz. The basic value is equal to 1 Hz to perform a scan. The lower the scan rate, the better the resolution because the machine will spend more time on the same area and conversely, the higher the scan rate, the worse the resolution will be and streaks may appear.
- **Scan size**: it represents the size of the windows that will be scanned. This window can be up to 60 µm in size.
- **Set point**: it represents the force applied on the surface of the sample when the probe is in contact with it. The default value is 2 µN.
- **Integral gain**: it represents the feedback loop between the transducer and the piezo scanner. The default value is 240.

2.5.2 Specific parameters of the modulus mapping

Different parameters are involved in modulus mapping: frequency (F_{AC}), load amplitude, lock-in time constant and low pass filter.

- **Load amplitude**: it represents the dynamic force imposed on the probe during the measurement. This one can go from 0.001 µN to the maximum force allowed by the transducer. The basic value is 2 µN and must always remain below the value of the set point. If the value exceeds the set point, it could cause the loss of contact with the surface.

- **Lock-in time constant**: it represents the length of time the lock-in remains on a signal before changing it. This means that it is the time during which the signal will be recorded and over which it will be averaged. If the value of this parameter is too high, the time over which it is averaged will be too large and this will decrease the lateral resolution, streaks may appear. If the value is smaller, the lateral resolution is improved but the measurements may contain too much noise because it is not averaged over a long enough time. It is therefore necessary to find an appropriate lock-in time constant to have a compromise between these two different behaviors. Basic values are 3 or 10 ms.

  It is possible to calculate the lock-in time constant that best fits the parameters chosen for the measurements. For this, several points must be known.
  The first one is that when scanning a region, its size is a parameter that can be decided by the user. Nevertheless, this window will always be a square composed of 256 $\times$ 256 pixels. It is therefore the size of the pixels that will change. Secondly, since a line is traveled back and forth, the probe must travel 512 points to form a line.
  By knowing this, the time (t_{bf}) needed by the probe to scan one back and forth is equal to :

$$t_{bf} = \frac{1}{S_R} \quad [s]$$

  The time (t_p) spent at each location can then be calculated using this formula:

$$t_p = t_{bf} \cdot \frac{1}{512}$$

  To have a high enough resolution, the locking time constant should be one third of this value. This is to avoid averaging over too long a period and to have a high resolution.

- **Frequency**: it represents the oscillation frequency imposed on the probe. This frequency can be between 1 and 300 Hz and the default frequency is 200 Hz [66]. It can influence the resolution of the measurement. Indeed, to have a high resolution, the probe must make at least one oscillation or several at the same place. Therefore, there is a way to calculate the number of oscillations per pixel (N) which allows to verify that the frequency is high enough. It is as follows:

$$N = F_{AC} \cdot t_p$$

- **Low pass filter**: its role is to prevent the piezo scanner from moving (i.e. expanding or contracting) during the measurement. This low pass filter can be enabled or disabled by the user. To perform a modulus mapping, this filter must be enabled, as recommended by the user manual.

2.5.3 Calibration of the protocol

A whole series of tests were conducted for about one month and half to understand the influence of the different parameters. This allowed us to set up a protocol that gives consistent measurement. Consistent means that they are reproducible and that the values obtained are those expected.
In the rest of this section, the different tests carried out on the same fused quartz but at different locations are described and their results are given. One type of region tested in fused quartz can be seen in FIGURE

2.9. This picture shows that the fused quartz is really homogeneous since no features are visible. Only few points are present on the surface but they are impurities.

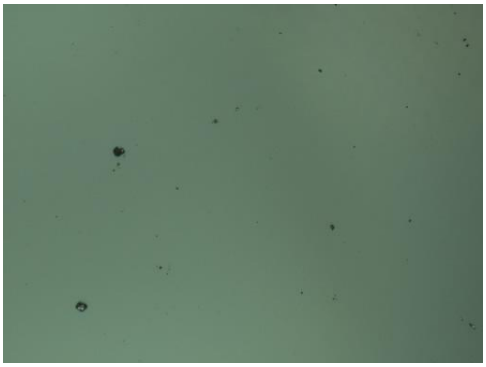

Figure 2.9: Optical microscopy image of a region of fused quartz.

Before performing each modulus mapping, a scan is done to check the root mean square (RMS) roughness and the global topography.

As a reminder, the RMS roughness is defined as the average of the height deviation of the mean value of the surface. The formula to calculate it is the following [72]:

$$\text{RMS roughness} = \sqrt{\frac{1}{n}\sum_{i=1}^{n}(h_i - h_{mean})^2} \tag{2.1}$$

with n the sample size, h_i the value number i of the height and h_{mean} the average value of the height.

First test phase

A first region was investigated. Its roughness was 1.2194 nm which is positive result since that means that the surface is flat. A modulus mapping was performed with the values recommended in the manual for the fused quartz. The parameters were:

- Scan rate = 0.2 Hz
- Scan size = 5 µm
- Set point = 4 µN
- Frequency = 200 Hz
- Load amplitude = 2 µN
- Lock-in time constant = $30 \cdot 10^{-3}$ sec
- Filter ON

This test was repeated four times on this region in order to ensure that the results were reproducible. Results are shown in FIGURE 2.10. For the height (FIGURE 2.10a), all four tests gave the same results. This makes sense given that the study area is the same for all four tests. For the amplitude (FIGURE 2.10b) which is the parameter measured by the machine, different results were obtained. That is not normal because measurements should be reproducible since the same parameter is measured at the same place. For the storage stiffness (FIGURE 2.10c), the graph is in mirror with the graph of the amplitude. This result is obvious since the EQUATION 1.6 seen before. For the storage modulus (FIGURE 2.10d), the histograms are centered on the same value but their height differs. The centering of the histograms can be easily explained by the fact that the storage modulus is calculated thanks to the tip radius which has been adapted so that the average value is 69.6 GPa, the known value of the young modulus of fused quartz.

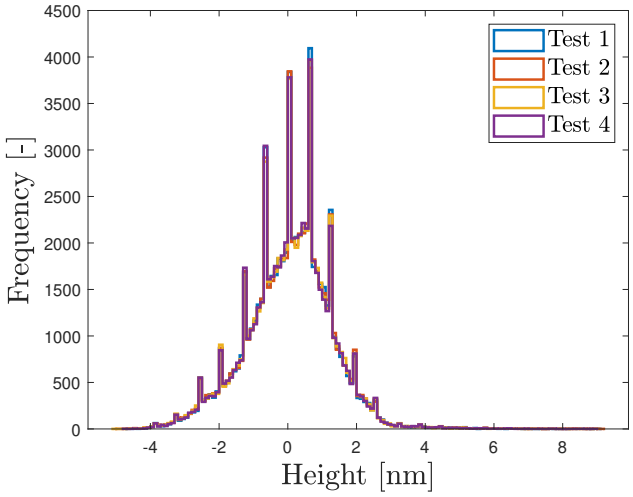

(a) Frequency distribution of the height [nm] for four same tests.

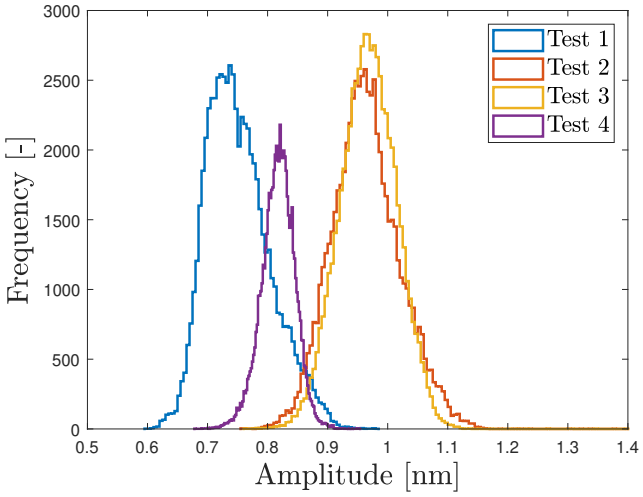

(b) Frequency distribution of the amplitude [nm] for four same tests.

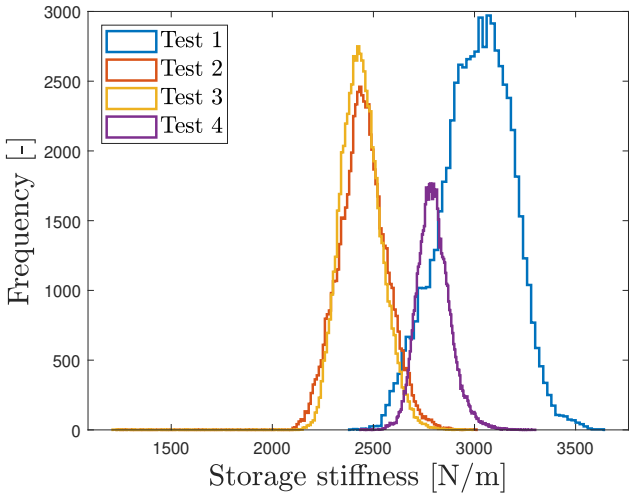

(c) Frequency distribution of the storage stiffness [N/m] for four same tests.

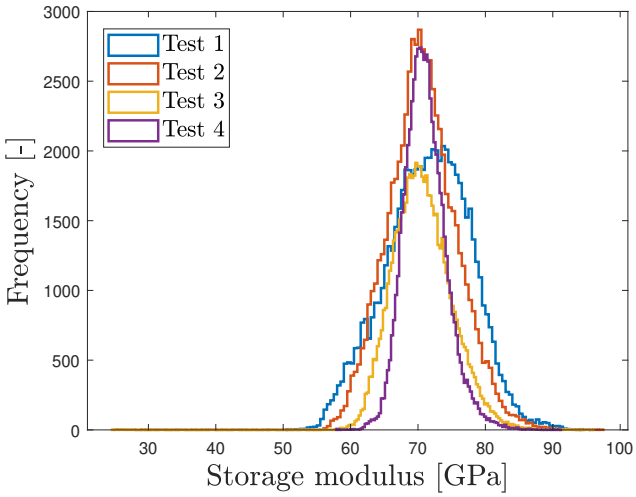

(d) Frequency distribution of the storage modulus [GPa] for four same tests.

Figure 2.10: Results obtained for the first test phase: Frequency distribution of the height, the amplitude, the storage stiffness and the storage modulus.

Second test phase

For these tests 2, a new region was analyzed. Its roughness was 1.2283 nm which again means that the surface is of high quality. To perform a modulus mapping, the scan rate and the lock-in time constant were changed with the aim of improving results. The scan rate has been changed from 0.2 to 0.1 to increase the resolution as explained earlier in the SECTION 2.5.1. The lock-in time constant was also changed because when performing the calculations shown in SECTION 2.5.2, we realized that the default value was too large. By applying the equation, the new value for the lock-in time constant was :

$$\text{lock-in time constant} = \frac{1}{3} \cdot \frac{1}{0.1} \cdot \frac{1}{512} = 0.006 \text{ sec} = 6 \text{ ms}$$

Results obtain with these new parameters are:

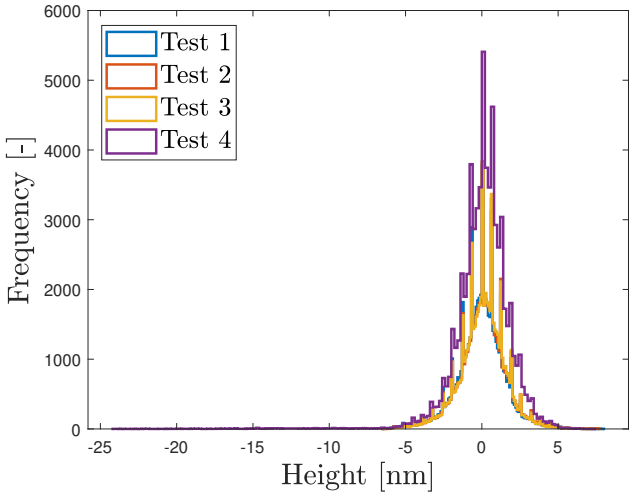

(a) Frequency distribution of the height [nm] for four same tests.

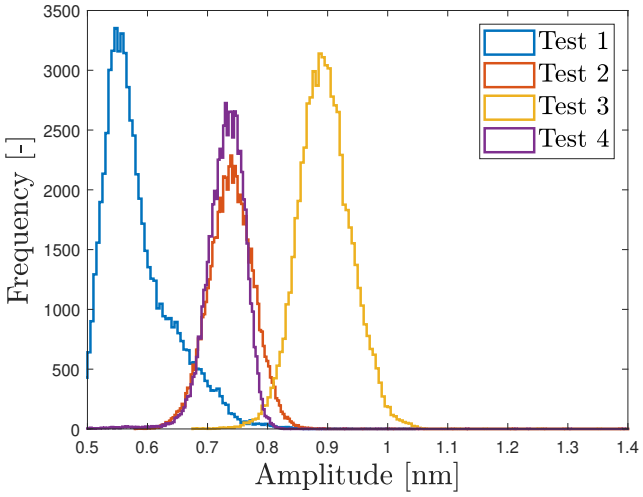

(b) Frequency distribution of the amplitude [nm] for four same tests.

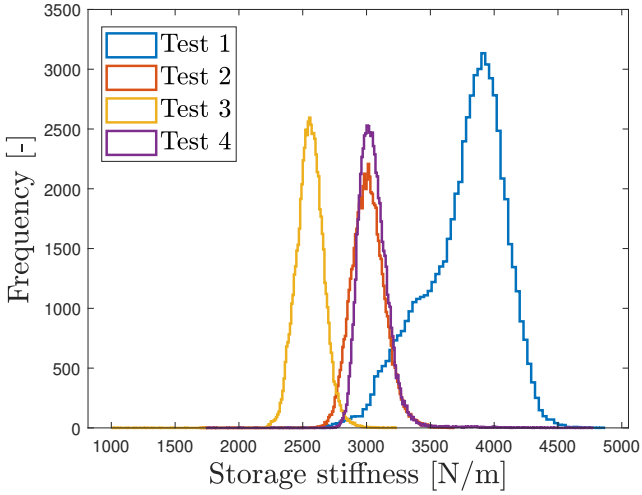

(c) Frequency distribution of the storage stiffness [N/m] for four same tests.

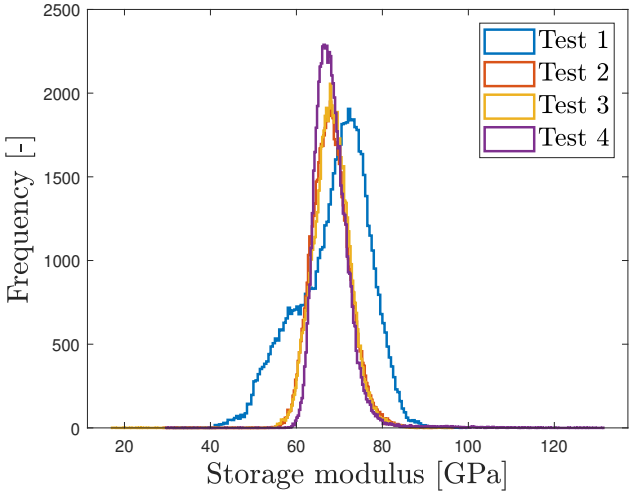

(d) Frequency distribution of the storage modulus [GPa] for four same tests.

Figure 2.11: Results obtained for second test phase : Frequency distribution of the height, the amplitude, the storage stiffness and the storage modulus.

Exactly the same observations as those obtained for the first test phase can be made. This leads to the conclusion that the parameters will not resolve the problem of reproducibility of the results. Another path was investigated in the following tests.

Third test phase

For these new tests, another approach was investigated. The goal of these measurements was to see if another method can improve the reproducibility of the results. In the previous tests, between each measurement, the tip was disengaged, i.e. it was lifted and therefore did not remain in contact with the surface. The new method is to always leave the tip engaged between each measurement. This ensures that the tip always starts in the same place. Indeed, if the tip is lifted, there will always be a drift of the sample which makes that the tip does not return to the same place.

A new region on the fused quartz with a roughness of 1.0694 nm was investigated with this new method. The same parameters as those used for the previous tests were applied:

- Scan rate = 0.1 Hz
- Scan size = 5 µm
- Set point = 4 µN
- Frequency = 200 Hz
- Load amplitude = 2 µN
- Lock-in time constant = $6 \cdot 10^{-3}$ sec
- Filter ON

Results obtained with this new method are shown in FIGURE 2.12

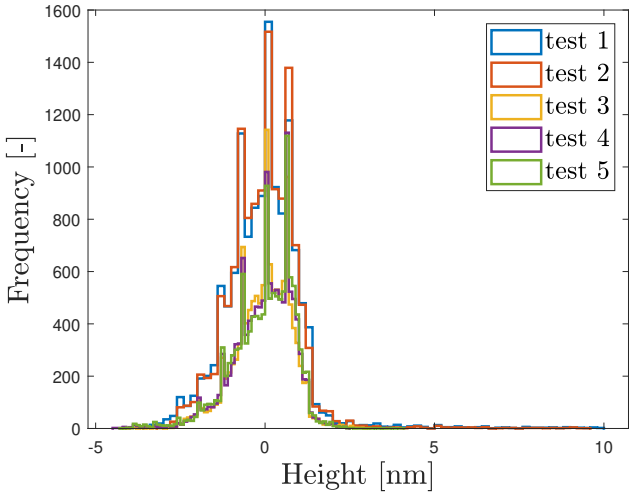

(a) Frequency distribution of the height [nm] for four same tests.

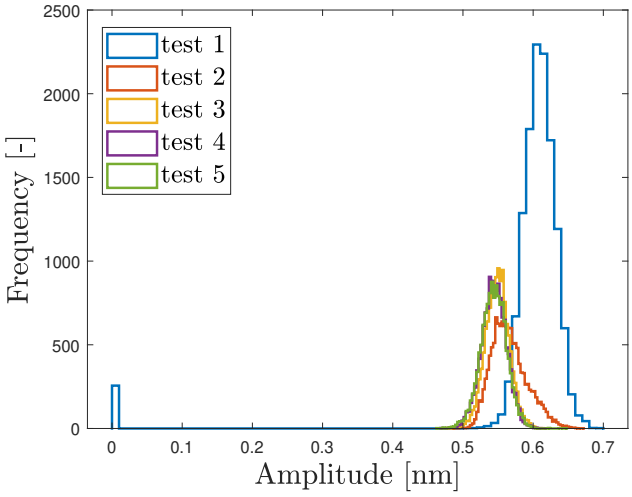

(b) Frequency distribution of the amplitude [nm] for four same tests.

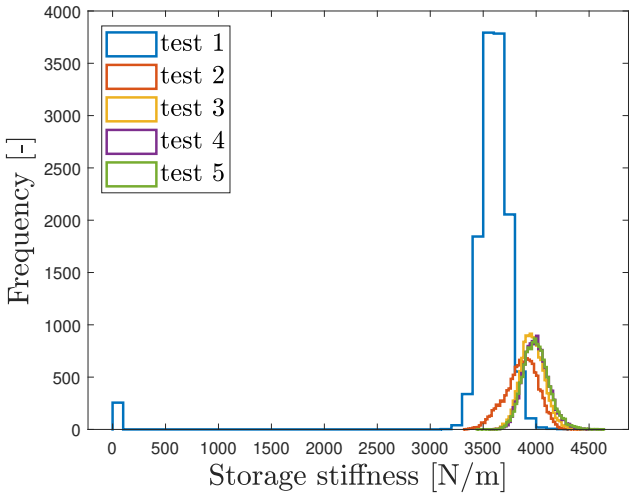

(c) Frequency distribution of the storage stiffness [N/m] for four same tests.

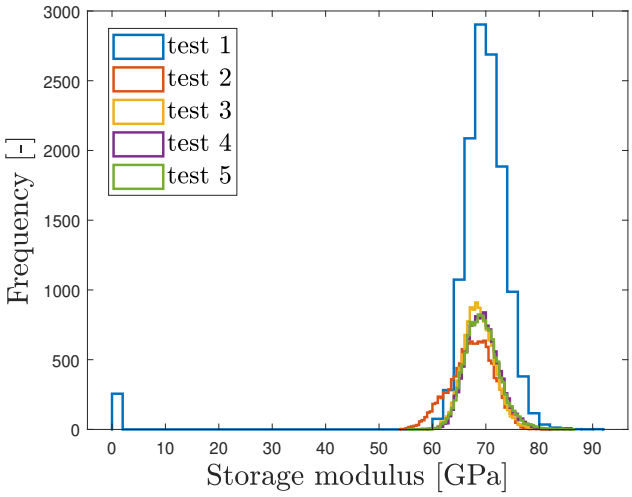

(d) Frequency distribution of the storage modulus [GPa] for four same tests.

Figure 2.12: Results obtained for third tests phase: Frequency distribution of the height, the amplitude, the storage stiffness and the storage modulus.

A point that stands out with these graphs is the fact that for all tests except the first one, the curves obtained are almost identical. These results are therefore consistent because they are reproducible. Only the first test is different from the following ones. This may be due to a problem of stabilization of the tip. This has been taken into account in the protocol established afterwards.

Thanks to numerous tests carried out over a month and a half on a bone sample and on fused quartz,

a rigorous protocol was created. This protocol allows us to obtain reproducible results with correct mechanical property values. This protocol is written in the following SECTION 2.6.

2.6 Protocol for the modulus mapping

Performing a modulus mapping is not so straightforward. A strict protocol has to be followed to ensure that the data are relevant. The steps to follow have been established on fused quartz by checking the results of numerous tests.

Before using the nanoindenter, the system must be calibrated and more particularly the transducer. This can be done in two steps. The first step consists of the calibration of the Indentation Axis. This calibration is done with the nanoindentation probe which performs an indent in the air so the instrument must be kept away from the samples to be sure not to touch them. This calibration is done with a load function in the shape of a triangle and with a peak force of 1300 N so that the displacement of the probe is in the range of 3.5-4.5 µm in the air. If the displacement is not in this range, the force must be adapted. Once the calibration is done, a graph giving the electrostatic force constant versus the displacement is generated. It is then compared with the fitted linear plot. The RMSE value that indicates the difference between the two is given. This value must be less than $5 \cdot 10^{-5}$ µN/V so that the calibration can be considered correctly conducted [66].

Before proceeding to the second step of the calibration, the tip was cleaned to remove all the waste, all the particles which could be on it. To do this, 3-4 indents must be made in the fused quartz. The load function chosen is the basic trapezoidal function with a force of 10 000 µN. This force is large enough to ensure that it goes deep enough into the fused quartz for the tip to be completely cleaned. Basic trapezoidal function represents a function which increases, stabilizes at the imposed force and after decreases until 0. This cleaning can also be done in the sample itself.

After this cleaning, the second calibration can be done. This second one is dynamic and gives as a result the calibrated value of the elements necessary to realize the modulus mapping: the spring constant in N/m, the mass in kilograms and the damping in kg/s. This calibration, like the first one, is performed in the air. The instrument must be far enough from the samples to ensure that it does not touch any samples during the process so as not to damage itself or the sample. The calibration is successful if the stiffness RMSE is less than 0.1 µ N/nm and the Phase RMSE is less than 1.0 ° [66].

Once the calibration and cleaning of the tip are done, the measurements can start. A scan is carried out for the first step. This one is performed with a scan rate of 1 Hz, a tip velocity of 10 µm/sec, a scan size of 5 µm and a set point of 2 µN. This scan is done for two reasons. First, it will permit to verify the region that will be analyzed. It allows to see the topography and thus to check if the surface is cleaned without too many defects. The roughness can also be investigated since more accurate results are obtained with smooth surfaces. The mechanical properties measured are influenced by the roughness which in turn depends on the polishing procedure. A second polishing can be considered to improve this roughness. Example values for the RMSE roughness of bone and fused quartz obtained during tests performed on a window with a size of 5 µm on the side are given in the TABLE 2.1.

	RMSE Roughness
Fused quartz	1.2 nm
Bone	6 nm

Table 2.1: Mean values of the RMS roughness of fused quartz and bone obtained during several tests.

The second thing is the fact that the scan allows to stabilize the tip. Once the tip is engaged for this first scan, it must remain engaged until the end of the measurements to ensure reproducibility.

While it continues to scan, the modulus mapping parameters must be encoded. The scan rate and the set point are the first parameters to modify. The changes are immediately effective. The scan rate is decreased to improve the resolution. Then, the modulus mapping parameters can be entered. These are the frequency, the load amplitude, the constant lock-in time and the activation of the low pass filter. The modulus mapping with these parameters only starts when the start button is pressed. Modulus mapping is therefore performed in continuity with the scan.

Again, to give the system time to stabilize and settle the components (electronics...), the modulus mapping must run for several minutes to have time to scan a few lines. Once the system is stabilized, we must ensure that the amplitude of the tip ranges between 0.3 and 1. If it is not in this range, the set point and load amplitude can be changed which will have an impact on the amplitude of the tip. The higher the load amplitude, the higher the observed amplitude and vice versa. When all parameters are correct, a modulus mapping can be restarted from the bottom or the top of the scanned area. The measurement takes approximately one hour with a scan rate equals 0.1 Hz.
It is important to note that to perform a sensitivity analysis of the parameters, a full scan is not necessary. To save time, just a few lines are enough to observe the trend.

Once the data are acquired, a calibration of the tip radius is necessary to ensure the veracity of the storage modulus measurement. Indeed, as seen in the explanation of the EQUATIONS 1.14 and 1.15, to pass from the storage stiffness to the storage modulus, the tip radius of curvature intervenes. To determine it, fused quartz is used because its average complex modulus has a defined value of 69.6 GPa. The machine then uses this information to calculate the tip radius so that the complex modulus is equal to this value. To calculate the tip radius of a sample whose mean complex modulus is not known, the procedure is as follows [66]:

- Modulus mapping is performed on the unknown sample.
- An indent is performed on the unknown sample with a load function with a peak of 20 µN which gives a load-displacement curve. The peak is fixed at 20 µN because higher force is not necessary and this value is enough to see the displacement corresponding to the force used for the modulus mapping. By knowing the force used during the modulus mapping, the displacement corresponding to this force can be known.
- An indent is performed on the fused quartz. On the load-displacement curve accessed, it is possible to extract the force to be applied to obtain the same displacement as determined in the previous step in the unknown sample. Since the tip radius depends on the depth of penetration, it is important to determine the same depth in the fused quartz and in the unknown sample.
- Modulus mapping is performed on the fused quartz with the set point force determined at the previous point. This modulus can be stopped after a few lines to save time. The system is now capable of calculating the tip radius by knowing the value of the complex modulus of the fused quartz.
- This tip radius determined, it can be applied to the measurements made in the unknown sample which allows to correct them.

To save the data correctly for analysis, it must be saved in .txt format.

All these steps are resumed in FIGURE 2.13.

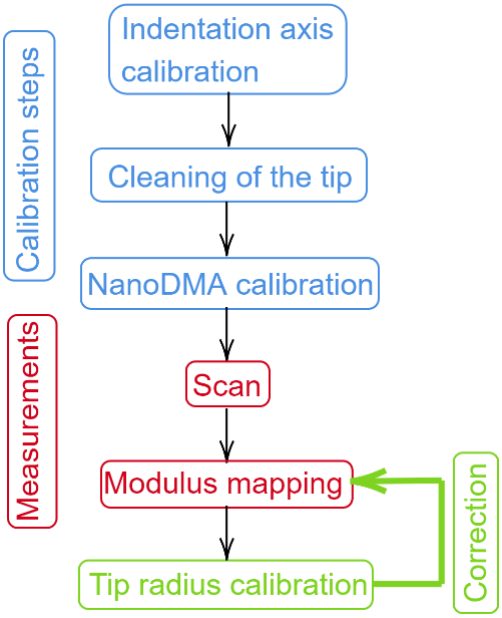

Figure 2.13: Resume of the different steps of the established protocol.

2.7 Statistical testings

In the following two sections (results and discussion), values are compared. To evaluate whether their difference is significant or not, a statistical analysis was then conducted. Since the two sets of data were independent, the two-sample t-test is used. To apply this test, two conditions must be met. The first is that each population must follow a normal distribution. A Kolmogorov-Smirnov test can be used to determine this. Second, the populations must have equal variances. This can be tested with a two-sample F-test. If at least one of the two conditions is not respected, another option must be used: Mann-Whitney U-test. This test also allows to determine if two sets of data are significantly different or not. The only difference is the null hypothesis which tests the probability that a random value in one set is greater or less than a random value in the second set. To achieve this, Matlab functions have been used. Statistical testings were conducted for the thickness and the storage modulus of the lamellae, for the storage modulus of the thick lamellae and the parallel fibers bone and finally for the parallel fibers bone and the central layer. A significance level equals 0.05 was used for this master thesis [73].

Chapter 3

Results

In this chapter, the different results obtained with the methods previously presented in the CHAPTER 1 are analyzed. Firstly, the results acquired with the SEM of the topography of the surface and its composition are investigated. Then those of the static indentations and those of the modulus mapping are explored to study the mechanical properties of a fibrolamellar unit. And finally, high load indents are analyzed qualitatively.
Before performing all these tests, the four samples were looked at under the optical microscope in order to check the quality of the polishing which, as seen before, must be of high quality to realize a modulus mapping.

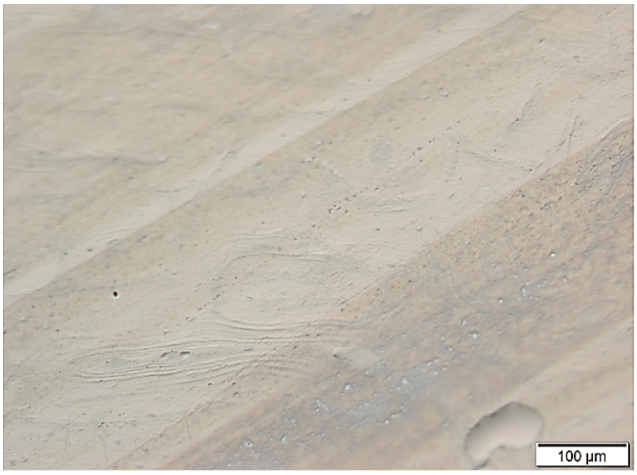

(a) Optical view of the sample number 1.

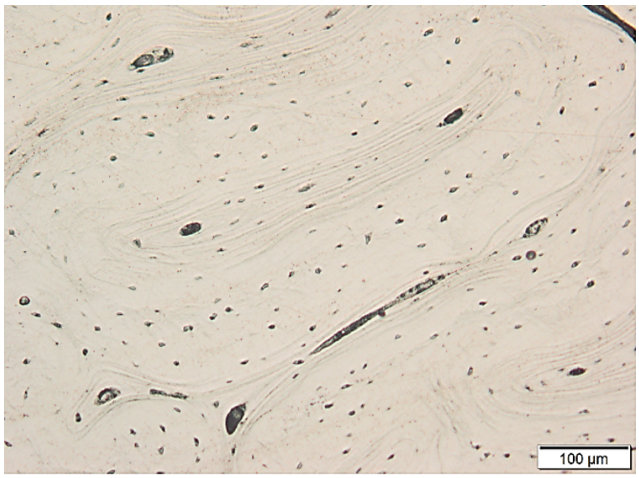

(b) Optical view of the sample number 2.

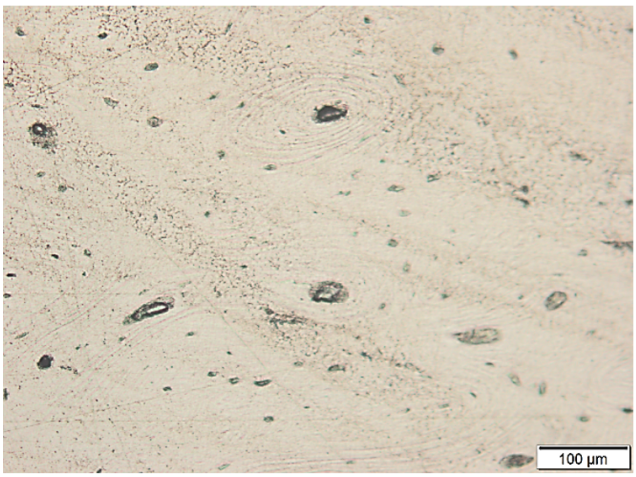

(c) Optical view of the sample number 3.

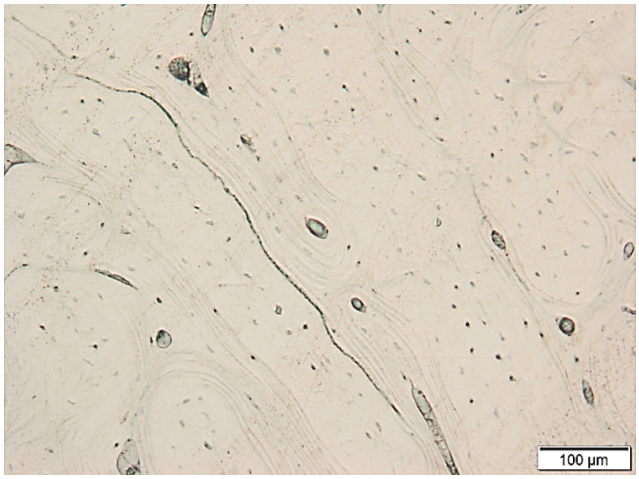

(d) Optical view of the sample number 4.

Figure 3.1: Optical view of the four samples with a zoom times 10.

These pictures (FIGURE 3.1), show that samples 1 and 3 have been badly polished because large black lines left by the process are visible. These two samples will not be used in order to guarantee the high quality of the measurements. Given the size of the units studied (about 140 µm) and the size of the sample (about 1.5 cm by 1 cm), only one sample is needed. The sample 2 was used throughout the measurements. In FIGURES 3.2 and 3.1b, the structure described in the SECTION 1 is present. Indeed, a network of blood vessels is visible, represented by the largest black holes with lamellar bone around them and the whole is attached by bone that looks uniform with a slightly different central layer. The osteocytes are also visible and are represented by the small black dots.

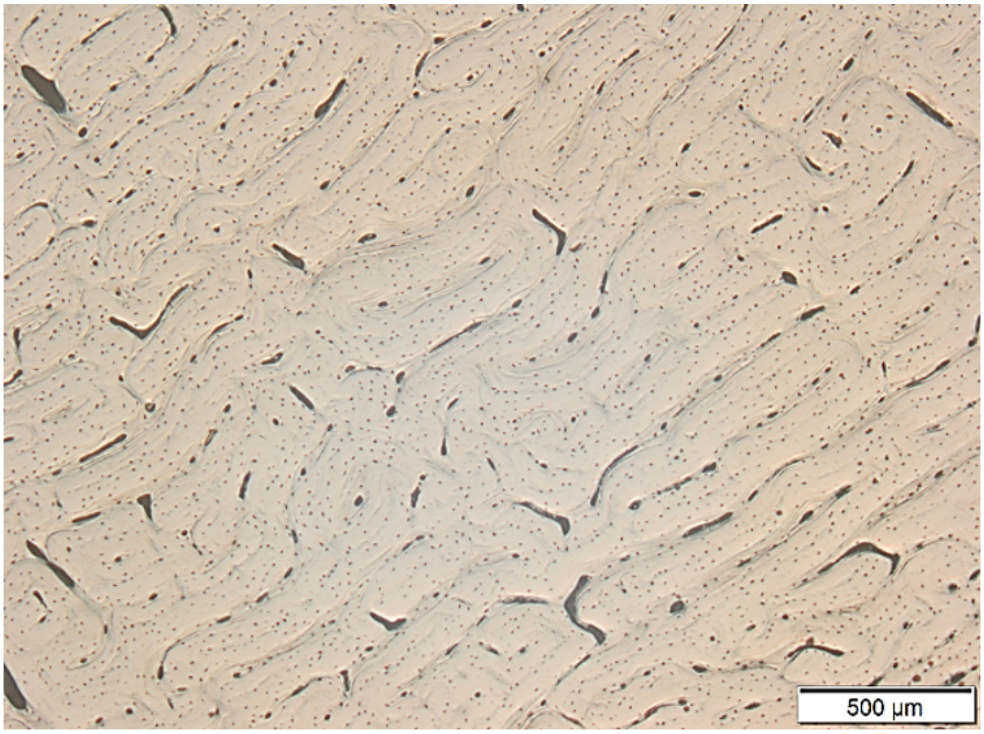

Figure 3.2: Optical image of the sample number 2 with a zoom times 2.5.

After this verification of the quality of the polishing and the choice of the sample to be studied, the measurements were started.

3.1 Electron microscopy

The goal of this part is to explore the features of a fibrolamellar bone unit and its composition and make the link with literature. As explained in SECTION 1.3, two different signals are analyzed using the SEM but the main part focuses on the BSE images.

3.1.1 Structure

First, a fibrolamellar bone unit can be observed by performing BSE images that provide compositional contrasts and allows to see features. In FIGURE 3.3, the different parts of a fibrolamellar bone unit are visible. Two blood vessels delimit the unit. They are then followed by lamellar bone (LB) that surrounds them.

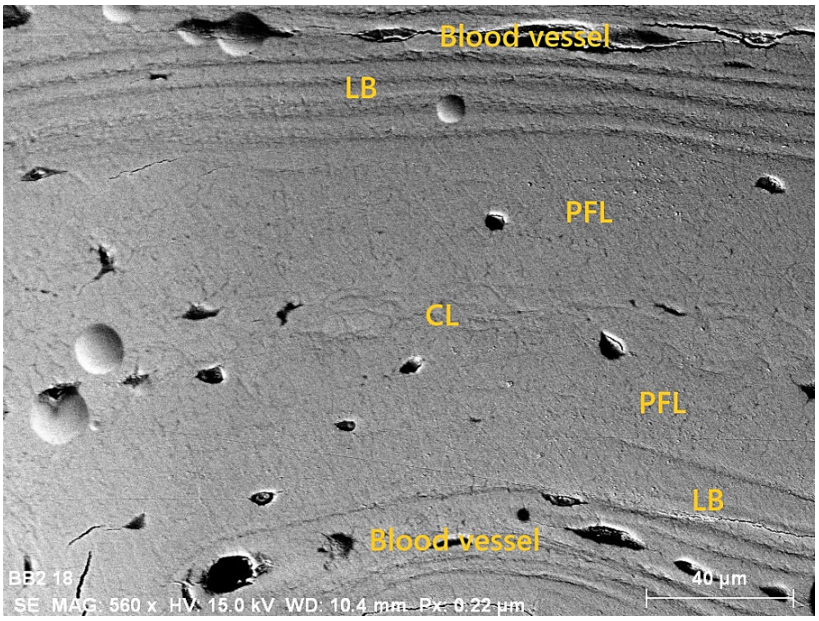

Figure 3.3: Image BSE of a fibrolamellar bone unit with its different features annotated.

Next comes what is assumed to be the parallel collagen fiber bone (PFL)[1] that sandwiches a central layer (CL). This central part is also described in the literature as a brighter layer than the other part as shown in FIGURE 1.16. In our case, this layer is not visible because of its compositional difference in this image but by the fact that there are lines that intersect in a random fashion. This structure confirms what is found in recent studies except that the middle line is not brighter. Higher resolution images were then taken to verify that no differences appeared between the regions or at their interface. After the verification of the zoom obtained, no dissimilarity is observed. From the FIGURE 3.3, the size of the different parts making up the unit of fibrolamellar bone can be estimated. The range of different values calculated from the scale is shown in TABLE 3.1.

Regions	Size [µm]
White lamellae	2.79 - 4.65
Black lamellae	1.39 - 2.6
Central layer	11.6 - 13.95
Parallel fibers	39 - 41

Table 3.1: Size range of the different zones composing a fibrolamellar bone unit.

The lamellae that appear white and black have differences in size: the white are thicker than the black with a significant difference ($p<0.05$). They are therefore called thick lamellae and the black ones are called thin lamellae. The entirety of a fibrolamellar bone unit, from one blood vessel to the next parallel to it, can also be measured. One unit ranges from 133 to 146 µm. It is important to note that these are ranges of values obtained from the BSE images acquired with the microscope, which represent only a few regions. Values outside these ranges can be found for other fibrolamellar bone units but still close to the ones presented here and therefore give a good idea of sizes and proportions.

To try to highlight the orientation of collagen fibers, an etching [2] was performed. It aims at dissolving a part of the minerals and leaving only the collagen. Once this treatment was done, the sample was again looked at with SEM. The image obtained is visible in FIGURE 3.4. On this one, the lamellae and

[1] We are not sure if the collagen fibers are parallel because we have not observed it, but we will call it that (corresponds to the literature) in the following work.

[2] This method was actually done last since it damages the surface by removing some of the minerals.

the osteocytes are highlighted. The osteocytes appear aligned with respect to the lamellae. In addition, a central area between two blood vessels appears to show a denser line of osteocytes that are still well aligned. Unfortunately, the orientation of the collagen fibers is not visible.

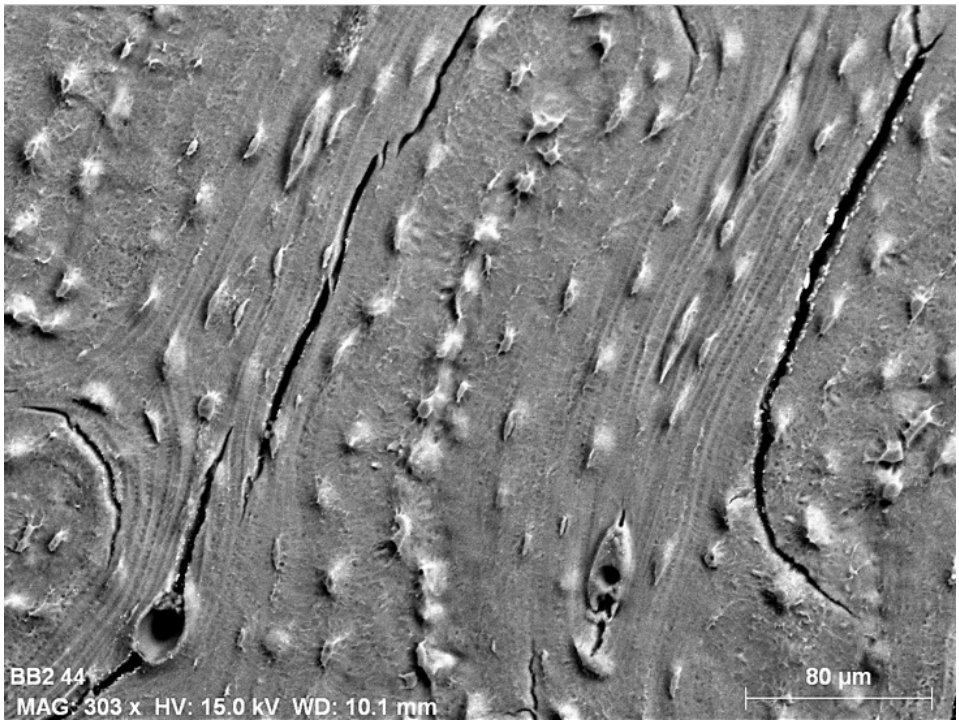

Figure 3.4: SEM image of a fibrolamellar bone unit after etching has been performed on the sample.

3.1.2 Composition

Since different features are visible in BSE images, the composition is investigated to see the difference of constitution in all regions. Several chemical composition tests were performed. A first image was done by making a map of a fibrolamellar bone unit. The second one consists of a profile that also crosses a fibrolamellar bone unit. The region used to make the composition map is visible at FIGURE 3.5. The same features as those seen in FIGURE 3.3 are observable.

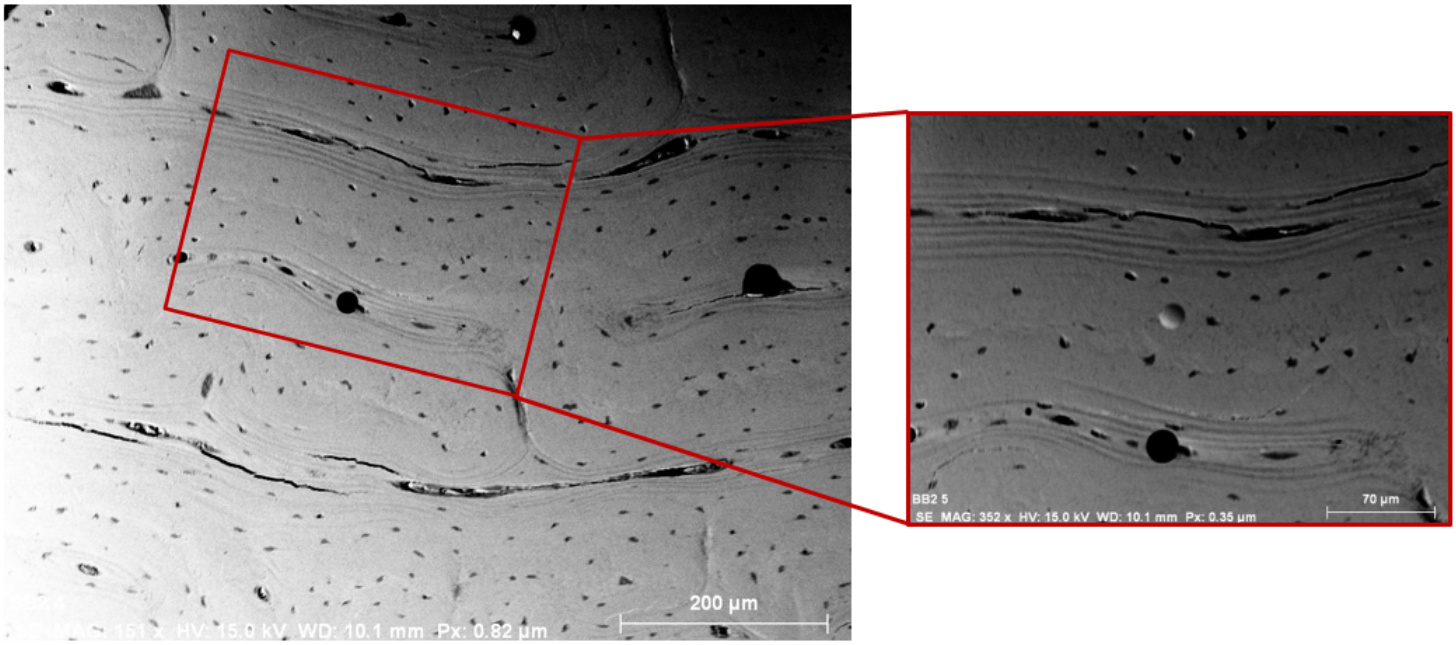

Figure 3.5: BSE image of fibrolamellar bone with a zoom of a fibrolamellar bone unit.

Results for composition in calcium, carbon, magnesium, phosphorous, oxygen and sodium (sets of components present in the bones) are visible in FIGURE 3.7. It can be seen that the composition appears to be homogeneous in the fibrolamellar bone unit for all components. Indeed, the only features that differ in composition are in images of Ca, C, O and P and they represent the holes in the bone such as blood vessels and osteocytes that are filled with resin and therefore clearly have a difference in composition from the bone.

The results of the profile (visible in FIGURE 3.6) can also be analyzed. They are shown in FIGURE 3.8. The observations are the same as those made for the map: the structure seems quite homogeneous. At the level of the central line, no increase in calcium concentration is observed. This is contradictory to the literature. This point will then be discussed in SECTION 4.

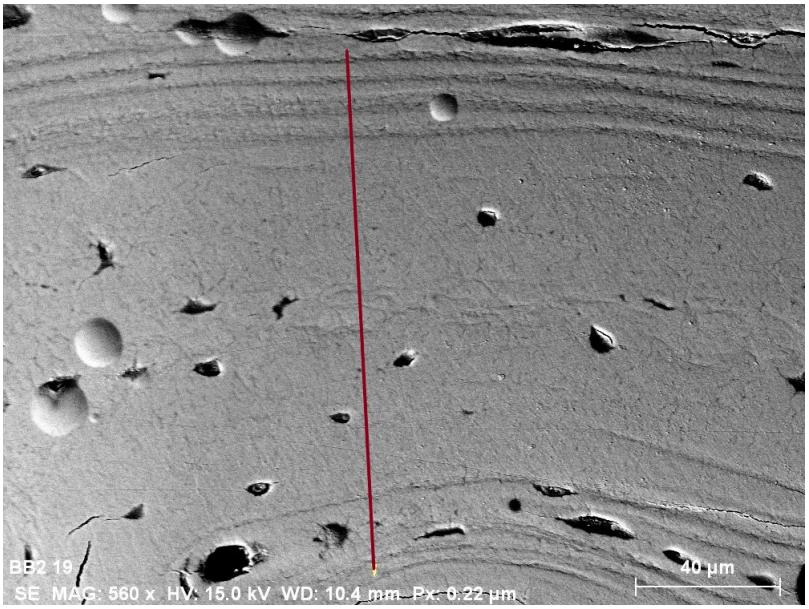

Figure 3.6: Line crossing from top to bottom a fibrolamellar bone unit used to study the possible changes of composition between the different features.

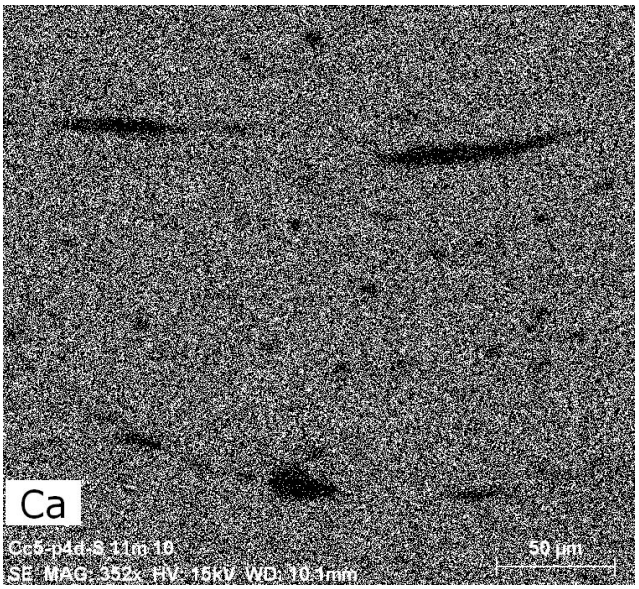

(a) Distribution of calcium.

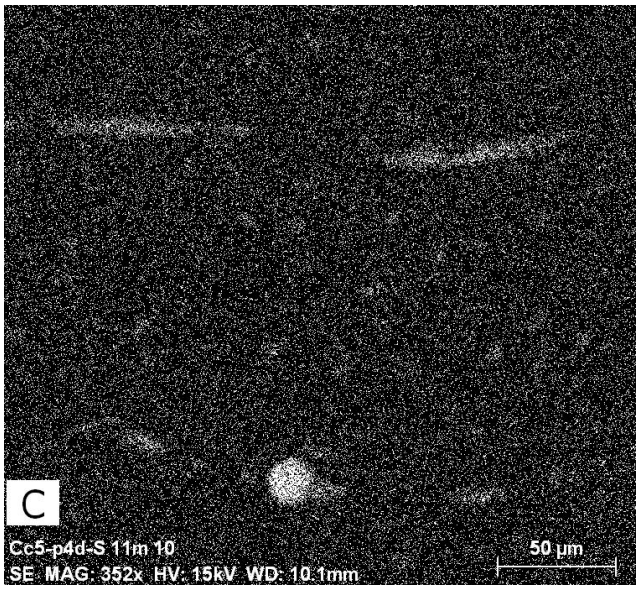

(b) Distribution of carbon.

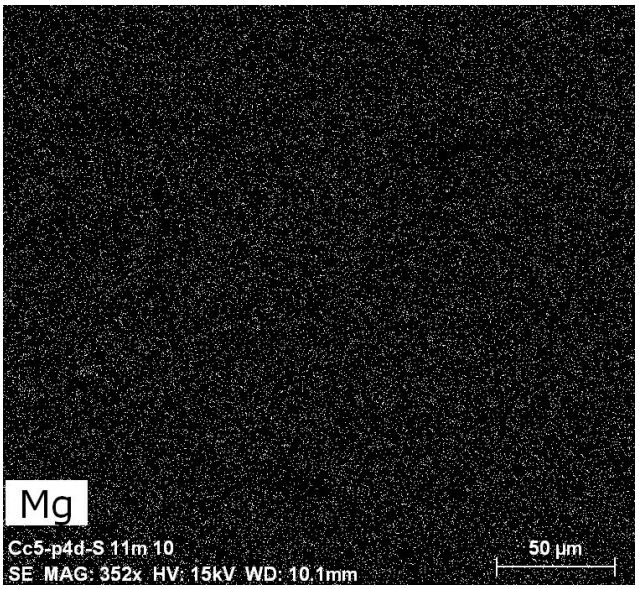

(c) Distribution of magnesium.

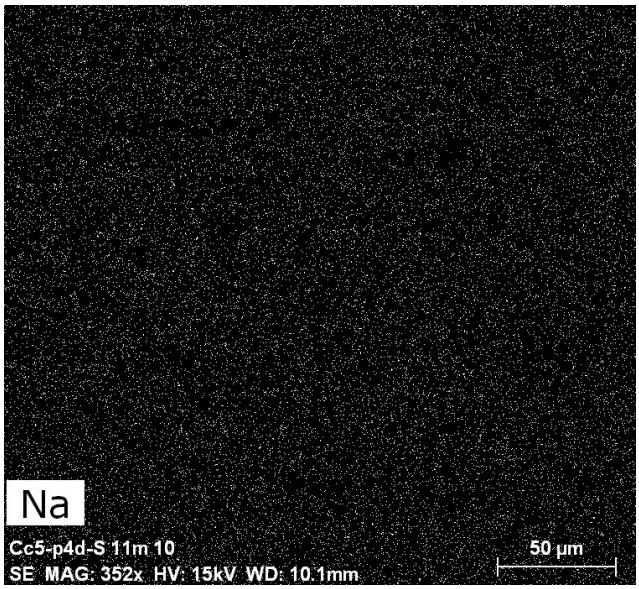

(d) Distribution of sodium.

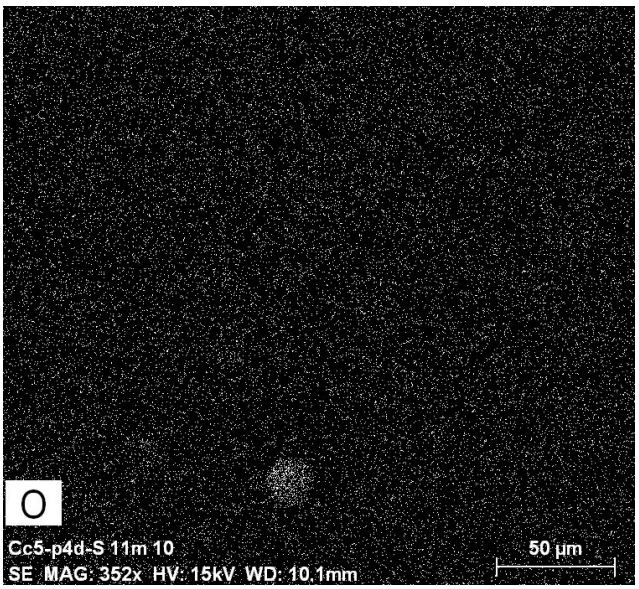

(e) Distribution of oxygen.

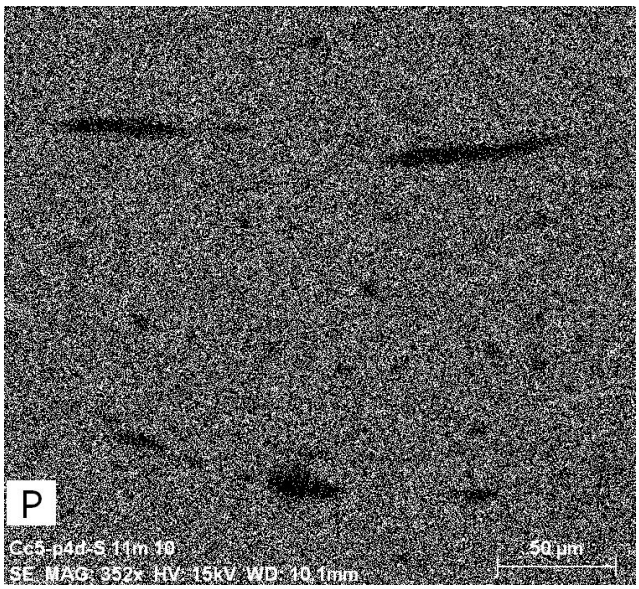

(f) Distribution of phosphor.

Figure 3.7: Distribution of different components in a fibrolamellar unit.

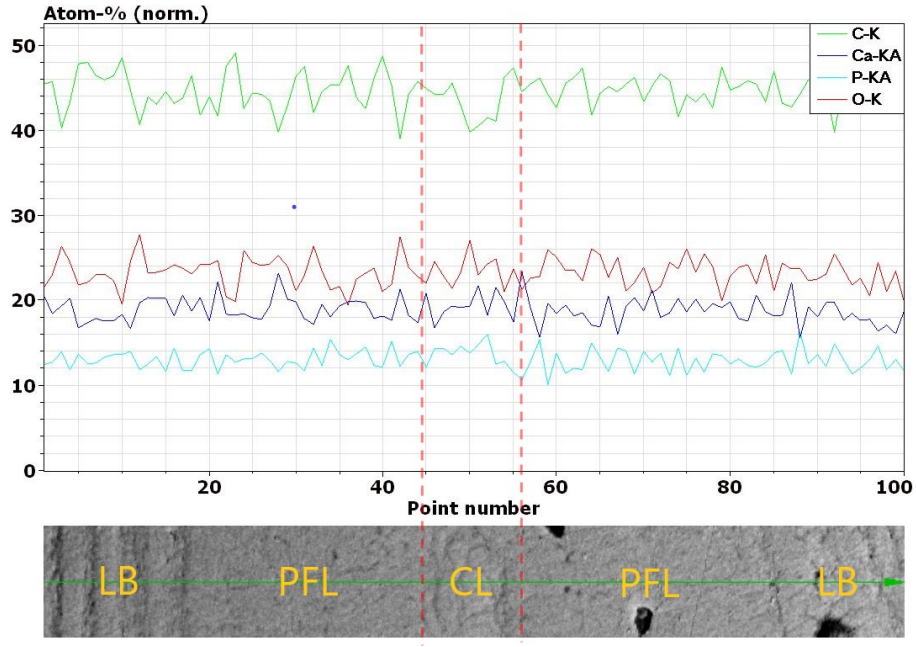

Figure 3.8: Profile in atomic percentage of the composition of a fibrolamellar bone unit.

A last kind of information can be obtained with SEM: these are SE images that allow to see the topography. A SE image is visible in FIGURE 3.9. When we compare this image with the BSE image shown in FIGURE 3.5, we notice that the images are almost identical, the same features are presented.

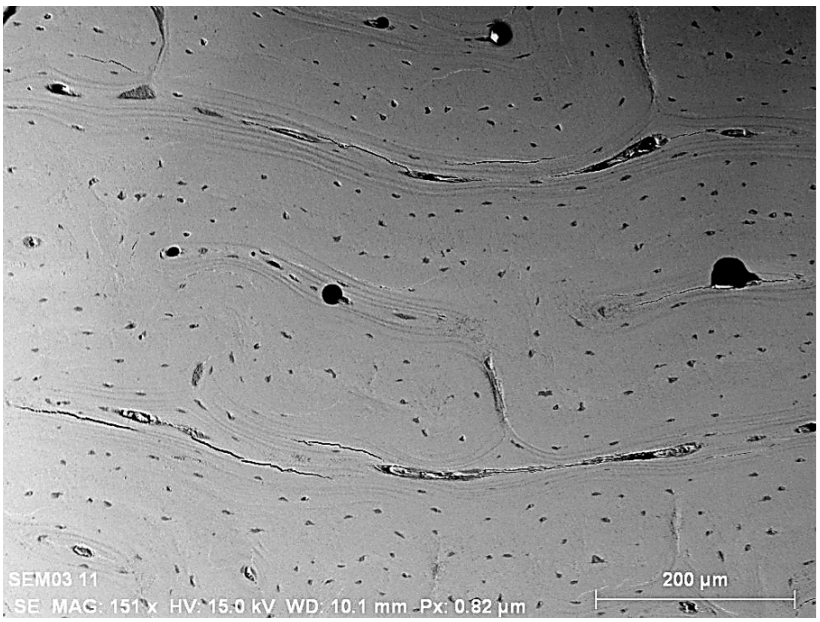

Figure 3.9: SE image of fibrolamellar bone.

3.2 Nanoindentation

In this section, the mechanical properties of a fibrolamellar bone unit are studied. For this purpose, 150 static indentations were made on a 5×30 indentations grid that covers a fibrolamellar bone unit from top to bottom. They are separated by 6 µm each to ensure that the plastic deformations generated by an indent do not disturb the area of the following indent. The resulting grid is shown in FIGURE 3.10 where the little black points represent the indents.

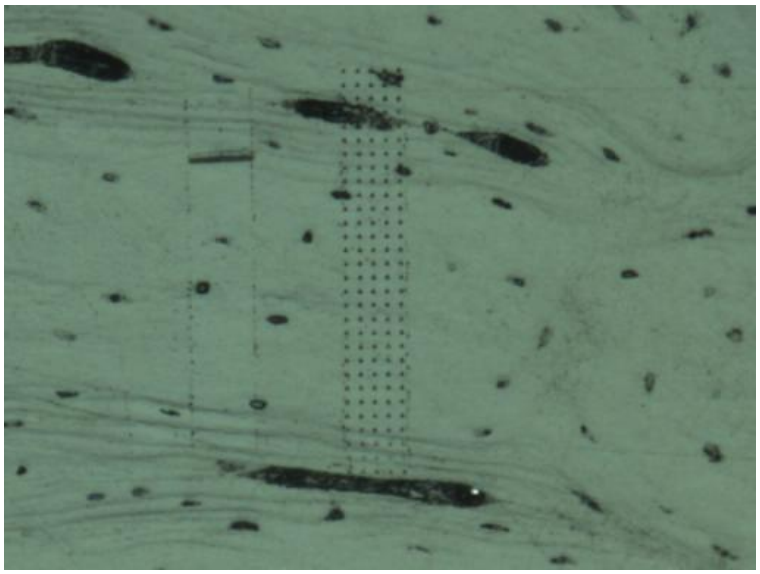

Figure 3.10: Image of the static indentation grid obtained with the nanoindenter optical microscope.

Each indent was obtained by applying the load function presented on the left in FIGURE 3.11. The load starts at zero and increases linearly during the first 20 seconds to reach a load of 3000 µN. Then, for the next 20 seconds, this load is constantly held at 3000 µN and, for the last 20 seconds is decreased linearly back to zero.

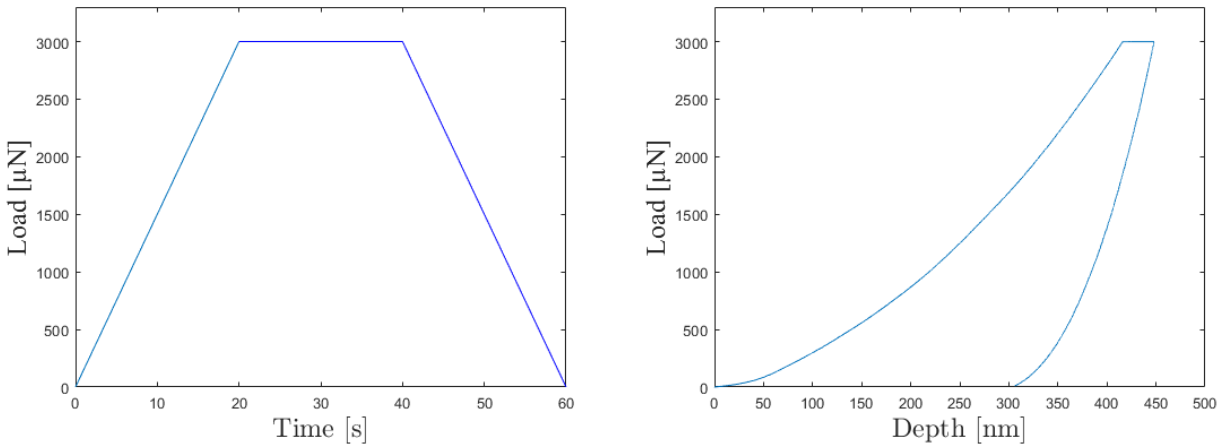

Figure 3.11: From left to right: trapezoidal load function used to perform each indent and load-depth curve obtained for a typical static indent.

At each indent, a load-depth curve is obtained, as shown on the right in FIGURE 3.11. The first part corresponds to the loading with depth which increases with the load. Then, when the load is kept constant, a plateau is observed on this curve where the load remains constant but the depth continues to increase due to viscoelastic/plastic deformations. And finally, the last part of the curve represents the unloading, part during which the depth decreases because the tip is removed. The curve does not return to its initial position which proves that there is a hysteresis phenomenon present, irreversible deformations have occurred and the material does not return to its initial state. Thanks to these curves, a Young's modulus could be calculated for each point as explained in SUBSECTION 1.2.1 by measuring the slope of the line at the very beginning of the loading curve which gives the stiffness. Note that the value obtained is actually the reduced modulus, as explained in SECTION 1 to EQUATION 1.17. However, the Young's modulus of the tip being very high, the second term divided by a much larger value can be neglected and the value we get is therefore very close to the Young's modulus of the element under

study. The hardness can also be obtained but the same trend as the Young's modulus was observed. It was then decided to study only the latter since the hardness did not bring new information.

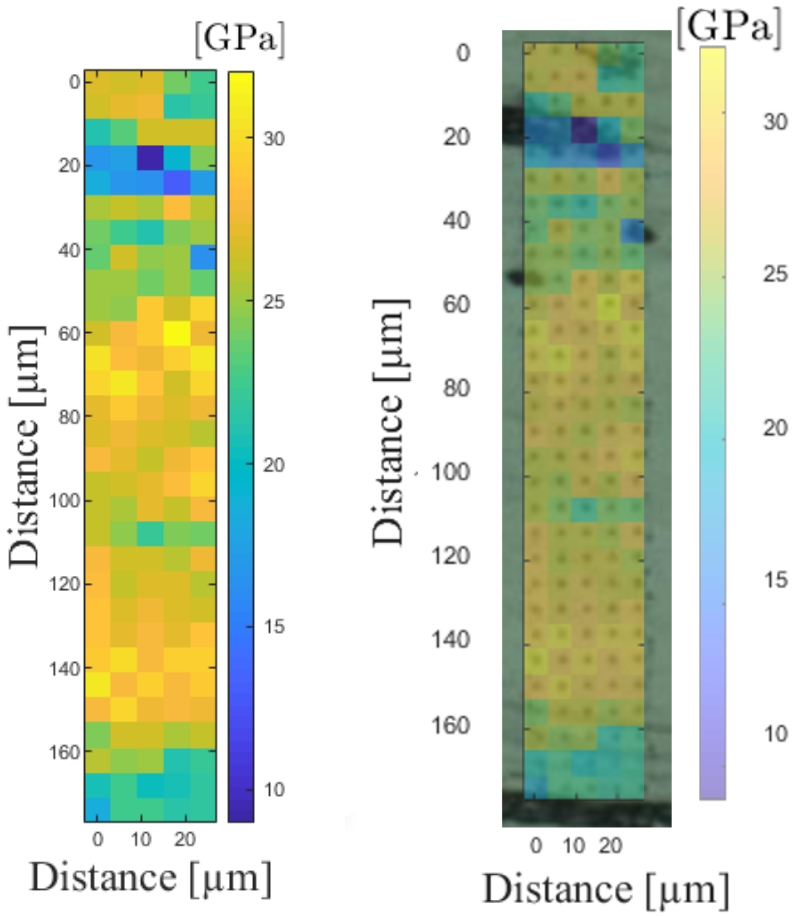

Figure 3.12: From left to right: value of the Young's modulus obtained for each static indentation and superposition of these values and all static indents.

The value of the Young's modulus for each indent is shown in FIGURE 3.12. The image of the left was also superimposed on the image of the indents to be able to correlate the value of a point to what it corresponds. When analyzing these images, several observations stand out. First, the middle line which is approximately between 100 and 110 µm in the image, assumed to be the hypercalcified layer mentioned in the literature, appears to have a lower Young's modulus than the bone containing parallel collagen fibers with values between 20 and 25 GPa compared to values between 26 and 33 GPa. These last values are the highest. In the lamellar part of the bone, the lamellae are not distinguishable. The resin-filled part of the blood vessel has much lower Young's modulus values than the other parts, which is logical since the resin is relatively soft. In this image, it is also visible that the structure presents the symmetry of mechanical properties at the level of the central layer.

The profiles of the Young's modulus of each line of indents that connect one blood vessel to another can also be analyzed. They have been represented in FIGURE 3.13. For this analysis, the value of the points of the two osteocytes that are filled with resin were excluded and replaced by an average of dots that surround it and are part of the same structure. For example, the point on the left, which is about 50 µm from the top, has been replaced by an average of three points, the one to the right of it, the one just below it and the one diagonally down. The two top points belonging to a lamella are not taken into account, being part of another structure. The resin filled dots belonging to the blood vessel were kept.

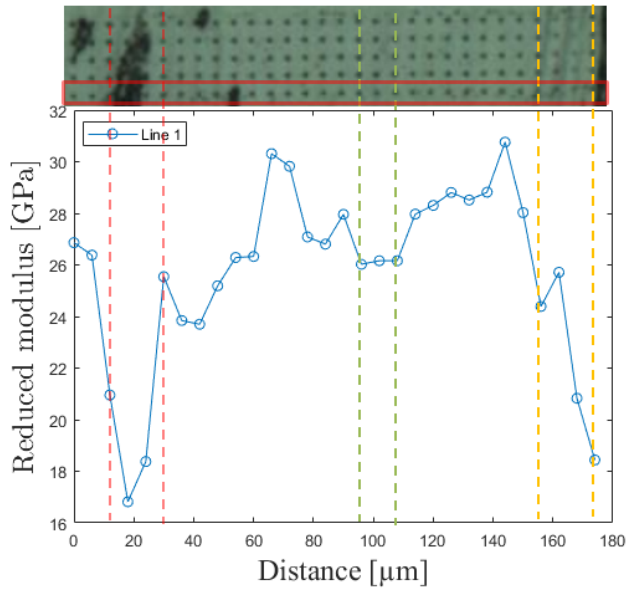

(a) Profile of the Reduced modulus of the line 1.

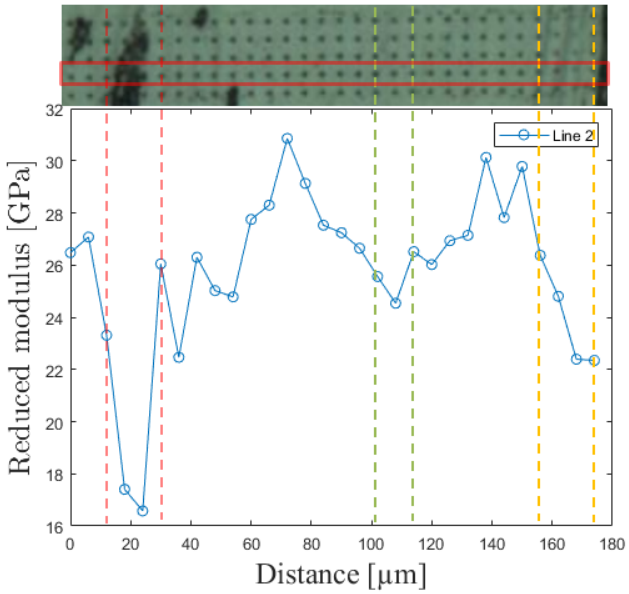

(b) Profile of the Reduced modulus of the line 2.

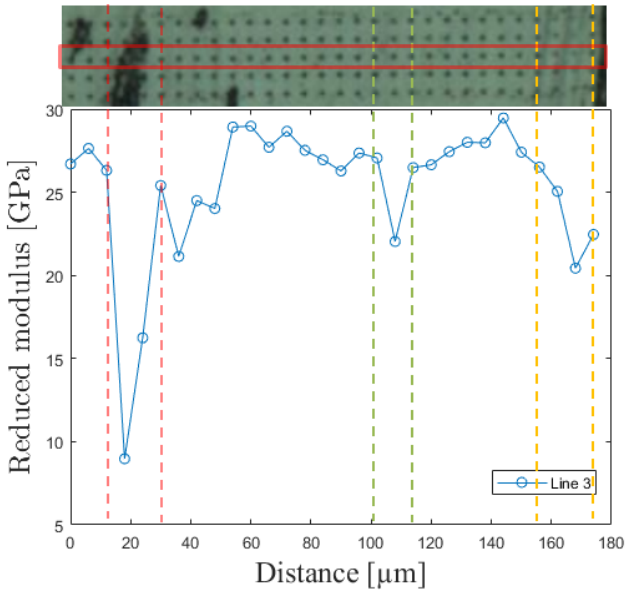

(c) Profile of the Reduced modulus of the line 3.

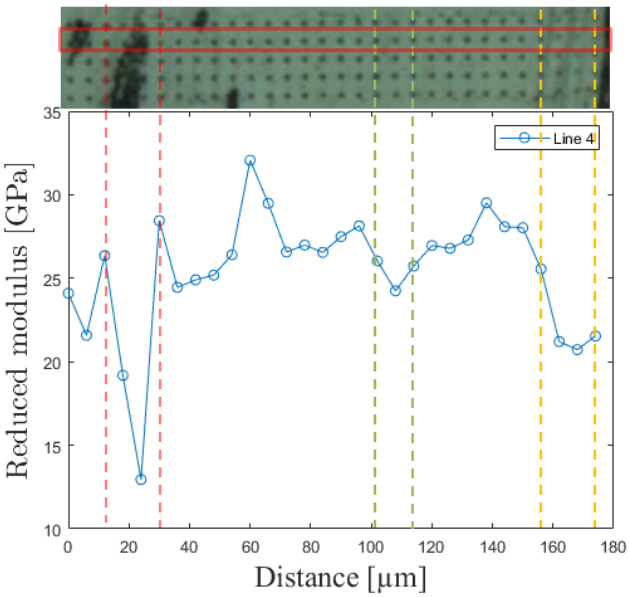

(d) Profile of the Reduced modulus of the line 4.

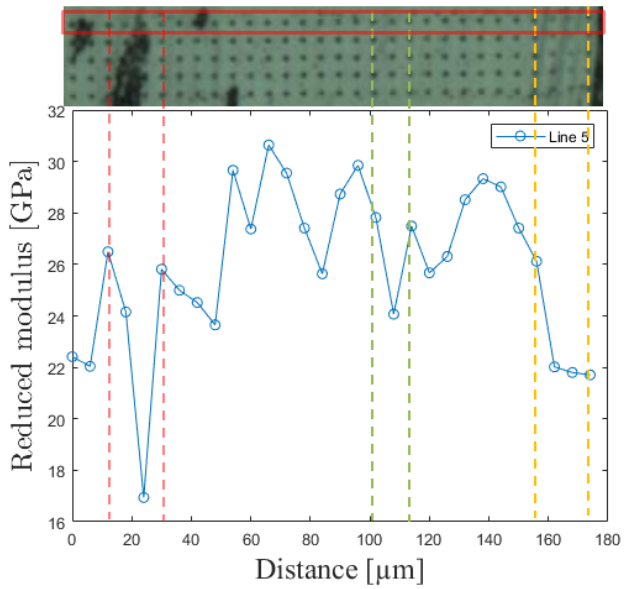

(e) Profile of the Reduced modulus of the line 5.

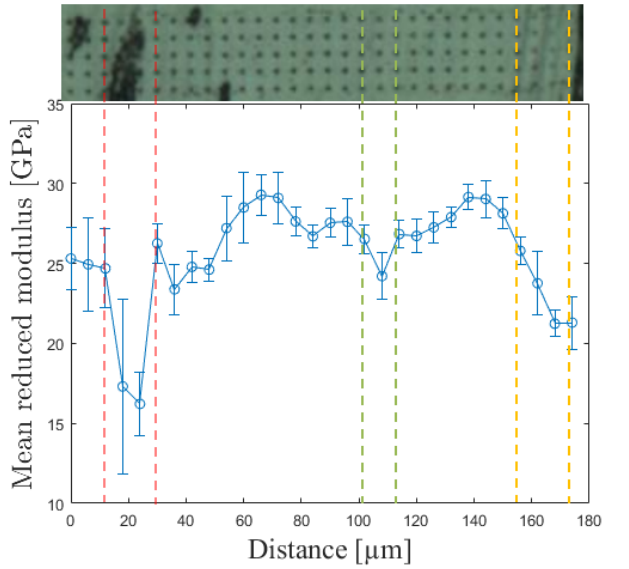

(f) Profile of the mean value of the Reduced modulus of the 5 lines and the corresponding standard deviation.

Figure 3.13: Profile of the Reduced modulus for each line and the mean of these lines.

When analyzing these profiles, a similar trend is observed. The blood vessel region (delimited by two dashed red lines on the graphs) is represented by a large downward peak which is consistent with the fact that it is filled with a softer resin. The middle part (delimited by two dashed green lines on the graphs) also presents a downward peak but this peak drops less with a higher average value for the Young's modulus equal to 24.2 ± 1.26 GPa. The surrounding parts, which are thought to be composed of parallel collagen fibers (first part between the red zone and the green zone and second part between the green zone and the yellow zone), are represented by bumps and have the highest mean Young's modulus of 29.29 ± 1.47 GPa. The lamellar bone is the latest feature. One of the areas made up of this type of bone is shown by the yellow dotted lines on the right of the image. Looking at this, no difference between the lamellae is visible. The profile just seems to decrease from the parallel fibers bone to the blood vessel.

When mapping the Young's modulus and plotting profiles, the same observation can be made: the lamellae are not visible, one can only notice that these regions have a lower Young's modulus than the regions where the collagen fibers are parallel. In order to improve that, modulus mapping was used.

3.3 Modulus mapping

3.3.1 Calibration of the implemented protocol on bone samples

The protocol being established on fused quartz in SECTION 2.4 can be applied to bone. Before performing the real measurement, several steps need to be investigated on bone.

First, reproducibility was tested to verify that the protocol worked properly on this type of sample. These tests were performed in a region as flat as possible as shown in FIGURE 3.14. A flat region was chosen so that the results would not be influenced by the topography of the sample.

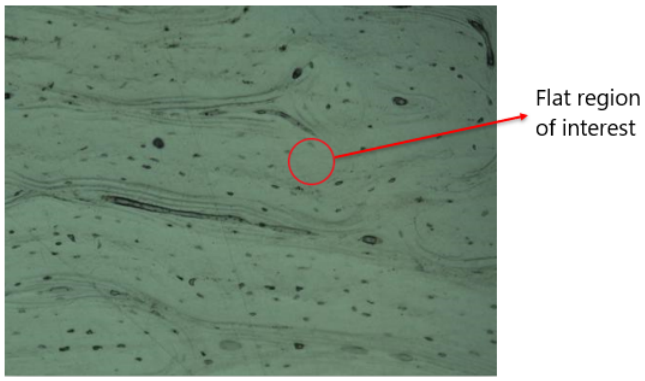

Figure 3.14: Optical microscopy image of a region of sample number 2.

Three tests were done on this same flat region and with the same parameters following the protocol established on fused quartz. The parameters were the following:

- Scan rate = 0.1 Hz
- Scan size = 5 µm
- Set point = 4 µN
- Frequency = 200 Hz
- Load amplitude = 2 µN
- Lock-in time constant = $6 \cdot 10^{-3}$ sec
- Filter ON

The results obtained on the bone are as follows:

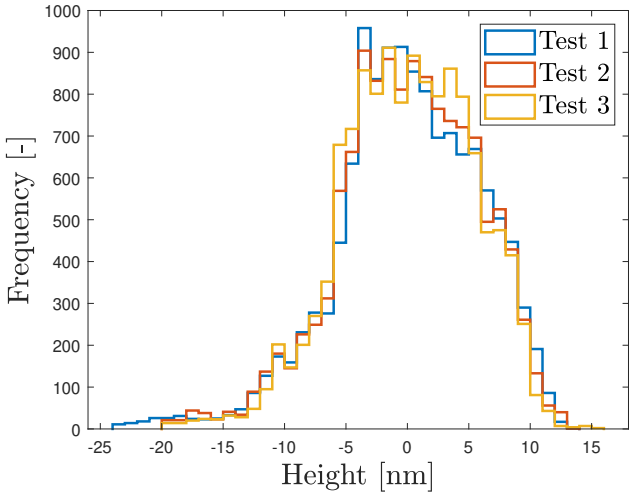

(a) Frequency distribution of the height [nm] for four same tests.

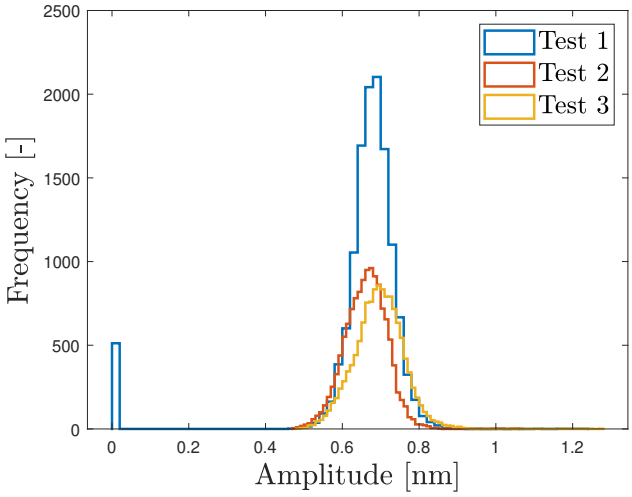

(b) Frequency distribution of the amplitude [nm] for four same tests.

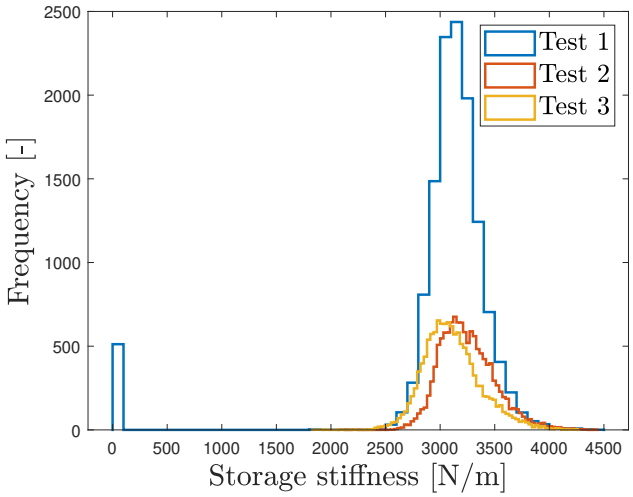

(c) Frequency distribution of the storage stiffness [N/m] for four same tests.

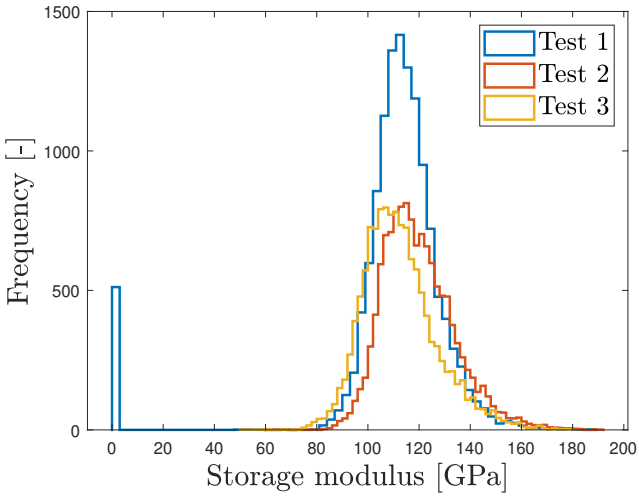

(d) Frequency distribution of the storage modulus [GPa] for four same tests.

Figure 3.15: Results obtained for three tests performed on the sample number 2: Frequency distribution of the height, the amplitude, the storage stiffness and the storage modulus.

With these new results we can say that the protocol established works well since results are reproducible. The only disadvantage visible on these graphs is the fact that the values for the storage modulus are again too high compared to the expected values (the values obtained are around 110 GPa whereas the expected values should be 20-30 GPa). To fix this, other parameters must be changed.

After that, the influence of the frequency was investigated. To do that several tests were performed at the same place with the same parameters with only the frequency changing. Frequencies 140, 170, 200, 230, 260 and 290 Hz were tested.
During these tests, the modulus mapping was stopped after about 15 minutes to save time. Indeed, the influence of the frequency was already visible in the part that had been run. Consequently, for the analysis, only the upper part of the images was taken into account. These results are shown in APPENDIX A. Several results emerged from these tests. First, the Belgian network is supplied by an alternating current with a frequency of 50 Hz [74]. In order to avoid any interference between this frequency and the one measured, multiples of the network frequency must be avoided. The default frequency of 200 Hz is therefore changed. Secondly, after observing the images of the storage stiffness obtained, it was noticed that the low frequencies decreased the sharpness of the image (noisier) while the higher frequencies

increased it (less noisy). The frequency of 290 Hz did not bring more sharpness than that of 260, the latter was thus retained as a choice of frequency.

After these measurements were made, the sample was again observed under the optical microscope. The window did during the modulus mapping was then visible because traces on the sides appeared as shown in FIGURE 3.16.

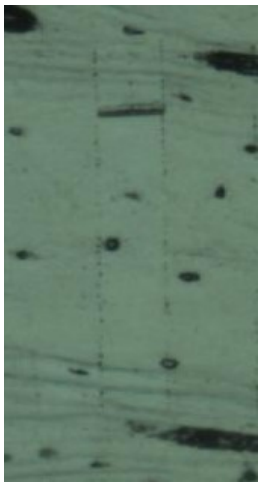

Figure 3.16: Optical microscopy image of a damage region of the sample number 2.

This is a problem since the modulus mapping is not supposed to change or damage the surface. It was then concluded that the set point equal to 4 µN and the load amplitude of 2 µN were too high. This resulted in too deep penetration into the bone and causing plastic deformation. The solution was then to decrease these two forces. After this discovery, many tests were performed again with smaller forces in order to obtain consistent results. This means that the modulus mapping does not damage the sample anymore and that the values obtained for the storage modulus are correct. These objectives were met for a set point equals 1 µN and a load amplitude of 0.35 µN. With these parameters, modulus mapping was performed in three different test regions: a relatively flat region, a region with lamellae and a region between the two called interface. The results obtained are shown in FIGURE 3.17.

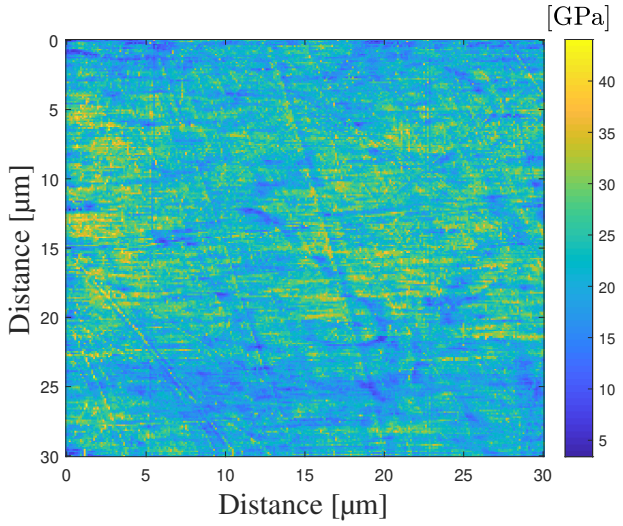

(a) Storage modulus image [GPa] of a flat region.

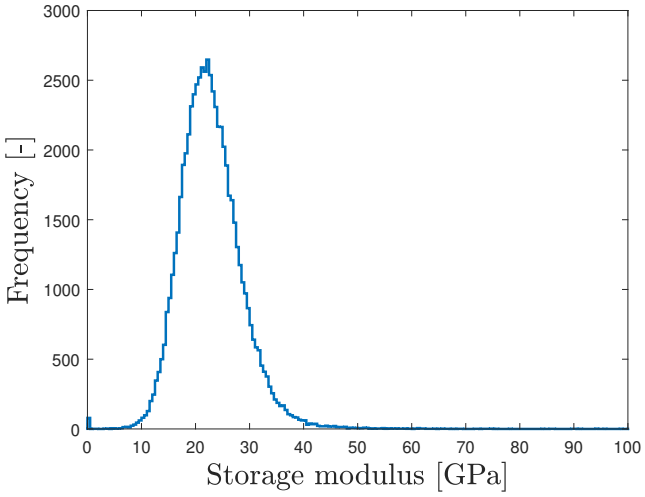

(b) Storage modulus histogram [GPa] of a flat region.

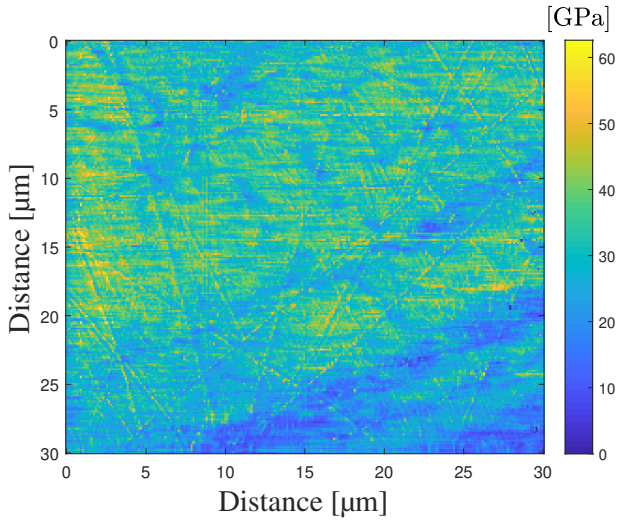

(c) Storage modulus image [GPa] of an interface region.

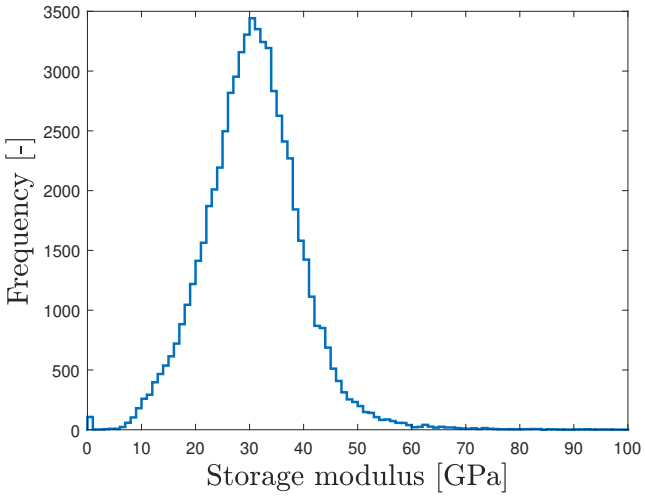

(d) Storage modulus histogram [GPa] of an interface region.

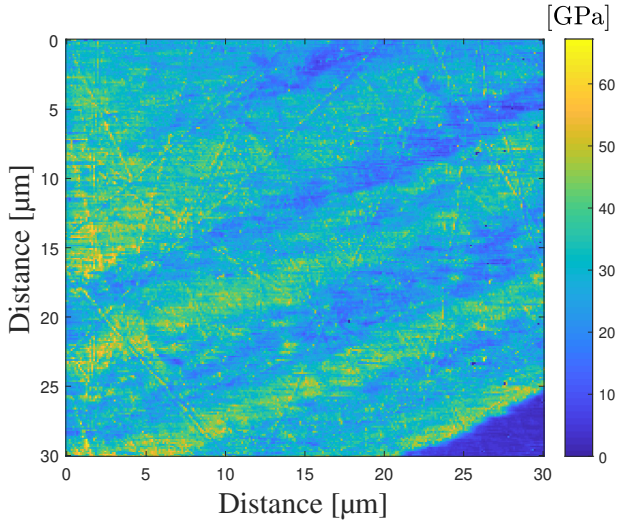

(e) Storage modulus image [GPa] of a lamellar region.

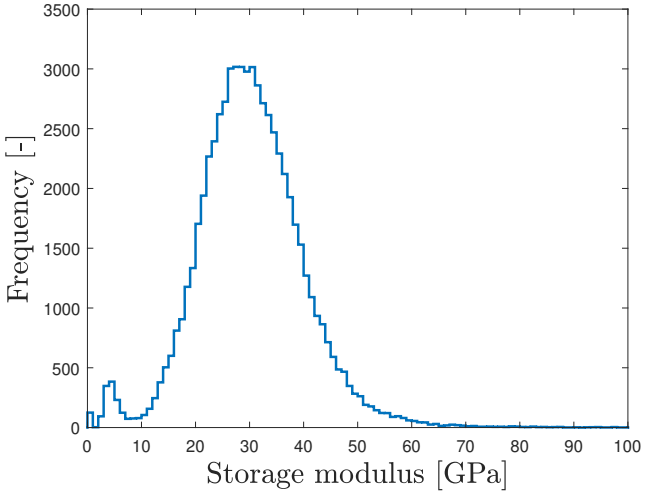

(f) Storage modulus histogram [GPa] of a lamellar region.

Figure 3.17: Results of storage modulus in GPa obtained for tests performed on three different region: flat, interface and lamellar.

Firstly, these results show us that, thanks to the established protocol, the images are not too noisy. The flat region is quite homogeneous as expected while in the lamellar region the different lamellae

are clearly distinguishable. The fact that this feature is visible means that the lamellae have different mechanical properties. As explained in SECTION 1, lamellae alternate between stiff and soft. Secondly, the histograms show that the average storage modulus is around 30 GPa which is consistent with the values described in the literature.
After these measurements, the learning of the use of the modulus mapping on bone is completed. We then moved on to real measurements on an area of interest of fibrolamellar bone.

3.3.2 Modulus mapping on a complete fibrolamellar bone unit

The modulus mapping method was applied to map each area of a fibrolamellar bone unit and to study its mechanical properties. This unit was covered by performing 6 scans of 30 µm each with an overlap of 2 µm in order to guarantee continuity of the measurements. For this purpose, the protocol established in the SECTION 2.6 was implemented. In addition, between each scan, the tip was kept engaged to ensure agreement between measurements. During these scans, a set point of 1 µN was applied and a load amplitude of 0.35 µN for the first scan and 0.65 µN for the next five was used. The load amplitude was increased to keep the amplitude in the range of 0.3 - 1 nm, as required by the technique. The region studied is the area shown in FIGURE 3.18. It corresponds to the one used to realize the indent grid. The modulus mapping was therefore carried out first. Having as advantages to leave the surface intact, the indent grid could then be performed exactly in the same area which guarantees the comparability of the results.

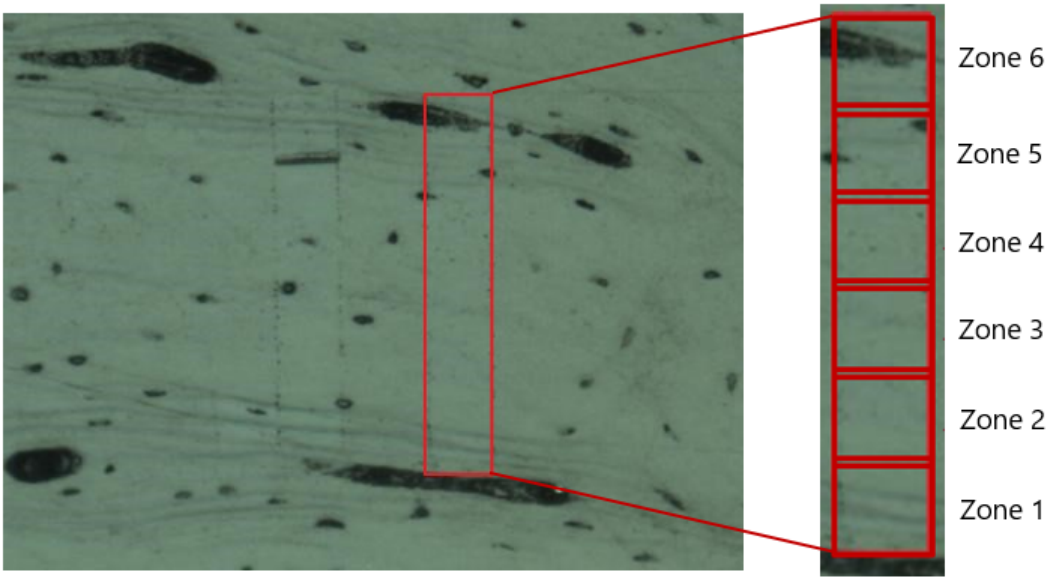

Figure 3.18: Region of interest on which 6 windows of 30 µm of modulus mapping have been performed.

Each scan of regions of interest is analyzed to extract information. Several types of information were examined and for this purpose, particular Matlab functions were used.

Firstly, the images, before being observed, are processed to remove all outliers that could distort the data and therefore the analysis. To do this, the function FILLOUTLIERS of Matlab was used with the argument "nearest" which means that each detected outlier is replaced by the neighboring pixel which is not an outlier. A value is considered as an outlier when its value exceeds three median absolute deviations (MAD) from the median with the MAD being defined as:

$$MAD = \text{median}(|A_i - \text{median}(A)|)$$

where A represents the matrix of the data, A_i is the element i of this matrix and i is equal to the number of data present in it [75].

Secondly, the profiles of the storage modulus averages are filtered to remove possible noise and highlight the trend of the curve by smoothing it. To do this, the function FILTER of Matlab was used to apply a moving-average filter. This consists of a window, whose size is to be determined, in which the average of the values is made [76]. The window then moves to process each point and thus smooth the data. The choice of the window size was made by trial and error, making sure that noise was eliminated but that no information was lost.

Finally, the correlation between the storage modulus and the height is analyzed. It is analyzed to determine whether the data are influenced by topography or not. If the correlation is zero, it means that the measurements have not been influenced by polishing, that they are true and that no artifact biases the data. To do that, the function CROSSCORR of Matlab is used. This function allows to quantify the similarity between two data sets. The lag permits to look at the correspondence between a set and a shifted version of the other set. The lag was chosen equal to $\pm$ 5 values which make a lag of about 0.6 µm. Since the measurements were made at the same location without disengaging the tip which guarantees that the measurements were made in the same region, a higher lag is not necessary. The coefficient returned for each lag indicates the correlation rate. If it is close to 0, there is almost no correlation, if it is close to 0.5 or -0.5, it is strong and if it is close to 1 or -1 the correlation is very strong. 1 means that the two data sets tested are identical [77].

► Zone 5: lamellar bone

The first zone investigated was zone 5, which corresponds to a region of lamellar bone. The height and storage modulus obtained for this area are shown in FIGURE 3.19.

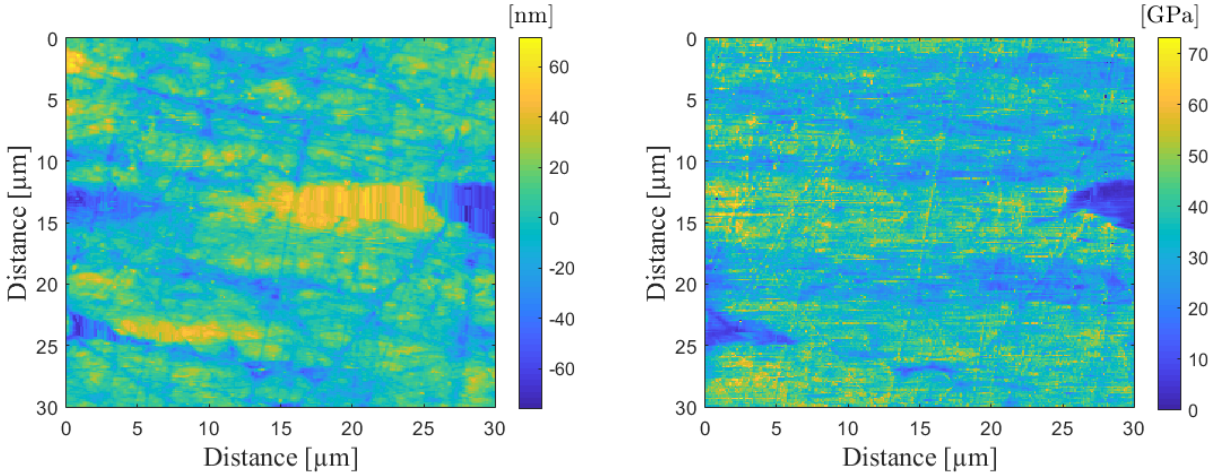

Figure 3.19: From left to right: map of the height in nm and map of the storage modulus in GPa, both for the region 5.

From these images, several things can be retained. First, we notice that the lamellae are weakly displayed on the image of the height and an artifact is apparent due to the resin. They are also present in a more visible way in the image of the storage modulus. The different lamellae that we have characterized in the results obtained with the scanning electron microscope show dissimilar mechanical properties. The thick lamellae, being of a more yellow color, present a higher storage modulus than the thin lamellae which appear more blue. To verify this, a profile was made perpendicular to the lamellae. A line with a thickness of 25 pixels (2.3 µm) was drawn and averaged over its width. Then the data was filtered as

explained before with the function FILTER to remove the noise and better show the trend. The results are visible in FIGURE 3.20.

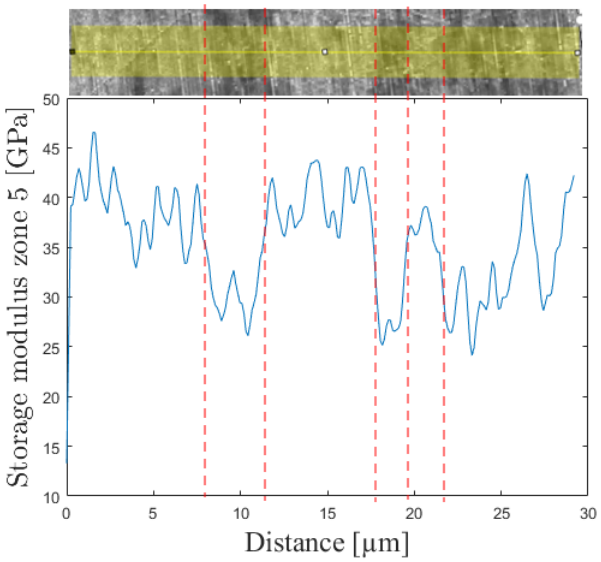

Figure 3.20: Profile of the storage modulus [GPa] crossing perpendicularly a lamellae zone of the sample.

The trend is the same as seen for the whole image: the thin lamellae have a lower storage modulus than the thick lamellae. The storage modulus of the different lamellae was then quantified. For this, several data sets were taken in the different areas of interest and the mean and standard deviation were calculated. After a statistical test, their difference was determined to be significant ($p<0.05$). The values obtained are visible in the TABLE 3.2.

	Storage modulus [GPa]
Thick lamellae	46.46 ± 3.56
Thin lamellae	32.8 ± 4.17

Table 3.2: Average and standard deviation of storage modulus for thick and thin lamellae.

The correlation between height and storage modulus can also be investigated. Using the Matlab function described above, the graph in FIGURE 3.21 is obtained. For a lag equals 0, the coefficient is equals to 0.5 approximately. This means that the correlation is strong between the height and the storage modulus.

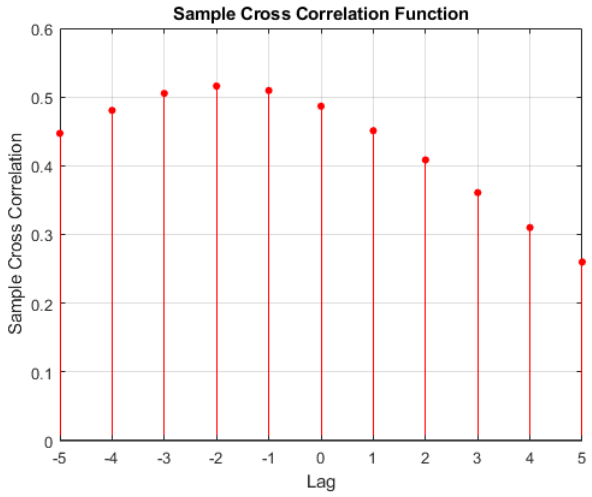

Figure 3.21: Graph of correlation coefficients between the heigth and the storage modulus of zone 5 for different lag.

► **Zone 4: parallel fibers bone**

Secondly, zone 4 can be analyzed. It corresponds to an area that is believed to contain parallel fibers bone. The height and storage modulus map for this region are shown in FIGURE 3.22.

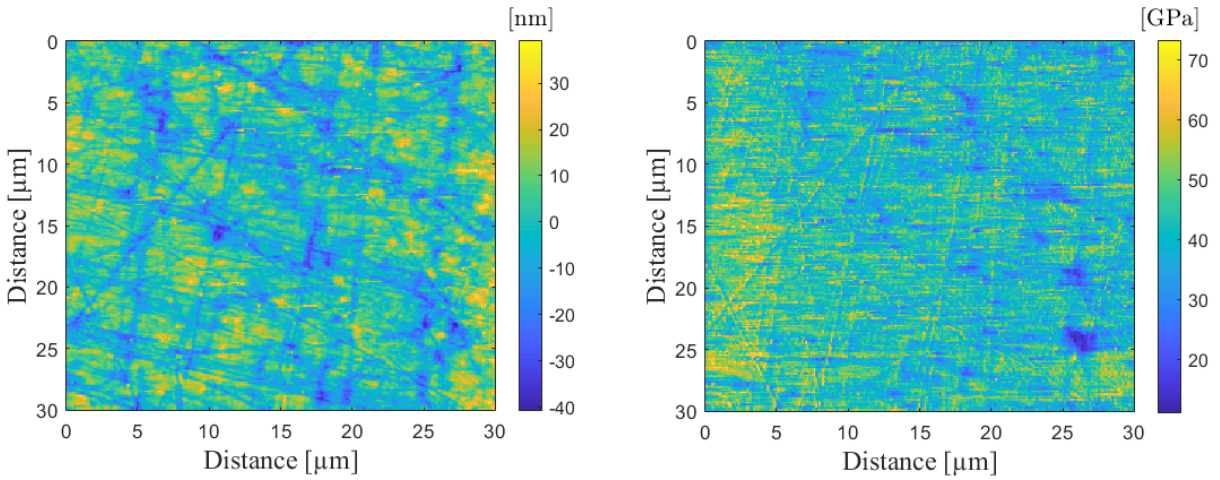

Figure 3.22: From left to right: map of the height in nm and map of the storage modulus in GPa, both for the region 4.

Several things can be learned from this. First of all, some scratches are visible on the image of the height but they are much less visible on the image of the storage modulus. This means that the storage modulus has not been influenced by the topography, which gives high quality data that represents what it should. Secondly, overall, no features stand out in the images, the maps seem more or less uniform. The parallel fibers bone therefore has mechanical properties that are uniform. To verify this, a profile was made by drawing a line from top to bottom of the area. The average of each thickness of the line was calculated as in the case of zone 5. The result obtained is shown in FIGURE 3.23. We can see on this graph that the signal oscillates a lot but the average remains relatively constant.

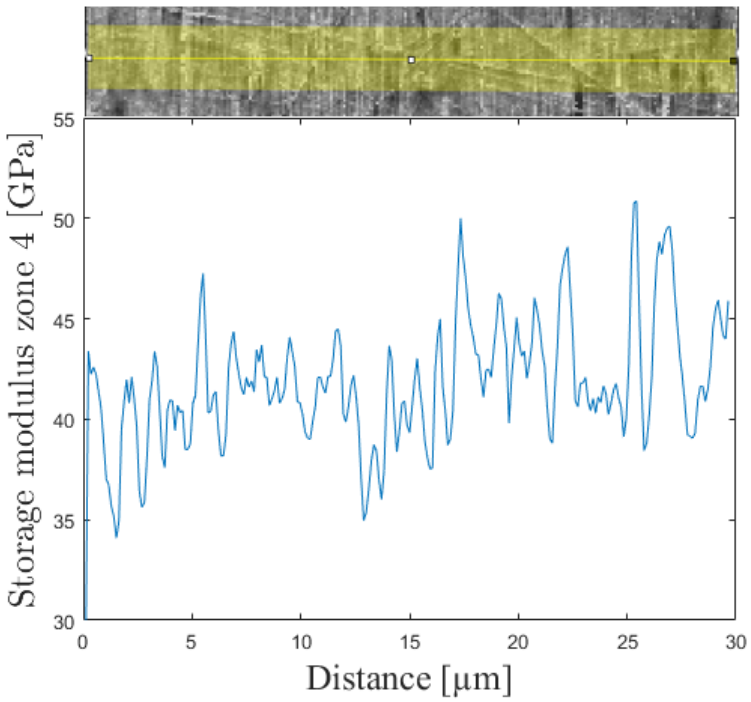

Figure 3.23: Profile of the storage module through a bone region with parallel fibers.

The storage modulus of this area was quantified by calculating its mean and standard deviation taking into account several areas. The values obtained are in the TABLE 3.3.

	Storage modulus [GPa]
Parallel fibers bone	42.65 ± 3.93

Table 3.3: Average and standard deviation of storage modulus for parallel fibers bone.

Then the correlation between the height and the storage modulus can be investigated. For that, the graph presented in FIGURE 3.24 was generated. We can see that the correlation coefficients found remain very low whatever the value of the lag. This means that the correlation between the two is almost zero. This supports what has been observed earlier thanks to the maps which show well that scratches are present on those of the height and much less on those of the storage modulus.

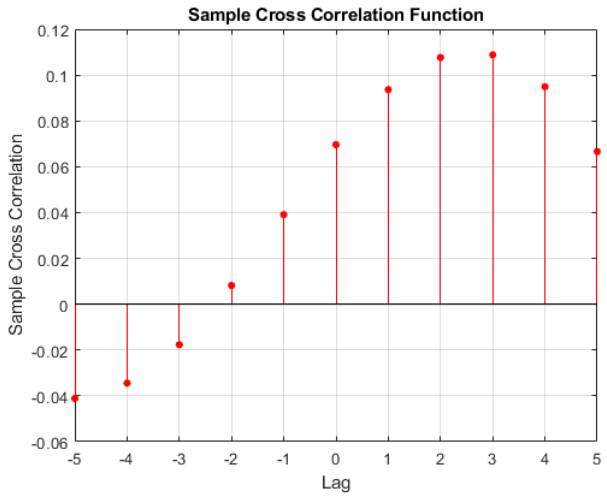

Figure 3.24: Graph of correlation coefficients between the heigth and the storage modulus of zone 4 for different lag.

► Zone 3: central layer

The last area that needs to be studied to have reviewed all the different parts of a fibrolamellar bone unit is zone 3 which contains the central part.

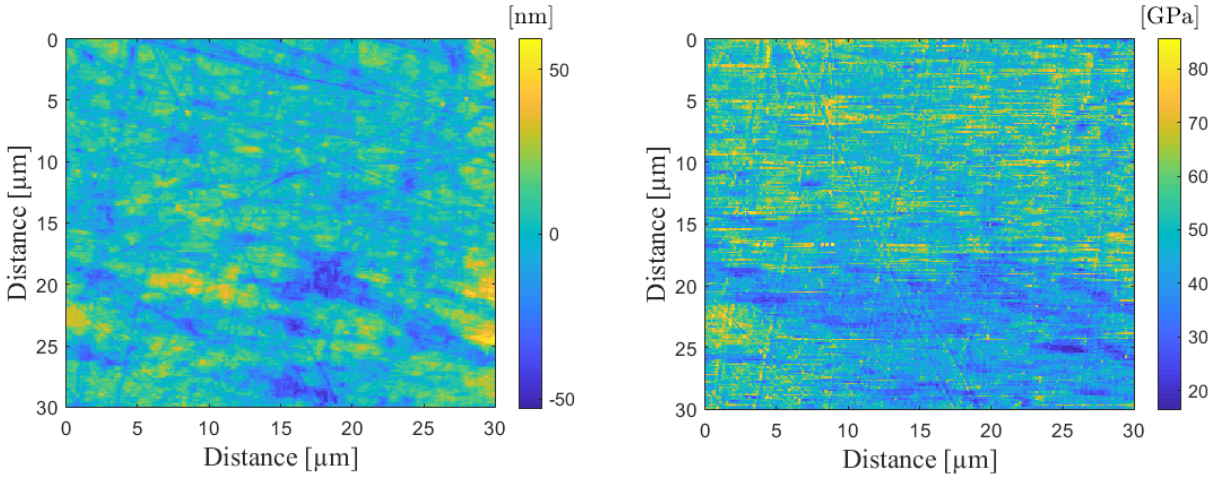

Figure 3.25: From left to right: map of the height in nm and map of the storage modulus in GPa, both for the region 3.

The maps for the height and for the storage modulus have been generated again. They are represented in FIGURE 3.25. Looking at the height, the bottom half seems to have more yellow and blue areas which means that they have some valleys and hills. As for the storage modulus, the map is clearly cut in half with the bottom half looking bluer than the top half which means it has a lower storage modulus. This area probably corresponds to the central layer explained in the literature and identified by SEM and indentations since the position matches to the position identified with the static indents. A profile, going from the top to the bottom of the region, was generated in the same way as for the other areas. The result is presented in FIGURE 3.26.

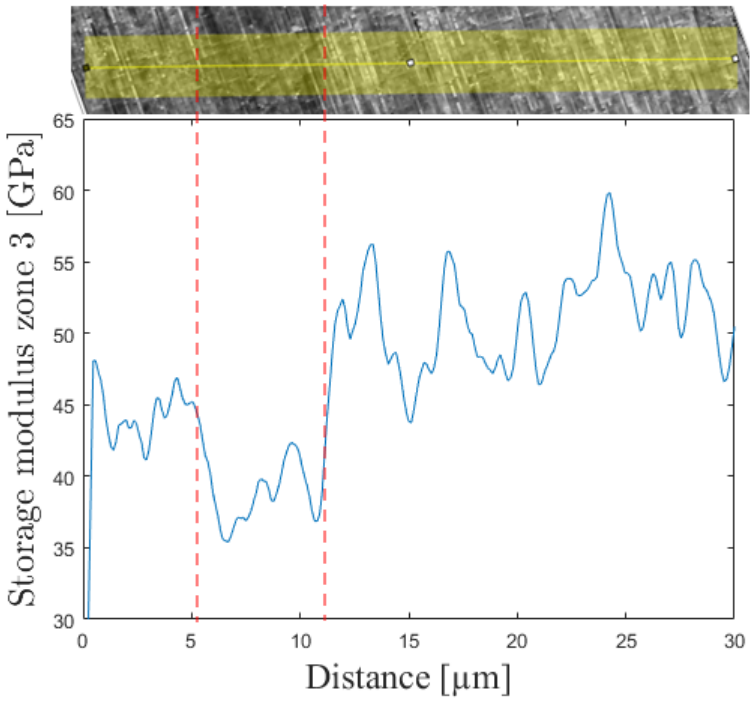

Figure 3.26: Profile of the storage module through the central layer.

The right part of the graph obtained corresponds to the lower part of the map. The graph shows the trend observed on the complete map: the right part has a lower storage modulus than the left part. The values of this storage modulus have been quantified with the same technique as for the two other areas studied. The results are written in the TABLE 3.4. They were compared to the results obtained for the parallel fibers bone and a significant difference was found ($p<0.05$).

	Storage modulus [GPa]
Central layer	38.11 $\pm$ 1.89

Table 3.4: Average and standard deviation of storage modulus for central layer.

Finally, the correlation between height and storage modulus for the latter area can be studied. For this, the graph of FIGURE 3.27 was generated. We can see in this case that the correlation is negative and that for a lag of 0 the coefficient is -0.2 which means that the correlation is poor. This confirms what has been observed for both maps, the fact that the hills and valleys visible for the height are not apparent in the storage modulus.

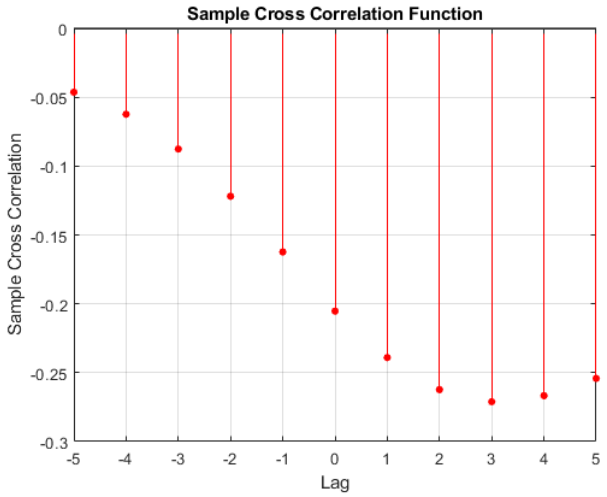

Figure 3.27: Graph of correlation coefficients between the heigth and the storage modulus of zone 3 for different lag.

► **Summary of results of the modulus mapping technique**

In this section, we investigated the mechanical properties of the different parts of a fibrolamellar bone unit. The values represented in the TABLE 3.5 were found.

	Storage modulus [GPa]
Thick lamellae	46.46 ± 3.56
Thin lamellae	32.8 ± 4.17
Parallel fibers bone	42.65 ± 3.93
Central layer	38.11 ± 1.89

Table 3.5: Summary table of the average and standard deviation of the storage modulus values found for the different parts constituting a fibrolamellar bone unit.

Thick and thin lamellae show a large variation in storage modulus with a difference of about 14 GPa on average. Their difference was determined to be significant ($p<0.05$). The central layer shows a lower storage modulus than the area where the collagen fibers are parallel. These two areas also showed a significant difference ($p<0.05$). Overall, the thin lamellae represent the parts with the lowest mechanical properties and the thick lamellae with the highest. In addition, the correlation between height and storage modulus was investigated and it was found that only the area where lamellae are present has a high coefficient indicating a strong correlation.

3.4 High load fracture analysis

A last test was performed in the framework of this master thesis to investigate qualitatively more deeply the mechanical properties of a fibrolamellar bone unit. This test consists of making indents in the bone but this time with a high load, which can potentially induce cracks. If the material is uniform, the crack created at the corner moves in a straight line, whereas if it is not uniform, the crack may be deflected. The load chosen was equal to 0.5 N, which is much higher than the loads used during modulus mapping and static indents. The different features of a unit have been studied: lamellar bone, parallel fibers bone, interface between both and the central layer. Two different units were investigated. The first one is

shown in FIGURE 3.28. In this area, an indent, representative of other indents in the same type of area will be studied. This one is framed by a square and is named 1 in FIGURE 3.28.

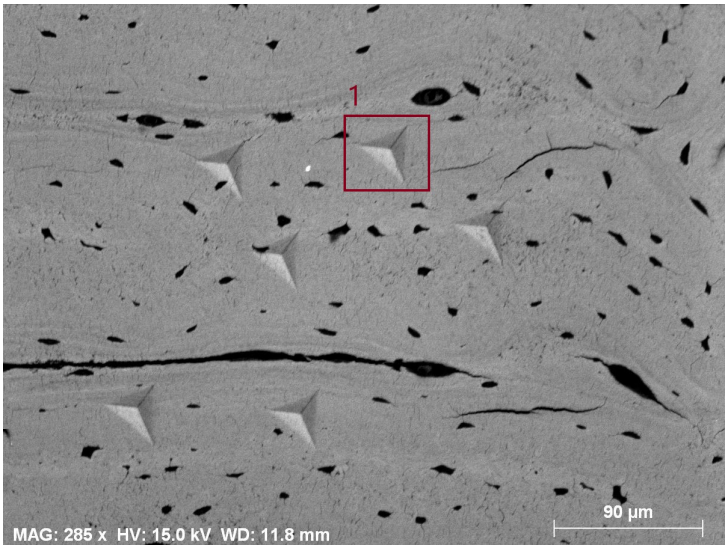

Figure 3.28: Zone 1 investigated with high load indents.

A zoom of this indent was made to better see the cracks created by it. The upper right corner has a crack that is not in a straight line but is deflected as further shown by zooming in on this crack in FIGURE 3.29. This means that the material is not uniform. This corresponds to the interface between the parallel fibers bone and the lamellar bone.

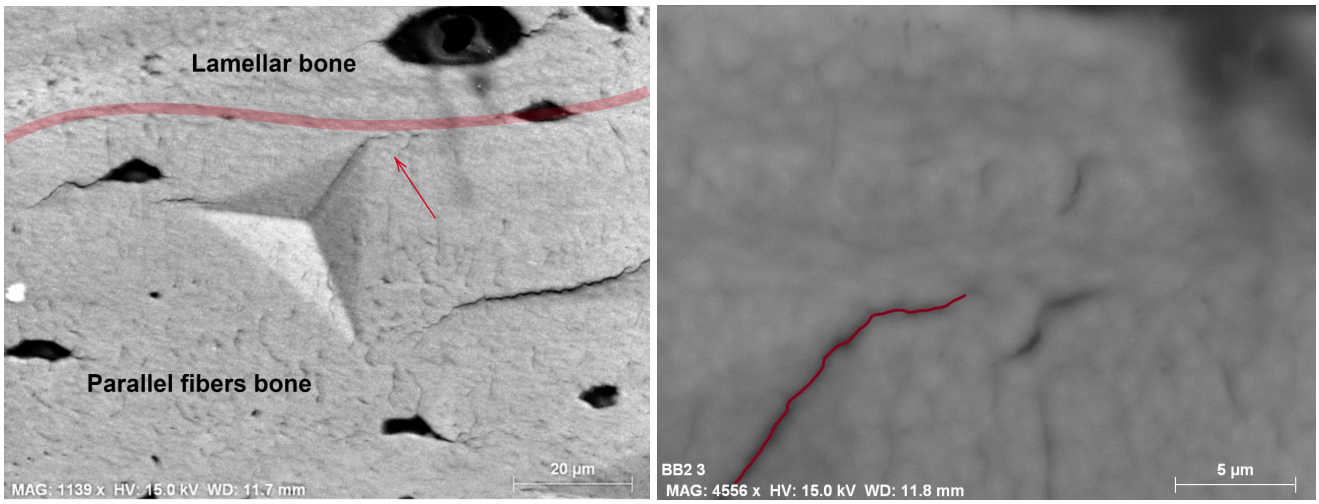

Figure 3.29: From left to right: zoom on the studied indent number 1 and zoom on the upper right corner with the crack highlighted in red.

A second area was investigated and in this one, three indents, representing the behavior of other indents of the same type of structure are be studied.

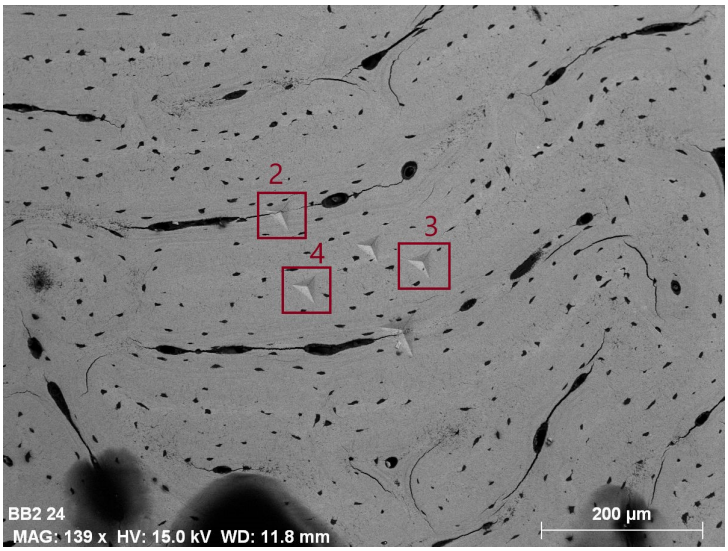

Figure 3.30: Zone 2 investigated with high load indents.

First, indent 2 lies entirely within the lamellar bone. On its zoom present on the left in FIGURE 3.31, it can be seen in the three corners that no crack has appeared. Secondly, the indent 3 can be analyzed. This one is entirely in parallel fibers bone. On the right in FIGURE 3.31, cracks are visible at the three corners. These are in a straight line to the indent, which means that the material is uniform. This confirms the fact that the parallel fibers bone is organized in a very precise and uniform way.

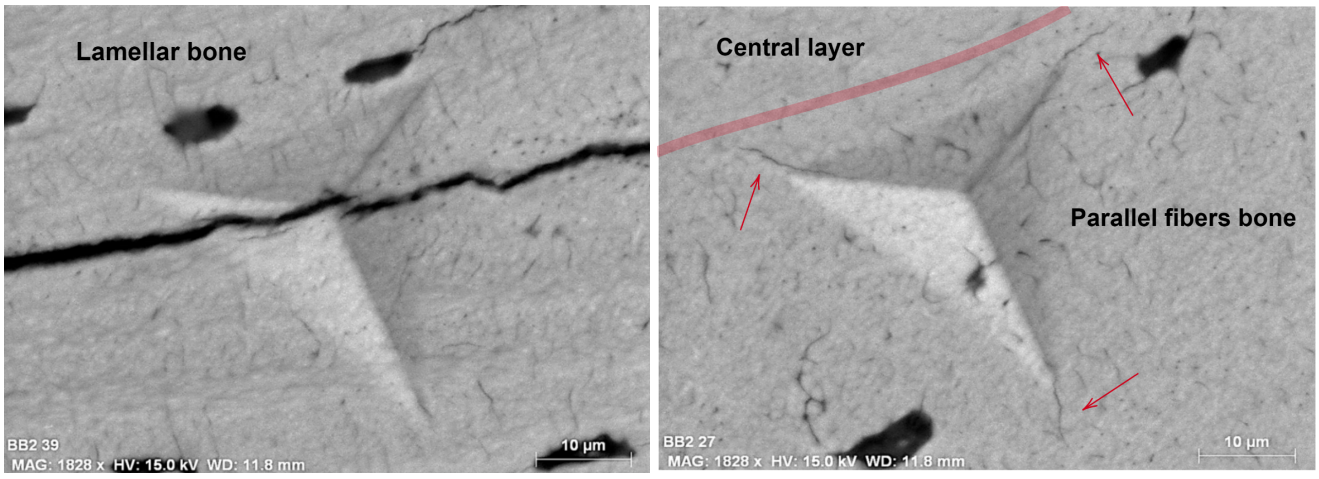

Figure 3.31: From left to right: zoom on the indent number 2 and zoom on the indent number 3.

The last indent, number 4 and visible in FIGURE 3.32, can be studied. Its upper right corner appears to be in the central area. Not really knowing the location of this area, the observations made for this indent will only be guesswork. At these corners, two cracks are visible: one at the upper right corner and the other at the bottom corner. The two cracks are not of the same length, the one at the top, present in what we think is the central line, is bigger than the one at the bottom corner, present in the parallel fibers bone.

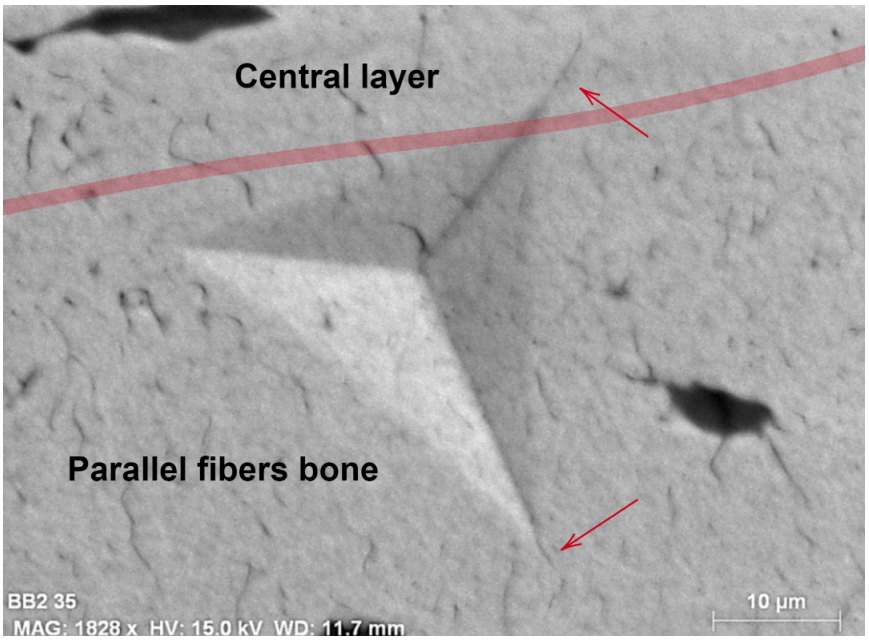

Figure 3.32: Zoom on the indent number 4.

Chapter 4

Discussion

In this last chapter the results are discussed for the different tests performed and they are compared with the literature. After, the limitations encountered throughout this master thesis are exposed and some perspectives are proposed.

4.1 Scanning electron microscopy

Thanks to the scanning electron microscope, several points can be deduced.

Firstly, with all the observations did with the chemical composition tests, it would seem that the fibrolamellar bone has a homogeneous composition throughout its structure. The fact that features present in the bone are visible in the BSE image does not indicate a difference in composition in our case. This is probably due to the influence of the topography which is still visible in this type of image which indicates, for example, that they have not all reacted in the same way to grinding and polishing.

Secondly, if the composition is considered homogeneous, the fact that the lamellae are highlighted after etching is not due to a difference in minerals but is due to different degrees of demineralization. Two reasons can explain this variance: whether it is due to different orientations of collagen fibers or to a dissimilar packing of these fibers. The collagen fibers and minerals are arranged differently between the lamellae, so the acid does not penetrate in the same way and the dissolution of the minerals is not the same everywhere. These findings remain theories since we were unable to see the orientation of the collagen fibers.

Thirdly, the fact that the osteocytes are aligned with respect to the lamellae and the central line was also observed by Kerschnitzki et al. [45] as said in SECTION 1. Indeed, they found that the osteocytes were aligned on the surface of the primaries. In the case of fibrolamellar bone this corresponds to the central line on which the bone structure grows. The fact that this structure is a primer explains that more osteocytes are found in this layer where the osteoblasts begin their synthesis process at the same time. This is typical of bones that must grow rapidly. These observations prove that there is a difference in the organization of the central layer if the line of osteocytes observed corresponds to this line.

Then, the central layer deserves a deeper investigation to know its composition. Indeed, in this work we found that it had the same composition as the other parts, and it differs only by its structure which seems different from the other parts (random lines). The composition is in contradiction with the literature. We must then test by improving the contrast and/or the resolution of the microscope to see if we obtain results similar to those of the literature.

Finally, to our knowledge, no study has quantified the size of the lamellae present in fibrolamellar bone. Therefore, a comparison with the lamellae present in osteons is made. This will allow to see the differences and/or similarities between these lamellae. The size of the lamellae has been investigated in several studies for both human (Hengsberger et al. (2002) [78] and Xu et al. (2003)[79]) and bovine bones (Zhou et al. (2020) [80]). They found similar ranges of values (3-5 µm for thick and <1-3 µm for thin lamellae) to those established in this work. As noted in studies and in the results of this work, these values differ in the structure of the bone, but this nevertheless gives an idea of the size and proportion. In the paper by Xu et al. they also investigated the Ca and P composition of the lamellae of osteons. They found no difference which means that the lamellae have the same chemical composition [79]. This supports the results obtained in this work which also shows a uniform composition of the whole bone and therefore of the lamellae.

4.2 Static indentations

When observing the results obtained with the static indentation grid, we noticed that the lamellae were not distinguishable. This is due to too low a resolution that does not allow us to differentiate them. Indeed, each indent is separated by 6 µm so as not to influence the others. But given the size of the lamellae calculated thanks to the BSE images, this resolution is not sufficient to detect them. In addition, the indents are not correctly placed, i.e. they do not follow the lamellae. On the same line, some points are in the thin lamellae, some are on the thick lamellae and the last ones are in between. In order to properly study the properties of the lamellae, it is necessary to place the indentations correctly i.e. that the indentations follow the lamellae. Moreover, we also need to make sure that the deformation area induced by the indentation is just influenced by the characteristics of the region under study and not by the features of the neighboring regions. A solution would be to program them all manually to choose exactly where they are made but this is very time consuming. To overcome these problems, the modulus mapping method, with a lateral resolution of 20 nm, is the most suitable solution.

4.3 Modulus mapping

In this subsection, the results obtained with the modulus mapping technique are discussed and compared to the results of other sections and to the literature.

- **Modulus mapping results**

Firstly, we can talk about the correlation between the height and the storage modulus of each zone. For the three areas, only area 5 which corresponds to the lamellar bone shows a strong correlation. The other regions show a weak one which proves that the topography has no influence on the storage modulus measurements. As for the 5, the fact that the correlation is strong between the height and the storage modulus can be explained. Indeed, the thick lamellae show a higher storage modulus while the thin ones appear softer. During the polishing stage, the less stiff areas have been the most eroded, they appear more hollowed while the stiffer areas appear more rounded because they have been less polished due to their mechanical properties. The same observation has been made by Xu et al. who found that thin lamellae are easier to wear out during polishing than thick ones [79].

Secondly, the collagen fibers of the thick lamellae must be mostly oriented in the direction of the main axis of the bone since they present the highest storage modulus values. Following a statistical test, the difference between their storage modulus was shown not to be significant ($p = 0.1528$). This reinforces the hypothesis that the fibers are potentially oriented in the same direction along the main axis of the

bone. This remains to be verified, but it has already been shown in osteons that lamellae containing mainly parallel fibers are thicker than those containing oblique fibers [81]. The difference between the thick lamellae and the parallel fibers bone would then be due to a difference in packing.

- **Comparison with the other results**

The results can be compared with those obtained for the chemical composition. In the latter tests, it appears that the bone has a uniform composition. The mechanical properties prove that the different parts of the bone are not similar due to their variations. The difference in properties cannot be explained by the fact that there are more minerals or not. The solution would then be that the dissimilar parts present differences in the organization of collagen fibers and minerals. This observation supports the one made with etching.

For the map of the height of the central area, valleys and hills appear. This can be correlated with the BSE images obtained with the microscope. Indeed, on the latter, the central area is visible thanks to lines that intersected randomly. This corresponds to the observation made with the modulus mapping. It would seem that we can conclude that the central line presents a different organization which would be made of collagen fibers arranged in all directions, as said in the literature.

Then the storage modulus values obtained for the central layer and the parallel fibers bone with the static indents and those with the modulus mapping can be compared. A comparison of the lamellae cannot be made, as they are not visible during the static indentation test. The same trend can be seen: the central layer presents a lower storage modulus than the part of parallel fibers. However, higher values were obtained with the modulus mapping for both the central part (39.11 vs. 20-25 GPa) and the parallel fibers (42.65 vs. 26-33 GPa). Since the two methods are different, only the relative difference between the values can be compared. The fact that the central layer has worse mechanical properties than the parallel fibers bone zones is due to its random organization.

- **Comparison with the literature**

In terms of composition and structure, in the literature, researchers found that the central zone is hypercalcified. Looking at the chemical composition, we did not find any difference in calcification there. One explanation could be the fact that the bone is of a certain age which makes the mineralization maximum everywhere and therefore equal in all parts of the bone. Weaker mechanical properties may then be due to the organization of collagen fibers in this layer. The part with parallel fibers has high mechanical properties because the fibers are oriented in the direction of the stress and it is in this direction that they are strongest since it is reinforced. While in the central part, the fibers are randomly oriented, as seen in the literature and in our observation of the topography, so that no direction is strengthened and therefore it has less strong mechanical properties.

In terms of mechanical properties, for fibrolamellar bone, we have seen in the background that the different parts of a unit have not been studied separately except by Seto et al. who investigated the part containing the parallel collagen fibers of wet bovine sample. They found by static indentations that this part had a Young's modulus of 23.1±0.7 GPa. In this work, the Young's modulus of this same part is equal to 30 GPa for the static indents and 42.65±3.93 GPa for the modulus mapping. The value obtained by Seto et al. can be compared to the value acquired with static indents but not with modulus mapping because they are two different methods. They found a lower value than the one we calculated. This can be explained by the fact that they tested wet samples while this work is based on dehydrated samples. It has been proven that dehydrated samples have a higher Young's modulus than wet ones.

In view of the lack of literature about the mechanical properties of fibrolamellar bone, the values obtained for the thick and thin lamellae can be compared to the values found in the literature of osteon lamellae. Different studies have tested bovine (Zhou et al. (2020) [80], Carnelli et al. (2013) [82] and Liu et al. (2018)[83]), humans (Gupta et al. (2006) [84] and Xu et al. (2003)) or porcine samples (Feng et al. (2012)[85]), wet or dehydrated. In each case the same trend is observed: the thick lamellae have elastic modulus higher than the thin one. This corresponds to what was obtained with the modulus mapping in this master thesis. Since the different studies worked on wet and dry samples, only the relative differences can be compared. In most studies, a small difference between thick and thin lamellae is observed, ranging from 3 to 4 GPa while in ours a much higher difference of 14 GPa is obtained. Only one study, conducted by Zhou et al., found a difference of 12 GPa, close to ours. This is the only study that has used modulus mapping like the one conducted in this master thesis. Even if the static indentation method and the modulus mapping method cannot be compared, such a gap between the relative difference of the Young's modulus of the lamellae can be explained. The indents have a low lateral resolution because they must be spaced far enough apart to ensure that the plastic zone they generate does not influence the others. The distance between two indents in our case has been defined at 6 µm. The thin lamellae having a thickness of 1 µm, it is possible that their plastic deformation zone encroaches on the thick lamellae. The thick lamellae being then taken into account in the measurements and having a higher Young's modulus, the Young's modulus obtained for the thin lamellae is higher. This reduces the relative difference between the two types of lamellae. Looking at this, we can say that fibrolamellar bone lamellae seem to follow the same trend as osteon lamellae since thin lamellae always present lower mechanical properties than thick ones.

4.4 High load indentations

In this part, we found that the cracks seem to be deflected by the lamellae and that they do not penetrate them. It thus appears that the lamellae hinder the propagation of the microcracks to potentially protect the blood vessels. This may mean that there is an interface between them and the parallel fibers bone.

Second, no cracks were observed when the indent was entirely contained in lamellar bone. This observation reinforces the fact that the lamellar bone is there to protect the blood vessels. Its well-organized structure prevents crack formation.

Then, the corners present in the parallel fiber bone present cracks that go in a straight line. This means that this area is uniform and well arranged.

Finally, an indentation between the central layer and the parallel fibers bone was made. The crack present in the central layer is greater than the one in the parallel bone. With these findings, it would seem that the central layer is more conducive to crack propagation than the parallel fibers bone. This is consistent with the fact that this layer presented weaker mechanical properties due to its poorly order organization in static indents and modulus mapping measurements.

4.5 Limitation

Several limitations were encountered during the realization of this master thesis. To improve the results obtained, it is interesting to work on them.

The most substantial limitation that caused the most problems was the resin. The protocol for using this resin comes from the Ludwig Boltzmann Institute of Osteology in Vienna, which is renowned in

bone research. Their sample preparation procedure is well established and the samples they obtain are of high quality, that is why it was chosen. However, some issues encountered with this resin probably remain due to a bad reproduction of the protocol. The first problem was the evaporation of the resin in the incubator. The solution of closing the molds entirely with paraffin allowed to reduce the evaporation but it was not completely eliminated. Because of this, some prepared samples were not embedded in enough resin, which made them unusable. Also, on the top of the molds, about 0.5-1 cm of resin did not cure and had to be cut off. If the resin has evaporated, only this part remained to embed the sample but being soft, the sample was again not usable. One additional remark to make is that this resin, even after polymerization, kept being relatively soft in contrast to more conventional resins. After the samples were prepared, other complications occurred with the resin. Indeed, bubbles appeared on the sample when the electron beam of the microscope was scanning it. The heat brought by this beam activated the polymerization of the resin which was visibly not polymerized in the holes and this one then came out of certain holes making these parts of the sample unusable. This phenomenon can be seen in FIGURE 3.5 where a first scan was performed and when a zoom was executed on a part, a resin bubble appeared. Finally, we also noticed that the resin was not stable in time. Indeed, the samples were stored in a temperature-controlled cabinet in the nanoindenter room for about 3 weeks. After this time, a new exploration with the microscope allowed to see that large resin bubbles/stains had appeared everywhere on the sample, this time larger than those caused by the electron beam. Theses bubbles are visible in FIGURE 4.1. In conclusion, the resin remains a considerable point to improve to ensure a better quality of our samples.

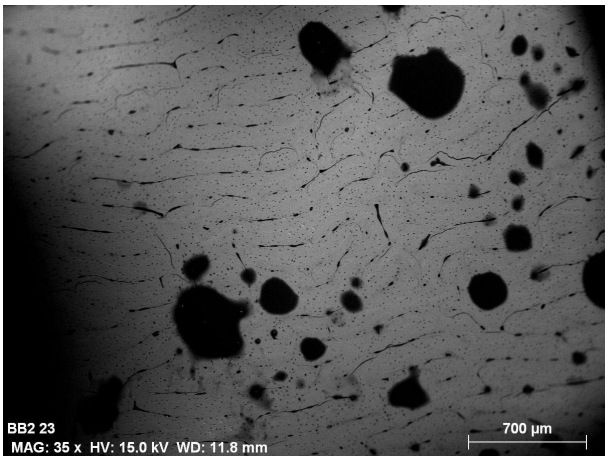

Figure 4.1: BSE image of the sample number two after 3 weeks of storage.

The second limitation is the unknown age of the samples. This is important when studying the bones as their composition and structure (due to bone remodeling) depend on it. For future studies, it is interesting to take note of it. Moreover, due to a forgetfulness, the position from which the samples were collected was not noted. However, the mechanical properties depend on the position in the bone. Knowing the location would be a plus to analyze the mechanical properties and to compare the results of different locations. As the results were very time consuming, few areas were investigated. To consolidate the results, it would be interesting to explore more areas on different samples from different locations.

The last limitation encountered is the modulus mapping. Indeed, this technique is recent, highly complex and not widely used, so the results obtained with it should be taken with care. Moreover, this method being super precise, it makes particularly sensitive. Some measurements give higher values than expected and we have not been able to explain this. Ideally, results should be verified by FE simulations. However, during this master thesis, a lot of time was dedicated to the understanding of this method and to the implementation of a protocol which did not leave enough time to perform simulations.

4.6 Future works

As a first perspective, it is interesting to continue this work on fibrolamellar bone with deeper analysis. First, the limitations encountered in this work must be resolved such as the resin, the age of the animal and the location of the sample in the femur. For the resin, after a discussion with Markus Hartmann of the Ludwig Boltzmann Institute of Osteology in Vienna, it appears that the quantities used to manufacture the resin must be reviewed and that more suitable molds, higher, made of PMMA (same material as the resin) and provided with a cap solider than paraffin can be used. It is therefore interesting to try these new improvements. Then, other techniques can be exploited to provide additional information. For example, it would be interesting to perform Quantitative Backscattered Electron Imaging (qBEI). This method allows to quantify the concentration of calcium in the different parts of the bone whereas BSE images only allow to see the contrast of the differences in composition. This is particularly interesting for the central layer to support the results of this work or the results of the literature. In addition, fracture tests can also be used to quantify the fracture toughness of the material. The fact that the lamellae deflect the cracks should also be studied in depth to try to determine whether or not an interface exists, specifically dedicated to this deflection much like the cement line in osteons.
In addition to the work, FE simulations can be performed to verify the results obtained with the modulus mapping method. Indeed, as explained in this work, modulus mapping being a very complex technique and the bones having microscale features (1 µm for fine lamellae for example), some measurement problems may appear. For example, measurements on inclusions smaller than the tip radius could be altered since the tip would rely on adjacent regions which do not have the same mechanical properties. Also, the impact of surface roughness due to polishing on the measurements is not known. Measurement problems could appear if a height difference is too important at the level of the lamellae, for example. These phenomena can then be explained and their impact evaluated through simulations.

A second interesting perspective would be to apply the protocol implemented in this work to the cement line, a peculiar structure of great interest. As explained in the background, the cement line is a particular layer that surrounds secondary osteons in cortical bone and bone packets in trabecular bone. It has been shown in experiments that microcracks are more likely to occur in the interstitial bone (bone that remains after bone remodeling and surrounds osteons) than in the osteons [86]. The cement line could then play a protective role for the blood vessels by deflecting the microcracks [2, 87]. This layer seems to play a crucial role in crack propagation, but it is not well understood and remains a controversial subject [88]. Some researchers thought and demonstrated by experiments that the cement line was hypo-mineralized [89, 90], and others found that it was on the contrary hyper-mineralized [2, 11, 91]. In more recent studies, the researchers, thanks to the scanning electron microscope, have highlighted a cement line that appeared brighter than what surrounds it, that is to say with a higher atomic contrast [92]. The organic matter in this layer is also a problem. Researchers do not agree on whether it is rich or poor in collagen, which is the arrangement... . Moreover, the mechanical properties (fracture toughness and Young's modulus for example) are not known. We can therefore say that the cement line in cortical bones is little studied and that it needs to be investigated. This structure is complex to study because of its size (between 1 and 5 µm) and because it is a 3D structure and when 2D measurements are made, nothing ensures that it is the cement line that is studied. For trabecular bones, no data are available. The cement line presenting interesting properties, it would be useful to study it more in depth by applying this high resolution tool that is modulus mapping. This method would allow to highlight the difference in mechanical properties between the cement line and the surrounding bone tissue further supporting the assumption that cement line acts as an effective interface which dissipates energy and hinders crack propagation.

Conclusion

The aim of this master thesis was to use a complex and fairly new nanoscopic mechanical characterization method based on nanoindentation and called modulus mapping, to analyze with high spatial resolution the mechanical properties of a fibrolamellar bone unit.

The implementation of a protocol for using the modulus mapping was the first part of the master thesis. From this, the following important points have been drawn:

- The tip must be washed because tiny particles on it can falsify all measurements.
- On the bone, a static force of 1 µN and a load amplitude lower than this value must be used.
- The tip must remain engaged between each measurement so that they are reproducible and to ensure consistent results between them.

In the second part of the thesis, fibrolamellar bone was investigated at the nanoscale using several techniques including modulus mapping. With the results, we concluded the following points:

- The chemical composition of the fibrolamellar bone is homogeneous.
- The central layer has a different architecture from the other parts and contains many osteocytes that are in its direction.
- The central layer has a smaller storage modulus than the parallel fibers bone zones. This may be due to its weak organization. The thin lamellae are less stiff than the thick ones. The thick lamellae and the parallel fibers bone represent the stiffest parts of the fibrolamellar bone unit. Probably being oriented in the same way , the non-significant difference of the two may be due to a higher packing density.
- Since fibrolamellar bone has different mechanical properties in different parts of a unit but has a uniform chemical composition, the changes must be due to a difference in the organization of the collagen fibers and minerals especially their orientation and packing.
- The lamellae surrounding the vessels deflect the cracks and are therefore there to protect them.
- The central line appears to be more conducive to crack propagation than the parallel fibers bone. The latter with straight line cracks can therefore be considered as uniform.
- The lamellae of fibrolamellar bone resemble the lamellae of osteons in many respects. They have the same size range for their thickness, in both cases the chemical composition is uniform and finally, the same trend in mechanical properties is observed.

This work provides for the first time a consistent method to study in detail the local nanosclale elastic and fracture properties of fibrolamellar bone and reports them in order to understand how nature combines the conflicting requirement of rapid bone growth with good mechanical properties. Future work may focus on the central layer to determine its composition using quantitative techniques such as qBEI and maybe apply this process to the unexplored cement line.

Appendices

Appendix A

Calibration on bone samples

Here are the values obtained for height, amplitude, storage stiffness and storage modulus for different frequency values on fibrolamellar bone and after there are the map for the storage stiffness for the 6 frequencies.

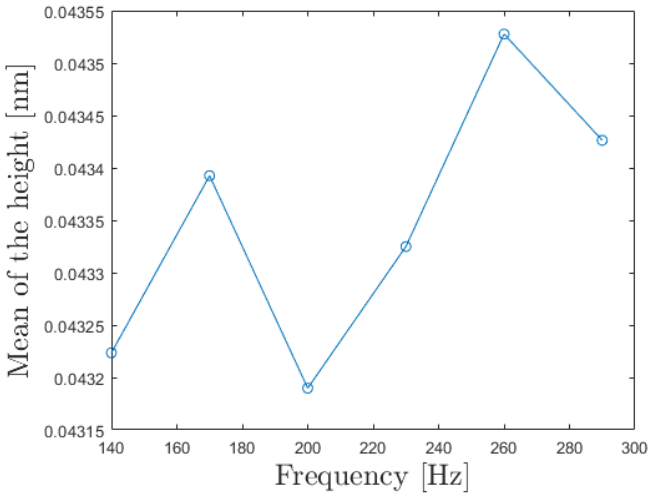

(a) Mean of the height [nm] for each frequency.

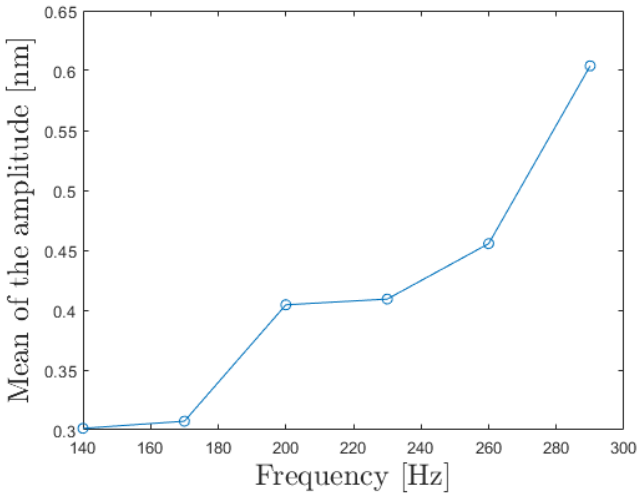

(b) Mean of the amplitude [nm] for each frequency.

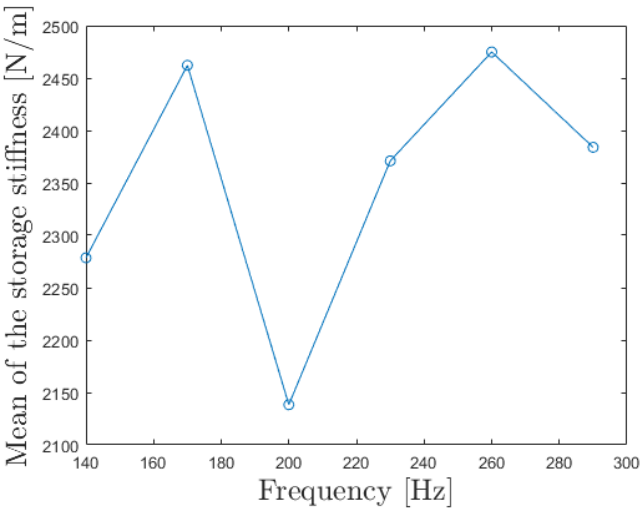

(c) Mean of the storage stiffness [N/m] for each frequency.

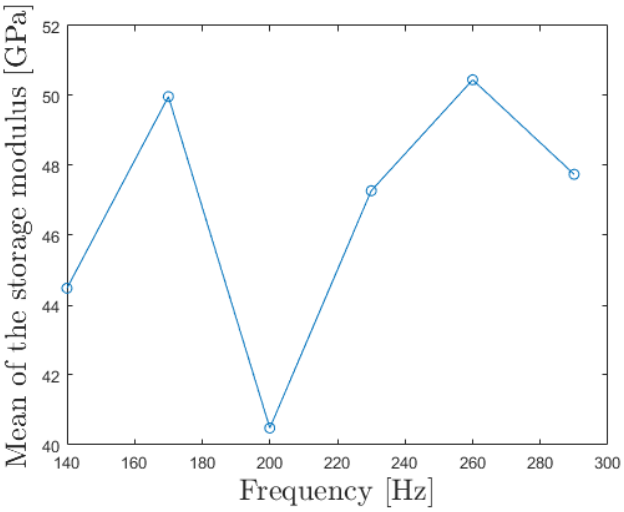

(d) Mean of the storage modulus [GPa] for each frequency.

Figure A.1: Mean of the height, the amplitude, the storage stiffness and the storage modulus for each frequency.

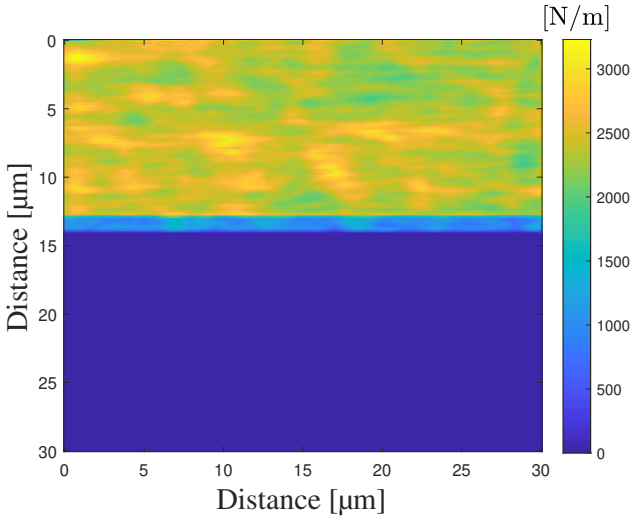

(a) Storage stiffness with a frequency = 140 Hz.

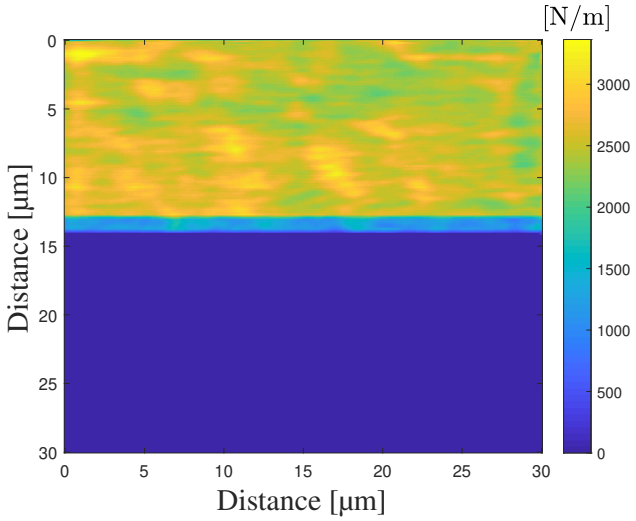

(b) Storage stiffness with a frequency = 170 Hz.

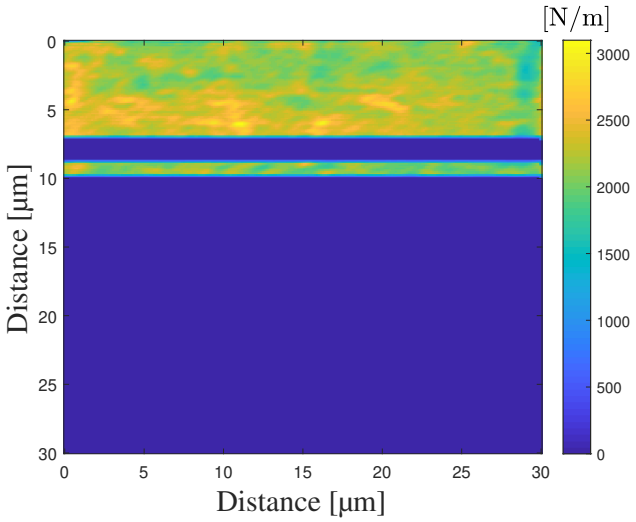

(c) Storage stiffness with a frequency = 200 Hz.

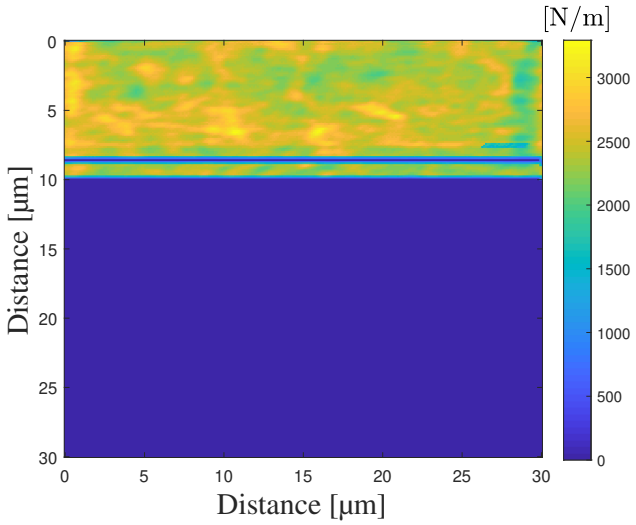

(d) Storage stiffness with a frequency = 230 Hz.

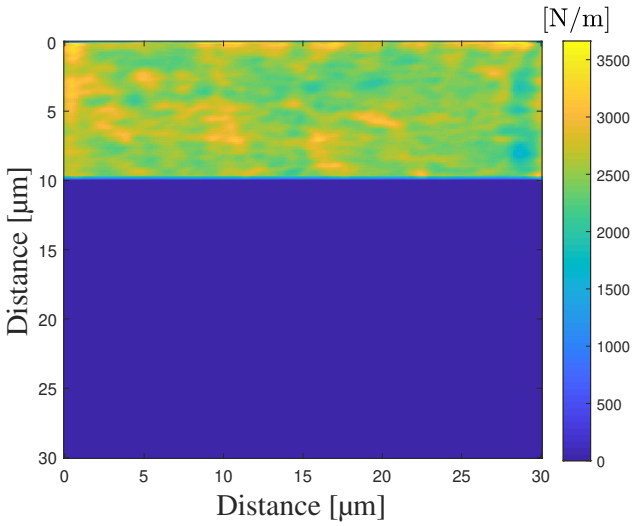

(e) Storage stiffness with a frequency = 260 Hz.

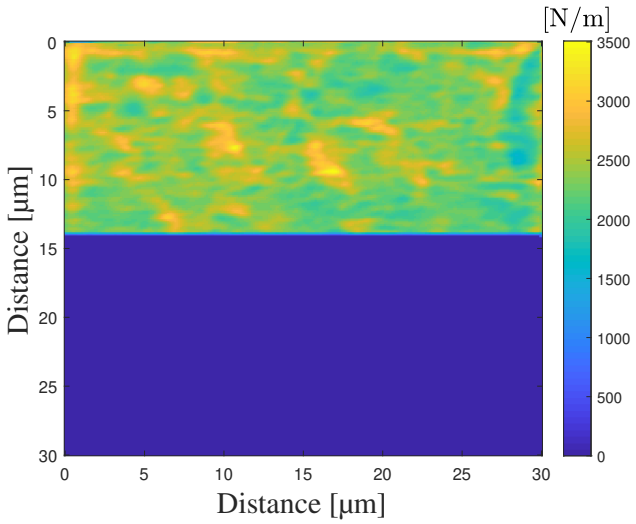

(f) Storage stiffness with a frequency = 290 Hz.

Figure A.2: Storage stiffness [GPa] obtained for different frequencies.

Bibliography

[1] SHEA GUNTHER. *8 Amazing Examples of Biomimicry*. https://www.treehugger.com/amazing-examples-of-biomimicry-4869336, (Last access on 2021-05-30).

[2] W. WAGERMAIER, KLAUS K. AND P. FRATZL. *Fragility of Bone Material Controlled by Internal Interfaces*. *Calcified Tissue International*, 97(3):201–212, 2015.

[3] J. W. BARRERA, A. LE CABEC AND M. M. BARAK. *The orthotropic elastic properties of fibrolamellar bonetissue in juvenile white-tailed deer femora*. *Journal of Anatomy*, 229:568–576, 2016.

[4] J.D. CURREY. *The many adaptations of bone*. *Journal of Biomechanics*, 36:1487–1495, 2003.

[5] J. D. CURREY. *BONES, Structure and mechanics*. Princeton University press, 2002.

[6] CLEVELAND CLINIC. *Musculoskeletal system*. https://my.clevelandclinic.org/health/articles/12254-musculoskeletal-system-normal-structure--function#:~:text=Your%20musculoskeletal%20system%20includes%20bones,problems%20with%20movement%20and%20function, (Last access on 2021-03-26).

[7] D. RUFFONI. *GBIO0012-2 Biomechanics slides*, chapter : Bones. University of Liege, 2019.

[8] WIKIPÉDIA. *Os*. https://fr.wikipedia.org/wiki/Os, (Last access on 2021-05-01).

[9] HEALTHLINE. *Bone Function: Why Do We Have Bones?* https://www.healthline.com/health/bone-health/bone-function, (Last access on 2021-05-01).

[10] LAROUSSE. *Variétés d'os*. https://www.larousse.fr/encyclopedie/images/Vari%C3%A9t%C3%A9s_d_os/1001991, (Last access on 2021-05-01).

[11] H. FRANCILLON-VIEILLOT ET AL. *Skeletal Biomineralization : Patterns, Processes and Evolutionary Trends*, chapter 20 - Microstructure and mineramization of vertebrate skeletal tissues. Joseph G. Carter editor, 1990.

[12] DEVICH DESIGN. *Bones*. http://devichedesigns.com/work/bones, (Last access on 2021-04-14).

[13] M.J.F.BLUMER. *Bone tissue and histological and molecular events duringdevelopment of the long bones*. *Annals of anatony*, (235):1–11, 2021.

[14] M. R. ALLENA, J. M. HOCK, D. B. BURR. *Periosteum: biology, regulation, and response to osteoporosis therapies*. *Bone*, 35:1003 – 1012, 2004.

[15] DEPTS.WASHINGTON.EDU. *The O' Cells*. https://depts.washington.edu/bonebio/bonAbout/bonecells.html#:~:text=These%20old%20osteoblasts%20are%20also,They%20also%20come%20from%20osteoblasts., (Last access on 2021-05-01).

[16] S. C. MILLER, L. DE SAINT-GEORGES , B. M. BOWMAN AND W. S. S. JEE. *Bone Lining Cells: Structure and Function* . *Scanning Microscopy*, 3(3):953–961, 1989.

[17] D. J. HADJIDAKIS AND I. I. ANDROULAKIS. *Bone Remodeling. ANNALS NEW YORK ACADEMY OF SCIENCES*, 1092:385–396, 2006.

[18] R. B. MARTIN, D. B. BURR, N. A. SHARKEY, D. P. FYHRIE. *Skeletal Tissue Mechanics*. 1998.

[19] T. M. KEAVENY, E. F. MORGAN, G. L. NIEBUR AND O. C. YEH. *BIOMECHANICS OF TRABECULAR BONE. Annual reviews biomedical engineering*, 3:307–333, 2001.

[20] BISHOP ET AL. *Cancellous bone and theropod dinosaur locomotion. Part I—an examination of cancellous bone architecture in the hindlimb bones of theropods. PeerJ*, 2018.

[21] P. ROSCHGER, E.P. PASCHALIS, P. FRATZL, K. KLAUSHOFER. *Bone mineralization density distribution in health and disease. Bone*, 42:456–466, 2008.

[22] E. NOVITSKAYA, P-Y CHEN, S. LEE, A. CASTRO-CESEÑA, G. HIRATA, V. A. LUBARDA AND J. MCKITTRICK. *Anisotropy in the compressive mechanical properties of bovine cortical bone and the mineral and protein constituents. Acta Biomaterialia*, 7:3170–3177, 2011.

[23] Z. MANILAY, E. NOVITSKAYA, E. SADOVNIKOV AND J. MCKITTRICK. *A comparative study of young and mature bovine cortical bone. Acta Biomaterialia*, 9:5280–5288, 2013.

[24] D. R. CARTERP AND D. M. SPENGLER. *Mechanical Properties and Composition of Cortical Bone. Section 3 basic science and pathology*, (135):192–217, 1978.

[25] A. SHARIR, M. M. BARAK AND R. SHAHAR. *Whole bone mechanics and mechanical testing. The Veterinary Journal*, 177:8–17, 2008.

[26] F. MADEHKHAKSAR, Z. LUO, N. PRONOST AND A. EGGES. *3D MultiScale Physiological Human*, chapter Modeling and Simulating Virtual Anatomical Humans. Springer London, 2008.

[27] D. J. WEBSTER ET AL. *Studying osteocytes within their environment. Bone*, 54(2):285–295, 2013.

[28] M. G. MULLENDER, R. HUISKES, H. VERSLEYEN AND P. BUMA. *Osteocyte density and histomorphometric parameters in cancellous bone of the proximal femur in five mammalian species*. 14(6).

[29] R. OWEN AND G. C. REILLY. *In vitro Models of Bone Remodelling and Associated Disorders. Frontiers in Bioengineering and Biotechnology*, 6(134):1–22, 2018.

[30] P. FRATZL AND R. WEINKAMER. *Nature's hierarchical materials. Progress in Materials Science*, 52:1263–1334, 2007.

[31] N. REZNIKOV, R. SHAHAR, S. WEINER. *Bone hierarchical structure in three dimensions. Acta Biomaterialia*, 10:3815–3828, 2014.

[32] S. RICARD-BLUM. *The Collagen Family. Cold Spring Harb Perspect Biol*, 2012.

[33] P. FRATZL AND R. WEINKAMER. *Nature's hierarchical materials. Progress in Material Science*, 19(9):1251–65, 2008.

[34] JELLAGEN - MARINE BIOTECHNOLOGIES. *What is collagen*. `https://www.jellagen.co.uk/products/wound-regenerative-medicine/medical-grade-materials/`, (Last access on 2021-04-21).

[35] S. WEINER AND W. TRAUB. *Bone structure: from angstroms to microns. FASEB J.*, 6(3):879–85, 1992.

[36] U. E. PAZZAGLIA, M. REGUZZONI, L. DEPERO, S. FEDERICI, M. BONDIONI, G. ZARATTINI AND M. RASPANTI. *The structure of cortical bone as revealed by the application of methods for the calcified matrix study*. *Microscopy research and technique*, pages 1–12, 2020.

[37] WEINKAMER, R. AND P. FRATZL. *Solving conflicting functional requirements by hierarchical structuring—Examples from biological materials*. *MRS Bulletin*, 41(9):667–671, 2016.

[38] M.E. RUPPEL, L.M. MILLER AND D. B. BURR. *The effect of the microscopic and nanoscale structure on bone fragility*. *Osteoporosis International*, 52:1263–1334, 2007.

[39] F. F. SAFADI, M. F. BARBE, S. M. ABDELMAGID, M. C. RICO, R. A. ASWAD, J. LITVIN AND S. N. POPOFF. *Chapter 1 Bone Structure, Development and Bone Biology*. pages 1–50, 2009.

[40] K. STEIN AND E. PRONDVAI. *Rethinking the nature of fibrolamellar bone:an integrative biological revision of sauropodplexiform bone formation*. *Biological reviews*, 89:24–47, 2014.

[41] W. WAGERMAIER, H. S. GUPTA, A. GOURRIER, M. BURGHAMMER, P. ROSCHGER AND P. FRATZL. *Spiral twisting of fiber orientation inside bone lamellae*. *Biointerphases*, 1(1), 2006.

[42] R. MORI, A. HIRAYAMA, T KODAKA AND M. NAKAMURA. *Histological and physicochemical studies of hypercalcified primear lines in the laminar bone of young calves*. *Anatomical Science International*, 82:108–115, 2007.

[43] R. A. MAGAL, N. REZNIKOV, R. SHAHAR, S. WEINER. *Three-dimensional structure of minipig fibrolamellar bone: Adaptationto axial loading*. *Journal of Structural Biology*, 186:253–264, 2014.

[44] M. KERSCHNITZKI, W. WAGERMAIER, P. ROSCHGER, J. SETO, R. SHAHAR, G. N. DUDA, S. MUNDLOS, P. FRATZL. *The organization of the osteocyte network mirrors the extracellular matrix orientation in bone*. *Journal of Structural Biology*, 173:303–311, 2011.

[45] M. KERSCHNITZKI, W. WAGERMAIER, Y. LIU, P. ROSCHGER, G. N. DUDA, P. FRATZL. *Poorly Ordered Bone as an Endogenous Scaffold for the Deposition of Highly Oriented Lamellar Tissue in Rapidly Growing Ovine Bone* . *Cells Tissues Organs*, 194:119–123, 2011.

[46] D. T. REILLY, A. H. BURSTEIN, V. H. FRANKEL. *The elastic modulus for bone*. *J. Biomechanics*, 7(3):271–275, 1974.

[47] G. BENECKE, M. KERSCHNITZKI, P. FRATZL AND H. S. GUPTA. *Digital image correlation shows localized deformation bands in inelastic loading of fibrolamellar bone*. *Cambridge journals*, 24(2):421–429, 2009.

[48] J. SETO, H. S. GUPTA, P. ZASLANSKY, H. D. WAGNER AND P. FRATZL. *Tough Lessons From Bone: Extreme Mechanical Anisotropy at the Mesoscale*. *Adv. Funct. Mater.*, 18:1905–1911, 2008.

[49] P.S. USKOKOVIC, C.Y. TANG, C.P. TSUI, N. IGNJATOVIC AND D.P. USKOKOVIC. *Micromechanical properties of a hydroxyapatite/poly-l-lactide biocomposite using nanoindentation and modulus mapping*. *Journal of the European Ceramic Society*, 27:1559–1564, 2007.

[50] W.C. OLIVER AND G.M. PHARR. *An improved technique for determining hardness and elastic modulus using load and displacement sensing indentation experiments*. *J. Mater. Res.,*, 7(6):1564–1583, 1992.

[51] S. A. SYED ASIF, K. J. WAHL, R. J. COLTON AND O. L. WARREN. *Quantitative imaging of nanoscale mechanical properties using hybrid nanoindentation and force modulation*. *Journal of Applied Physics*, 90(3):1192–1200, 2001.

[52] L.P. MULLINS, M.S. BRUZZI AND P.E. MCHUGH. *Measurement of the microstructural fracture toughness ofcortical bone using indentation fracture*. *Journal of Biomechanics*, 40:3285–3288, 2007.

[53] J.J. KRUZIC, D.K. KIM, K.J. KOESTER AND R.O. RITCHIE. *Indentation techniques for evaluating the fracture toughnessof biomaterials and hard tissues*. *Journal of the mechanical behaviour of biomedical material*, 2:384 – 395, 2009.

[54] I. ZLOTNIKOV, E. ZOLOTOYABKO , P. FRATZL. *Nano-scale modulus mapping of biological composite materials: Theory and practice*. *Progress in Materials Science*, 87:292–320, 2017.

[55] I. ZLOTNIKOV, P. FRATZL AND E. ZOLOTOYABKO. *Nanoscale elastic modulus mapping revisited: The concept of effective mass*. *Journal of applied physics*, 16, 2014.

[56] G. BALOOCH, G.W. MARSHALL, S.J. MARSHALL, O.L. WARREN, S.A.S. ASIF AND M. BALOOCH. *Evaluation of a new modulus mapping technique to investigate microstructural features of human teeth*. *Journal of Biomechanics*, 37:1223–1232, 2004.

[57] S. A. SYED ASIF, K. J. WAHL AND R. J. COLTON. *Nanoindentation and contact stiffness measurement using force modulation with a capacitive load-displacement transducer*. *Review of Scientific Instruments*, 70:2408–2413, 1999.

[58] DR PH. COMPÈRE. *Microscopies électroniques*, chapter : Le microscope électronique à balayage. University of Liege, 2021.

[59] K. AKHTAR, S. A. KHAN, S. B. KHAN, AND A. M. ASIRI. *Handbook of Materials Characterization*, chapter 4 – Scanning Electron Microscopy: Principle and Applications in Nanomaterials Characterization. Joseph G. Carter editor, 2018.

[60] J. I. GOLDSTEIN ET AL. . *Scanning Electron Microscopy and X-Ray Microanalysis*. 2003.

[61] PROF KIN MAN. *Instrumental Methods of Analysis and Laboratory*, chapter 3 – Microscopy (II): scanning electron microscopy scanning probe microscopy. University of Hong Kong, 2021.

[62] FORD, BRIAN J. , JOY, DAVID C. AND BRADBURY, SAVILE. *Scanning electron microscope*. *Encyclopedia Britannica,*, 2019.

[63] M. HARTMANN. *Samples protocol*. Exchange by mail, 2021-02-27.

[64] ATLAS OF PLANT AND ANIMAL HISTOLOGY. *Histological techniques - 3. RESIN EMBEDDING*. https://mmegias.webs.uvigo.es/02-english/6-tecnicas/3-resina.php, (Last access on 2021-04-16).

[65] HERZAN. *Active vibration control*. https://www.herzan.com/resources/technology/active-vibration-control.html, (Last access on 2021-04-25).

[66] HYSITRON. *TI 980 TriboIndenter User Manual*. Revision 10.0.1216.

[67] CERAMTEC. *Basics of Piezo-ceramic Technology*. https://www.ceramtec.com/ceramic-materials/piezo-ceramics/basics/, (Last access on 2021-04-25).

[68] M. DIETIKER. *Nanoindentation of Gold Nanostructures and Nacre-Like Nanocomposites – Size Effects and Limits of Strength*. PhD thesis, ETH Zurich, 2011.

[69] BRUKER. *Quasi-Static Nanoindentation*. https://www.bruker.com/en/products-and-solutions/test-and-measurement/nanomechanical-test-systems/nanoindentation.html, (Last access on 2021-04-26).

[70] J-Y RHO AND G. M. PHARR. *Effects of drying on the mechanical properties of bovine femur measured by nanoindentation. Journal of material science : materials in medicine*, 10:485–488, 1999.

[71] QSIL. *About fused quartz.* https://www.qsil.com/en/material/about-fused-quartz/, (Last access on 2021-03-29).

[72] DESTINY TOOL. *Understanding Surface Finish.* https://www.destinytool.com/surface-finish.html?fbclid=IwAR0eNSmCnll4JrJOkBtaTESt8JFhqQZV0fl6HduURfVsbTMf_Js0rkzOEZo, (Last access on 2021-05-06).

[73] A. TITS. *Where tendons meet bones – Structural and mechanical analysis of Achilles tendon insertion into calcaneus.* PhD thesis, University of Liege, 2018.

[74] SERVICE PUBLIC FÉDÉRAL. *Electricité.* https://www.health.belgium.be/fr/electricite#:~:text=Le%20courant%20du%20r%C3%A9seau%20%C3%A9lectrique,%2C%2050%20Hz)%20en%20Europe., (Last access on 2021-04-28).

[75] MATHWORKS. *Help center - Filloutliers.* https://nl.mathworks.com/help/matlab/ref/filloutliers.html, (Last access on 2021-05-24).

[76] MATHWORKS. *Help center - Filter.* https://nl.mathworks.com/help/matlab/ref/filter.html, (Last access on 2021-05-26).

[77] MATHWORKS. *Help center - Crosscorr.* https://nl.mathworks.com/help/econ/crosscorr.html, (Last access on 2021-05-27).

[78] HENGSBERGER, S., KULIK, A., ZYSSET, P. *Nanoindentation Discriminates the Elastic Properties of Individual Human Bone Lamellae Under Dry and Physiological Conditions. Bone*, 30(1):178–184, 2002.

[79] J. XU, J. Y. RHO, S. R. MISHRA, Z. FAN. *Atomic force microscopy and nanoindentation characterization of human lamellar bone prepared by microtome sectioning and mechanical polishing technique. J Biomed Mater*, 67:719–726, 2003.

[80] Y. ZHOU, M. J. KASTNER, T. B. TIGHE AND J. DU. *Elastic modulus mapping for bovine cortical bone from submillimeterto submicron-scales using PeakForce Tapping atomic force microscopy. Extreme mechanics letters*, 41, 2020.

[81] K. E. STOCKHAUSEN, M. QWAMIZADEH, E. M. WOLFEL, H. HEMMATIAN, I. A. K. FIEDLER, S. FLENNER, E. LONGO, M. AMLING, I. GREVING, R. O. RITCHIE, F. N. SCHMIDT AND B. BUSSE. *Collagen Fiber Orientation Is Coupled with Specific Nano-Compositional Patterns in Dark and Bright Osteons Modulating Their Biomechanical Properties. Acsnano*, 15:455–467, 2021.

[82] D. CARNELLI, P. VENA, M. DAO, C. ORTIZ AND R. CONTRO. *Orientation and size-dependent mechanical modulation within individual secondary osteons in cortical bone tissue. Journal of royal society interface*, 10(81), 2013.

[83] Y. LIU, G. YAN, S. CHEN AND B. CHEN. *Effects of shape and direction of osteocyte lacunae on stress distribution of osteon. Materials Science and Engineering*, 423, 2018.

[84] GUPTA, H. S., STACHEWICZ, U., WAGERMAIER, W., ROSCHGER, P., WAGNER, H. D., FRATZL, P. . *Mechanical modulation at the lamellar level in osteonal bone. Journal of materials research*, 21(08):1913–1921, 2006.

[85] L. FENG, M. CHITTENDEN, J. SCHIRER, M. DICKINSON AND I. JASIUK . *Mechanical properties of porcine femoral cortical bone measured by nanoindentation. Journal of Biomechanics*, 45:1775–1782, 2012.

[86] S. QIUA, D. S. RAOA, D. P. FYHRIEB, S. PALNITKARAAND A. M. PARFITT. *The morphological association between microcracks and osteocyte lacunae in human cortical bone. Bone*, 37(1):10–15, 2005.

[87] A. GUSTAFSSON, M. WALLIN, H. KHAYYERI AND H. ISAKSSON. *Crack propagation in cortical bone is affected by the characteristics of the cement line: a parameter study using an XFEM interface damage model. Biomechanics and Modeling in Mechanobiology*, 2019.

[88] R. SHAHARA AND S. WEINERB. *Open questions on the 3D structures of collagen containing vertebrate mineralized tissues: A perspective. Journal of Structural Biology*, 201:187–198, 2018.

[89] D. B. BURR, M. B. SCHAFFLER AND R. G. FREDERICKSON. *Composition of the cement line and its possible mechanical role as a local interface in human compact bone. Journal Biomechanics*, 21(11):939–945, 1988.

[90] M. B. SCHAFFLER, D. B. BURR, AND R. G. FREDERICKSON. *Morphology of the Osteonal Cement Line in Human Bone. The anatomical record*, 217:223–228, 1987.

[91] M. LANGER, A. PACUREANU, H. SUHONEN, Q. GRIMAL, P. CLOETENS AND FR. PEYRIN. *X-Ray Phase Nanotomography Resolves the 3D Human Bone Ultrastructure. Plos One*, 7(8), 2012.

[92] P. MILOVANOVIC, A. VOM SCHEIDT, K. MLETZKO, G. SARAU, K. PÜSCHEL, M. DJURIC, M. AMLING, S. CHRISTIANSEND AND B. BUSSE. *Bone tissue aging affects mineralization of cement lines. Bone*, 110:187–193, 2018.